ISSN 0915-6348

NATIONAL INSTITUTE FOR FUSION SCIENCE

Plasma-Based and Novel Accelerators
(Proceedings of Workshop on Plasma-Based and Novel Accelerators)
Nagoya, Japan, Dec. 1991

(Received – Apr. 30, 1992)

NIFS-PROC-11 May 1992

RESEARCH REPORT
NIFS-PROC Series

NAGOYA, JAPAN

PLASMA-BASED AND NOVEL ACCELERATORS

(Proceedings of Workshop on Plasma-Based and Novel Accelerators)

NAGOYA, JAPAN, DECEMBER 1991

EDITORS:

RYO SUGIHARA
NAGOYA UNIVERSITY

YASUSHI NISHIDA
UTSUNOMIYA UNIVERSITY

KEYWORDS: ACCELERATOR, PLASMA-BASED ACCELERATOR, BEAT WAVE ACCELERATOR, WAKEFIELD ACCELERATOR, $V_p \times B$ ACCELERATOR, MULTI-LASER-BEAM ACCELERATOR, GAUSSIAN LASER BEAM, PLASMA LENS, FEL, CLUSTER GENERATION

CONTENTS

PREFACE

This publication is a collection of papers presented at Workshop on Plasma-Based and Novel Accelerators held at National Institute for Fusion Science, Nagoya, on December 19-20, 1991. Plasma-based accelerators are attracting considerable attention in these days as a new, exciting field of plasma applications. The study gives rise to and spurs study of other unique accelerators like laser-based accelerators. The talks in the Workshop encompassed beat-wave accelerator (BWA), plasma wake field accelerator (PWFA), $V_p \times B$ accelerator, laser-based accelerators and some novel methods of acceleration. They also covered the topics such as FEL, cluster acceleration and plasma lens. Small scale experiments as those in universities have exhibited brilliant results while larger scale experiments like BWA in Institute of Laser Engineering, Osaka University, and PWFA in KEK start showing significant results as well. We are going to enhance active collaboration between theories and experiments and, in particular, intense communication between big laboratories and small scale university researches.

The editors acknowldge all attendees for their enthusiastic participation and lively discussions. The list of participants and the program of Workshop are given in the last part of this booklet as appendices.

Ryo Sugihara
Yasushi Nishida
April 1992

Laser Ionization of High Speed Gasjet for Beatwave Acceleration

Y. Kitagawa, K. Sawai, K. Matsuo, K. Morioka, and S. Nakai
Institute of Laser Engineering, Osaka University
Yamada-oka 2-6, Suita, 565, Japan

Abstract

A 1ns CO_2 laser ionized a hydrogen gasjet to provide a plasma with the electron density of $10^{17}cm^{-3}$ for the beatwave acceleration experiments. The density is proportional to the square of the injected gas flow. Also it increases as increasing the laser intensity so as the collisionless Keldysh tunnel ionization model suggests. The result of the temporal evolution of the density is consistent with the prediction that the plasma is almost fully ionized at the laser peak.

§1. Introduction

The most importance for the laser beatwave acceleration[1] experiment is to control exactly the electron density of the plasma, in which a beatwave of double line laser excites a relativistic plasma wave. To accelerate particles effectively, a beatwave of 10.6μm and 9.6μm lasers, for instance, needs a plasma of $1.1x10^{17}$ cm^{-3} electron density. The plasma must be more than a few mm in length and larger than a spot size in diameter. Some methods have been reported to provide such resonant density plasmas: one is a high density θ-pinch, which C. Clayton et al. (1987)[2] have used to successfully excite the relativistic plasma wave, but simultaneously generated magnetic fields distorted the orbit of injected electron beams so strongly that detectors, they say, were hard to effectively catch electrons. Z-pinch or multi-arc discharge plasma sources are also used.[3] A double pulse laser illumination on a very thin foil is an another way, as done by N. A. Ebrahim (1985).[4]

A laser ionization has advantages over the above methods, since the laser

does not generate a strong magnetic field in the region far under the cutoff density and since the most attractive is that only one laser can provide both a resonant density plasma and a relativistic plasma wave. Ebrahim et al. have reported the laser ionization for the beatwave acceleration in 1986.[5] We have reported the similar method in the recent publication(1992).[6] A high speed gaspuff injects hydrogen gases of about 1500 Torr·cc into a vacuum chamber, which are ionized by a 1 ns double line laser pulse. Thus we get 10^{17} cm^{-3} electron density plasma as well as a plasma wave of an amplitude $\delta n/n$ ~ 5 %. This plasma wave accelerated plasma electrons to more than 10 MeV. Nevertheless, the important but remained problem in this method is to demonstrate that the laser pulse produces the resonant density plasma so fast that the same laser pulse can excite a relativistic plasma wave within the pulse duration.

We report here that a 1 ns laser provides the resonant density plasma within the laser pulse to excite relativistic plasma wave. The ionized plasma density depends on the laser intensity, so as the collisionless Keldysh ionization model suggests. The plasma grows to have the resonant density before the laser peak timing. The Keldysh tunneling ionization model[7] can explain such a high speed ionization within the laser pulse. A spectral measurement of the temporal evolution of the density is consistent with this prediction. S. L. Chin et al. (1985) have used this model to explain their gas ionization experiment in a CO_2 laser field.[8]

§2. Electron density control by high speed gaspuff

To protect a gun diode for electron beam injection from an unfavorable breakdown and to prevent a laser breakdown far out of the laser focal point, we fed gases to the focal point by a high speed gaspuff.[9] Figure 1 is a schematic cross section of the high speed gaspuff, which consists of mainly a back gas room, a plenum gas room and a magnetic solenoid, driving an aluminum alloy valve plate. A thin rubber divides the back and plenum gas rooms. The plenum gas volume is 20 cc. To open and close the valve as fast

as possible, the back gas pressure P_b must be not lower than the plenum gas pressure P_p. The plenum gas exhaust is open through the valve into a pipe of 2 cm inner diameter. The circumference of the pipe is a solenoidal coil, which guides an injected electron beam onto the focal point.

A 10 kV-100 μF capacitor bank drives the gaspuff solenoid through an ignitron switch. The valve opens with about 20 μs rise time against the back gas pressure. We measured the gas flow Q in Torr·cc from the difference between the indicator values of a vacuum sensor before and after the firing. The vacuum sensor is the Type 600 Absolute Vacuum Transducer, Barocel/Plus. Since the gas expands into a vacuum usually with the sound velocity of ~ 1.6×10^5 cm/s, the gas jet of 440 Torr·cc, for instance, will arrive at the focal point 120 μs after firing the ignitron and fill the inside of the pipe over 50 cm long around the focal point in more 150 μs, providing < ~3 Torr neutral gas pressure. The corresponding gas atomic concentration n_0 will be

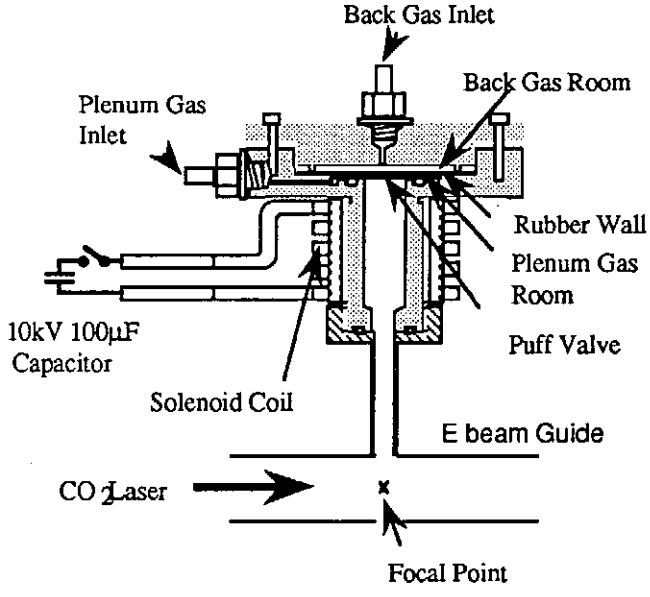

Fig. 1. A schematic cross section of a high speed gaspuff. The laser ionizes gases 270 ms after the ignitron switch is fired.

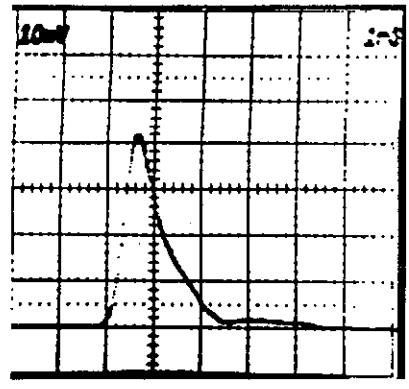

Fig. 2. Pulse shape of the double line CO2 laser measured at the entrance of the vacuum chamber: 1 ns/div. Fast pyroelectric detector *P5-00* is used. Rise time <100 ps.

< 2×10^{17} cm^{-3}. Then the laser ionizes the gas almost fully to produce a plasma of around 10^{17} cm^{-3}. The laser is 300 J in 0.4 ns rise and 1ns width, as shown in Fig. 2. Single line of 10.591 μm or double lines of 10.591 μm and 9.569 μm are used. Since the distance from the output of power amplifier to the vacuum

chamber is ~70 m, the radial mode becomes almost Gaussian, which enables a thin *NaCl* lens to focus the beam to the spot size of much less than 1mm, maybe ~300 μm. Thus the peak intensity is ~4×10^{14} W/cm^2 for 280 J. Since F number is 10, or the lens is so thin, we used the gasjet to prevent the laser breakdown far before the focal point.

From the Stark broadening of the hydrogen Balmer α line (*6563Å*) width, we determined the electron density at the focal point.[10] The emission from that point is collected by a lens into an optical fiber of 800 μm diameter, connected through a monochrometer (0.5 m focal length) to an optical multichannel analyzer. The overall resolution is 1Å. Figure 3 shows a typical spectrum of the Balmer α line emission. Since a Lorentzian curve (a smoothed curve) just fits to this spectrum, we can say that the line broadening is due to the Stark effect, which yields 8.3 Å full width at half maximum, or the electron density n_e of 1×10^{17}cm^{-3},[10] supposed the electron temperature of more than 10 eV. In fact, we estimated the electron temperature from the ratio of total line and continuum intensities, independently of n_e.[11] We can approximate the ratio for hydrogen Balmer α line by an asymptotic curve as

$$\frac{I_l}{I_c} \approx \frac{59 \exp 2.3/T_e}{T_e} \text{ [eV]}, \qquad (1)$$

where I_l and I_c are the Balmer α and continuum intensities integrated over

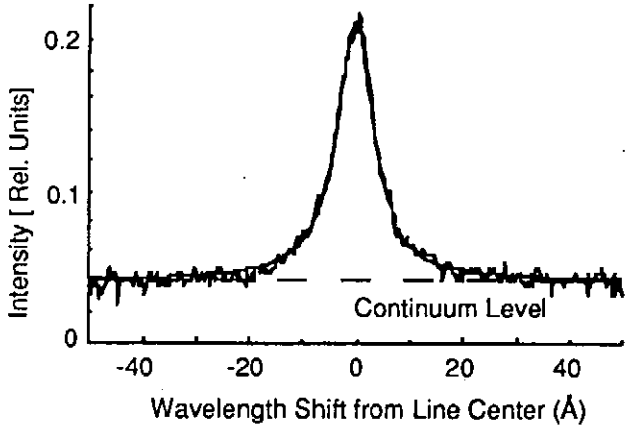

Fig. 3. Typical spectrum of the Balmer a line emission. The line center is 6563 Å. A smoothed line denotes a Lorentzian. The Stark broadening yields 8.3 Å full width at half maximum corresponding to 1x1017 cm-3. The electron temperature of more than 10 eV is assumed.

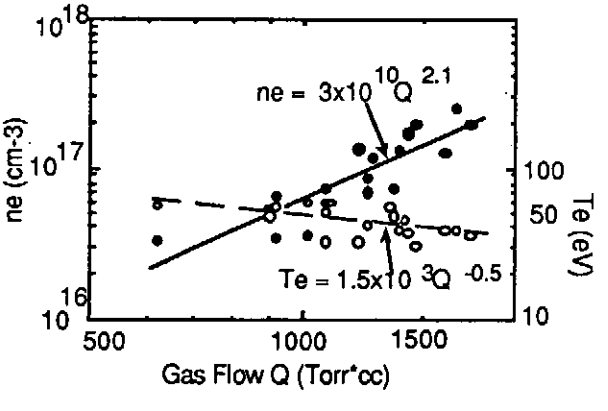

Fig. 4. ne (solid circle) and Te (open circle) at the focal point as a function of the gas flow Q. The lines are best fitted to ne and Te data, respectively. Laser energy is 205±17 J.

100 Å around the line center. From Fig. 3 we obtained I_l/I_c = 1.5, giving T_e = 41 eV. The neutral gas pressure also causes the Lorentzian broadening, but this effect can be neglected under the present low pressure condition.

Thus, in Fig. 4 we plotted n_e and T_e at the focal point as a function of the gas flow Q. Q will be proportional to the neutral gas density n_0. The shot by shot error is within 30 % for the Laser energy deviation of 8 % (205±17J). The lines $n_e \propto Q^{2.1}$ and $T_e \propto Q^{-0.5}$ in the figure are best fitted to n_e and T_e data, respectively. The electron density proportional to $Q^{2.1}$ may lead us to that collisional ionizations dominate, since then the ionization rate n_e/n_0 can be described as $n_0\sigma\sqrt{T_e}$, where σ is an electron impact ionization cross section, usually $\propto \sim 1/T_e$. so that $n_e \propto Q^{2.25}$ using $T_e \propto Q^{-0.5}$. It stands, however, for weak ionization, not for the present case. Furthermore, since a dissociative ionization cross section of H_2 by ~ 50 eV electrons is ~ 3 x10^{-18} cm^{-2} ,[12] a mean free time for dissociative ionization in H_2 is estimated as 7.6 ns for 1.5 Torr, which is too large to ionize the injected gas fully during the 1 ns laser pulse. This is not consistent with the temporal evolution results discussed in §3. The ionization time for single H atom is 0.3 ns.[13] We discuss in the next section the other ionization mechanism to compete with this or to dominate the ionization at least in the very early times. The excitation time for Balmer α is also 7 ns under the same condition,[14] which leads to that the emission peak comes few or few tens ns after the laser pulse. The weak decrease of T_e as $T_e \propto Q^{-0.5}$ will be the result of the increasing energy loss in the higher neutral gas flow.

An optical lens combination, instead of optical fiber, relayed the image of the plasma emission onto the monochrometer. Thus we took the picture of the Balmer α line emission on films, which shows us the emission image is flat 7 mm long along the axis and 1.8 mm wide across the axis. Temporal as well as spatial uniformities of the resonant density plasma, however, are not yet so clear.

§3. Laser ionization of hydrogen gases

To make the ionization mechanism clear, we plotted in Fig. 5 (a) the electron density n_e as a function of the laser intensity I_L. The data seem to be divided into two groups as for Q around 1000 Torr·cc: the low Q data (440 to 1100 Torr·cc: open marks in the figure) and the high Q data (1160 to 1740 Torr·cc: closed marks). As increasing I_L from $1x10^{14}$ W/cm^2 to 2.5 $x10^{14}$ W/cm^2, n_e for high Q, denoted by closed marks, increases slowly and from 2.5 $x10^{14}$ W/cm^2 to $3x10^{14}$ W/cm^2 it goes up fast as shown in Fig. 5 (a). While n_e

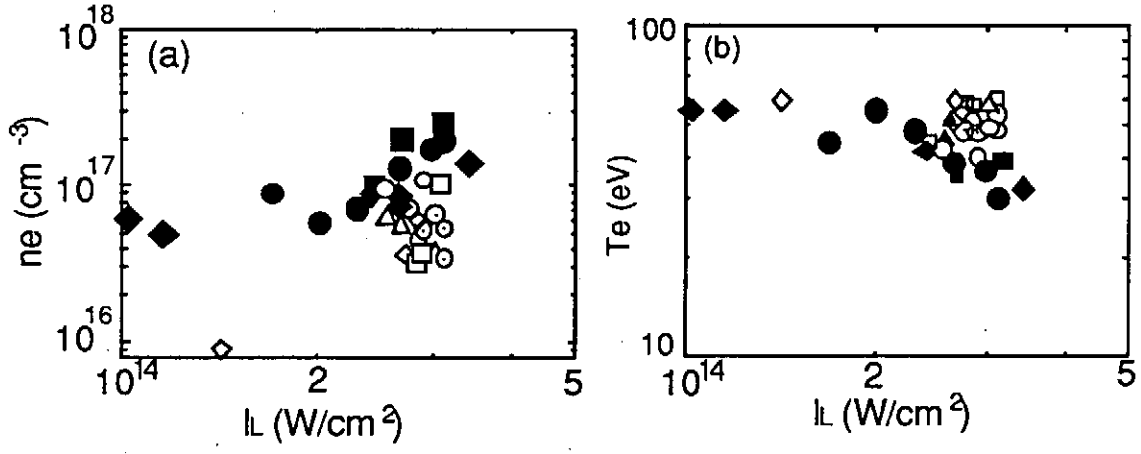

Fig. 5. (a) Electron density ne and (b) electron temperature Te as functions of the laser Intensity IL. The data can be divided to two groups: the low Q (gas flow) data (440 ~ 1100 Torr·cc, denoted by open marks) and the high Q data (1160 ~ 1740 Torr·cc, denoted by closed marks).

for low Q, denoted by open marks, does not increase above $1x10^{17}$ cm^{-3}, but even decreases below $1x10^{17}$ cm^{-3} around $3x10^{14}$ W/cm^2. These results lead us to that the injected gases of low Q(<~1000 Torr·cc) are ionized almost fully at $3x10^{14}$ W/cm^2, giving n_e of $1x10^{17}$ cm^{-3}, but not for Q >1000 Torr·cc. In Fig. 5 (b), T_e for low Q increases at around 2.5 $x10^{14}$ W/cm^2, which seems to show that the most fraction of the absorbed laser energy is used to heat the produced plasma. While, T_e for high Q decreases slowly as increasing I_L, which seems to show that most fraction of the absorbed laser energy is used to ionize the neutral gas. We can say that at least the lowest Q (440 Torr·cc) data provides 100 % ionization, that is, 440 Torr·cc corresponds to $n_0 = 1x10^{17}$ cm^{-3}.

So that to estimate the ionization rate P, defined by n_e/n_0, we divided each n_e by n_0 in Fig. 5 (a), assuming from the above discussion that $n_0 = 1\times10^{17}$ (Q/440 Torr·cc) cm^{-3}. Note that we estimated $n_0 < 2\times10^{17}$ cm^{-3} for 440 Torr·cc in the previous section. We plotted P as a function of the laser intensity I_L in Fig. 6.

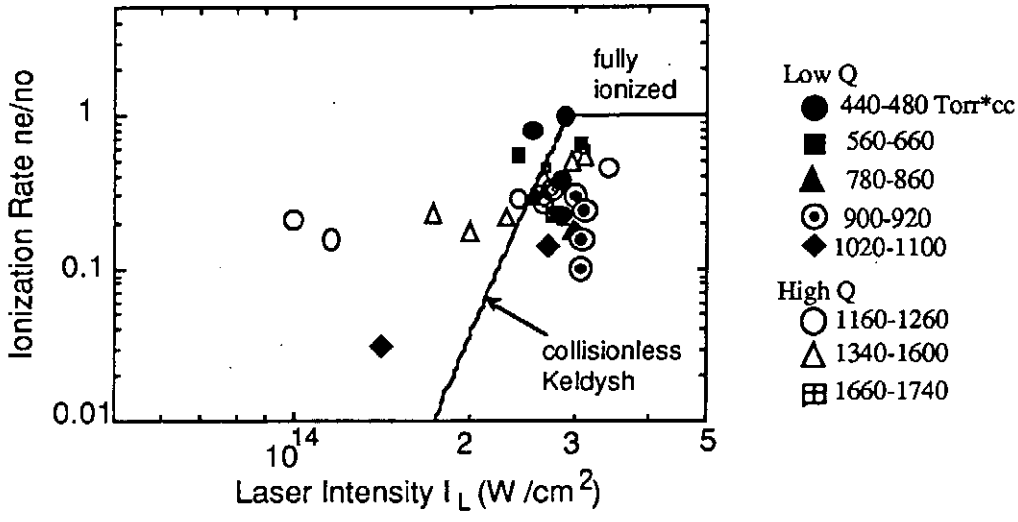

Fig. 6 Calculated and Experimetal Ionization Rate vs Laser Intensity

Intense laser field can distort the atomic potential so as to draw bound electrons out directly. We call this the Keldysh tunneling ionization.[7] The velocity v of the bound electron is given by $(2I_0/m)^{1/2}$. The laser field E affects this electron as $mv/\tau = eE$, if the field does not change during the electron drift through the potential barrier d. Here I_0 is the hydrogen ionization potential of 13.6 eV and ω is the CO_2 laser frequency of 1.78×10^{14} /s. So that the tunneling condition can be written as:

$$\tau \approx \frac{\sqrt{2mI_0}}{eE} < \frac{1}{\omega}. \qquad (2)$$

We are under this condition, because $\omega(2mI_0)^{1/2}/eE \sim 0.08$ for $I_L = 2\times10^{14}$ W/cm^2. This condition is called the strong field condition. The collisionless Keldysh ionization probability is expressed under strong field conditions as[7]:

$$W(t) = \frac{\sqrt{6\pi}}{4}\frac{I_0}{\hbar}\left(\frac{eE\hbar}{m^{1/2}I_0^{3/2}}\right)^{1/2}\exp\left\{-\frac{4}{3}\frac{\sqrt{2m}I_0^{3/2}}{eE\hbar}\left(1-\frac{m\omega^2 I_0}{5e^2E^2}\right)\right\}. \quad (3)$$

Equation (3) yields the ionization rate P at the laser peak (~500 ps after the onset) as follows:

$$P(500ps) = W(t)\times 500ps = 4\times 10^6\left(\frac{I_L}{2\times 10^{14}}\right)^{1/4}\exp\left\{-18.5\left(\frac{2\times 10^{14}}{I_L}\right)^{1/2}\left[1-1.3\times 10^{-3}\left(\frac{2\times 10^{14}}{I_L}\right)\right]\right\}. \quad (4)$$

Equation (4) is plotted in Fig. 6 by a line as indicated, showing that we get P =1 at $I_L \sim 3\ x10^{14}\ W/cm^2$, i.e., the gas is fully ionized at or before the laser peak timing. Almost all the data are close to the line and specially so are for the low Q data, which suggests that the collisionless Keldysh ionization is a dominant mechanism. Some high Q data for $I_L < 2x10^{14}\ W/cm^2$ are far from the Keldysh line, which will be due to collisional effects at the laser timing or due to collisional ionization by heated electrons after the later pulse.

§4. Temporal evolution of the laser ionized plasma

To successfully accelerate electrons, the two frequency laser must meet an uniform and stable plasma with resonant density. So that to check whether this condition is met or not, we time-resolved the Balmer α line spectrum using the monochrometer with a photomultiplier tube with 3 ns resolution. The monochrometer scanned the emission from the center (6563Å) to one wing (6593Å), which are plotted in Fig. 7. The width of the spectral window (resolution) is 7 Å. Each line comes from different shot, but the laser energy and the gas flow are constant all over the shots. The first peak near to 0 ns, denoted by a dashed curve, will correspond to the photo-ionization (excitation), while the second peak at 100 ns, denoted by the second dashed curve, and the later will correspond to the collisional recombination emissions, that is to say, in "afterglow plasmas". The emission at line center increases until around 300ns after the laser onset, as denoted by the third dashed curve. While, the wing emissions decrease faster as shown in the figure. From the data near to 0 ns we constructed the temporal evolution of the electron density within a few ns from the laser onset, as seen in Fig. 8.

The constant density duration seems to be 6 ns or more. Even considering the detector resolution of ~ 3 ns, it will be not far from $(6ns^2-3ns^2)^{1/2} \sim 5$ ns, which is long enough for the 1-ns double line laser to meet the resonant density plasma. Two data series in the figure come from two different energy shots. The collisional ionization rate by electron impact is too small to provide such a high dense plasma at least at the early times, but the Keldysh ionization rate is enough to do it.

Since $I_0/h\nu \sim 120$, the multiphoton ionization will not occur.

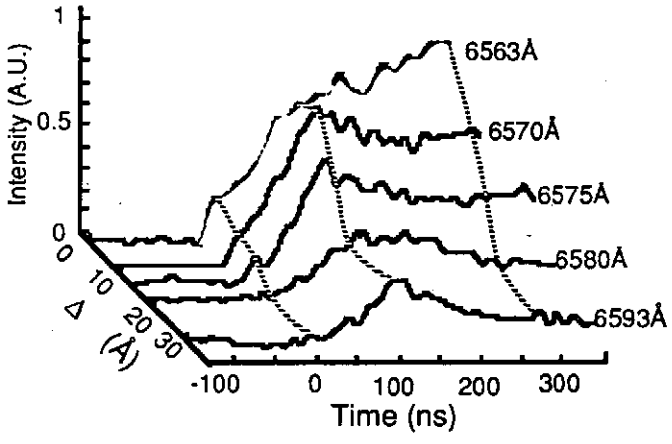

Fig. 7. Temporal evolution of the spectral emissions from 6563 Å(the Blamer a line peak) to 6593 Å(the red side wing). Spectral width is 7 Å and temporal resolution is 3 ns. Laser comes at around 0 ns. Laser:180±11 J; Gas flow Q:1500±110 Torr·cc.

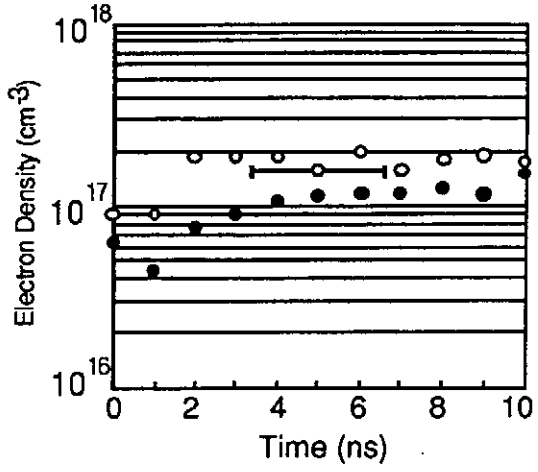

Fig. 8. Temporal evolution of the electron density within a few ns from the laser onset. Open circle: laser energy of 206±5 J and hydrogen flow Q of 1540±360 Torr·cc; solid circle:180±11 J and 1500±110 Torr·cc, respectively. Horizontal bar denotes the time resolution.

§5. Conclusions

The results are:

(1) The plasma density increases in proportion to the square of the gas flow Q within 30 % error, while the electron temperature decreases as the square root of Q.

(2) As increasing the laser intensity from 2.5×10^{14} W/cm^2 to 3×10^{14} W/cm^2, the electron density increases for high Q (>1100 Torr·cc). While, for the low Q (<1100 Torr·cc) it saturates or even decreases because of fully ionization.

(3) The collisionless Keldysh model predicts that the CO_2 laser at 3×10^{14}

W/cm^2 can fully ionize hydrogen gas in 500 ps, that is, before the laser peak comes to the focal point.

(4) The electron density is constant over 5 ns around the laser peak, which is consistent with the Keldysh model calculation.

We conclude that 1-ns CO_2 laser can ionize the gas and provide the resonant density plasma for the beatwave acceleration within the pulse. The Keldysh tunneling ionization seems to dominate the ionization within the pulse. In this plasma the same double line laser excites a relativistic plasma wave to accelerate electrons. We can successfully use single pulse laser for beatwave acceleration study.

Acknowledgements

The high speed gaspuff used here is designed by Prof. S. Goto and his student of the Plasma Physics Laboratory, Osaka University. We thank them very much. The *LAC MATRIX* members: K. Mima, K. Nishihara, H. Takabe, H. Azechi and K. A. Tanaka for their valuable supports and discussions are acknowledged with pleasure. We also acknowledge Prof. emeritus C. Yamanaka for his encouragement.

References

1) T. Tajima and J. M. Dawson, Phys. Rev. Lett., **56**, 267 (1979).

2) C. E. Clayton, C. Joshi, C. Darrow and D. Umstadter, Phys. Rev. Lett., **54**, 2343 (1985).

3) C. E. Clayton, UCLA, Institute of Plasma and Fusion Research Preprint **PPG-1340**, March 1991.

4) N. A. Ebrahim, P. Lavigne and S. Aithal, IEEE Trans. Nuclear Science, **NS-32**, 3539 (1985).

5) F. Martin, P. Brodeur, J. P. Matte, H. Pepin and N. Ebrahim, Preprint for the Proc. SPIE, **Vol. 664**, High Intensity Laser Process (1986).

6) Y. Kitagawa, T. Matsumoto, T. Minamihata, K. Sawai, K. Matsuo, K. Mima, K. Nishihara, H. Azechi, K. A. Tanaka, H. Takabe and S. Nakai, Phys. Rev. Lett., **68**, 48 (1992).

7) L. V. Keldysh, Soviet Physics JETP, **20**, 1307 (1965).

8) S. L. Chin, F. Yergeau and P. Lavigne, J. Phys. B: At. Mol. Phys. **18**, L213 (1985).

9) Y. Kitagawa, Quarterly Progress Report, **ILE-QPR-91-38**,(Institute of Laser Engineering, Osaka University, 1992)

10) G. Bekefi, *"Principle of Laser Plasmas"*, Ch. 13. John Wiley & Sons, N. Y. 1976.

11) H. R. Griem, *"Plasma Spectroscopy"*, McGraw-Hill, New York, 1964.

12) S. C. Brown, *"Basic Data of Plasma Physics, 1966"*, 2nd edition, revised (MIT Press, London, 1966).

13) W. L. Fite and R. T. Brackmann, Phys. Rev., **112**, 1141 (1958).

14) H. Kleinpoppen and E. Kraiss, Phys. Rev. Lett., **20**, 361 (1968).

20MeV ESM Calibration for Laser Beat-Wave Acceleration

K. Sawai, Y. Kitagawa, K. Matsuo, K. Morioka,
and S. Nakai

Institute of Laser Engineering, Osaka University

Yamada-oka 2-6, Suita, 565, Japan

§1. Introduction

We have done beat-wave-acceleration experiment using CO_2 laser[1]. Figure 1 shows the experimental setup. The LEKKO VIII electron-beam controlled CO_2 laser[2] produced a 0.4 ns rise and 1 ns full width at half maximum pulse containing 150 J in the 10.6μm and 9.6μm line, respectively. An f/10 NaCl lens focused the laser beam of a 23 cm diameter to less than a 1-mm-diameter spot. H_2 gas was injected to the laser-focal point by a high-speed puff about 270μs before the laser irradiation. The laser generated a plasma and a plasma wave at the same time. From the Stark broadening measurement of the hydrogen Balmer α line (6563 Å) emission we estimated the electron density and temperature at the focal point[3]. We measured a scattered light at 11.857μm with a liquid He-cooled Cu-Ge detector to confirm the plasma wave excitation and to estimate its amplitude. The plasma wave amplitude was about 6%. Hot electrons(~1 MeV) in the plasma were accelerated to the energy of higher than 10 MeV (see the appendix). Accelerated electrons were measured by a 20-MeV-electron spectrometer (ESM).

Using 18 to 20 MeV linac electrons we calibrated the sensitivity of the ESM, which we report here.

§2. Experiment

Figure 2 shows the schematic of the 8 channel ESM setup. A rare earth-cobalt dipole magnet (CORMAX-2300) of 4.8 kG analyzes electron energy from 3.3 to 22.6 MeV. The channel separation is 2.8MeV and width is 600keV. The detector consists of the Pilot-U scintillator (rise time < 1ns) and the R647-09 photo-multiplier tube (PMT)(HAMAMATU). The outputs from PMT's

are connected to a CAMAC system as well as to oscilloscopes.

Calibration setup of the ESM gain is shown in Fig.3. The electron beam from the linac output double Quadrupole magnet (Q-Mag) was emitted through an aluminum attenuator plate (2mm) into the ESM aperture. Since the linac current is so high that the fluorescent light from the scintillator is too strong to directly illuminate the PMT. Therefore and also to reduce background noises, we inserted an optical fiber (OF) of 200μm diameter and of 20m length between the scintillator and the PMT. The fiber output is connected to the PMT set outside the room. At the same time, we decreased the PMT-applied voltage from 1000V to 400V. To know the absolute value of the current into the channel window, we put plain metal electrode as a charge collector (CC) to 18 or 20MeV channel windows. The linac electron energy is varied from 18MeV to 21MeV, so as to calibrate both 18 and 20.5MeV channels. The linac output has a 20 ns width and a 1.5A peak current, 30 pps.

§3. Experimental Results

Figure 4 shows the energy difference between the design (solid line) and the measured points. The difference are within 5%, which is less than the field difference of 8% between the center (4.8kG) and the edge (4.4kG).

At the beat-wave-acceleration experiment[1], we linked the scintillator directly to the PMT and the PMT-applied voltage was 1000V. So that, we need the following formula to obtain the net sensitivity G, or the PMT output gain per electron into each channel:

$$G = \frac{PMT}{CC} \times \frac{1}{\eta_F} \times \left(\frac{V_1}{V_2}\right)^N , \qquad (1)$$

where PMT is the PMT output current, CC is the absolute current into the channel window, η_F is the optical fiber coupling efficiency. Since the PMT output current is proportional to Nth power of the applied voltage V, we need additional factor $(V_1/V_2)^N$, where V_1=1000V and V_2=400V. Figure 5 shows the oscilloscope traces of both the PMT and the charge collector currents for the linac electron energy of 20MeV. The upper traces are the 7th channels

(17.7MeV) and lower traces are the 8th channels (20.1MeV), respectively. The PMT output peak signal of the 8th channel in the left photograph is 260μA and the corresponding CC signal (right side) is 12μA. Since the ratio of these two peak currents is 21.7, while the ratio of the charges included in each pulse is 31, the net ratio should be within 26±5.

Even though we have reduced the signal intensity by using the optical fiber, as written in the previous section, the 7th channel PMT current yet saturated, as seen in the photograph. So that we used only the 8-channel signals to get the ratio of PMT current and the absolute current, which is 26±5. Both the η_F and N are determined by using a optical pulser (6720 Å)(PLP-01). The light from the optical pulser were emitted into the Pilot-U linked to the PMT with and without optical fiber. As shown in Fig. 6, changing the PMT-applied voltage from 400 to 1000V, we plotted the PMT output with optical fiber(the solid circle), and that without fiber(the open circle). Both the data points have a same slope at the nonsaturated region. We get $\eta_F=(2.1\pm0.4)\times10^{-3}$ from the vertical sift of the data and N=7.8±0.2 from the slope of the line. The data widths come from the read out errors. Thus we get G for the 20 MeV electron, as

$$G = (1.8\pm0.9)\times10^{7}.$$

The sensitivities of the other channels can be obtained from this value proportionally to the electron energy.

Figure 7 shows the beat-wave-acceleration data.[1] We see, high energy electrons (10-20 MeV) from 10 to 100 electrons at double line laser and plasma electron density matching condition.

§4. Conclusion

As for the 20-MeV electron spectrometer(ESM),

[1]The energy difference between the designed and the measured value is within 5% for 18~20MeV range.

[2]The ESM sensitivity G is $(1.8\pm0.9)\times10^{7}$ for 20MeV. This value is used to estimate the beat-wave accelerated electrons[1].

Acknowledgment

This work was done under the cooperation with the Radiation Laboratory, the Institute of Science and Industrial Research, Osaka University. We thank K. Tsumori of the Radiation Laboratory very much.

Appendix

In the wave frame, a wave with a potential energy ϕ' can trap electrons with γ' and $\beta' = (1-1/\gamma'^2)^{1/2}$ when

$$(\gamma' - 1)\, mc^2 < e\phi', \tag{A-1}$$

where " prime " denotes the wave frame quantity. So that the maximum energy W_+, the electrons obtain from the wave, is

$$W_+ = \gamma'_+ mc^2 = e\phi' + mc^2 \quad \text{and} \quad \beta'_+ = \beta', \tag{A-2}$$

and the minimum energy W-, over which the wave can trap the electrons, is

$$W_- = \gamma'_- mc^2 = e\phi' + mc^2, \quad \text{but } \beta'_- = -\beta'. \tag{A-3}$$

W_+ and W_- are Lorentz-transformed to the laboratory frame by[4)]

$$\begin{pmatrix} p_\pm \\ \frac{iw_\pm}{c} \end{pmatrix} = \begin{pmatrix} \gamma_\phi & -i\beta_\phi\gamma_\phi \\ i\beta_\phi\gamma_\phi & \gamma_\phi \end{pmatrix} \begin{pmatrix} \pm mc\gamma'_\pm\beta' \\ imc\gamma'_\pm \end{pmatrix}, \tag{A-4}$$

where $\gamma_\phi = \omega/\omega_\phi$ and $\beta_\phi = (1-1/\gamma_\phi^2)^{1/2}$ are the wave quantities and ω is a laser frequency. Then,

$$W_\pm = mc^2\gamma_\phi\gamma'_\pm(1\pm\beta_\phi\beta'). \tag{A-5}$$

On the other hand, the wave potential is in the laboratory frame notations:

$$e\phi' = e\gamma_\phi\phi = \gamma_\phi mc^2\varepsilon, \tag{A-6}$$

where $\varepsilon = \delta n/n$ is the wave amplitude. Substituting Eq. (A-6) into Eqs. (A-2) and (A-3), we get

$$\gamma'_\pm = \gamma_\phi\varepsilon + 1. \tag{A-7}$$

Thus, we have from Eq. (A-5):

$$W_\pm = mc^2\gamma_\phi(\gamma_\phi\varepsilon+1)(1\pm\beta_\phi\beta'). \tag{A-8}$$

When $\varepsilon \sim 0$, β' becomes ~ 0, then

$$W_\pm \approx mc^2\gamma_\phi. \tag{A-9}$$

When $\varepsilon \sim 1$ and $\gamma_\phi > 1$,

$$W_+ \approx 2mc^2\gamma_\phi^2 \text{ and } W_- \approx 0 \qquad \text{(A-10)}$$

Equation (A-8) is plotted in Fig. 8 for the cases of CO_2 laser ($\gamma_\phi = 10$) and glass laser ($\gamma_\phi = 100$), where W± indicates for convenience, only the kinetic energy part. The figure indicates that a glass-laser pulse can accelerate electrons up to 10 GeV.

References

1) Y. Kitagawa, T. Matsumoto, T. Minamihata, K. Sawai, K. Matsuo, K. Mima, K. Nishihara, H. Azechi, K. A. Tanaka, H. Takabe, and S. Nakai, Phys. Rev.Lett., 68, 48 (1992).
2) C. Yamanaka et al., IEEE J. Quantum Electronics,**QE-17**,1678 (1981)
3) G. Bekefi *" Principle of Laser Plasma"*, Ch. 13. John Wiley & Sons, N.Y.1976
4) L. D. Landau and E. M. Lifshitz, *" The Classical Theory of Fields"*, 4th ed., Ch. 2, Moscow 1962.
5) F. Martin et al. Preprint for the Proc. SPIE, Vol. 664 High Intensity Laser Process (1986).

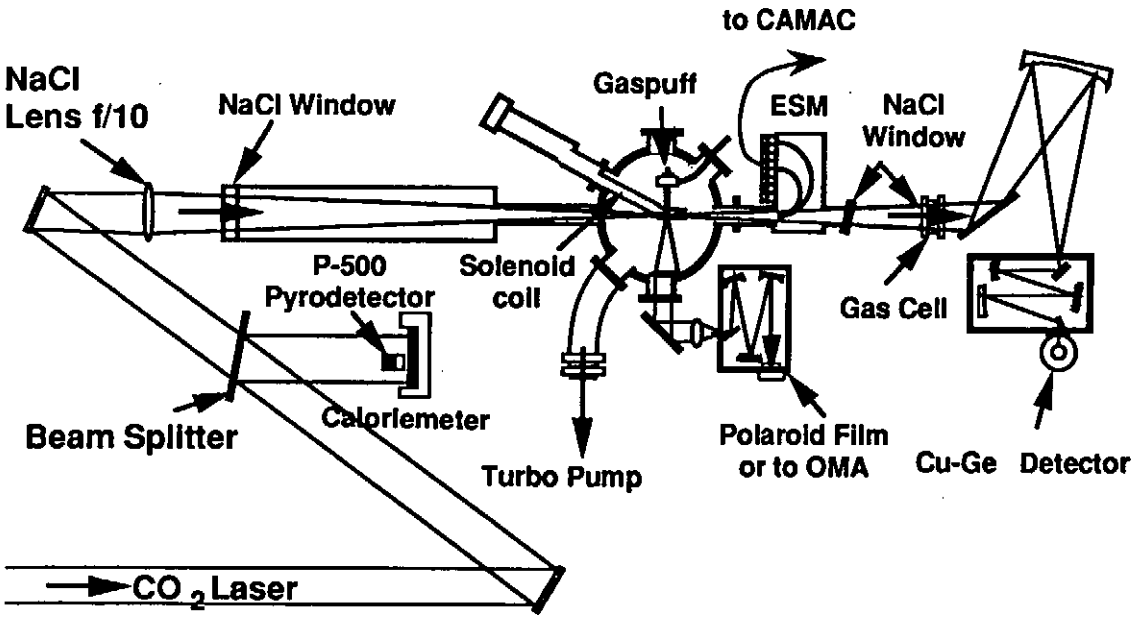

Fig.1 Experimetal setup for Beat Wave Acceleration.

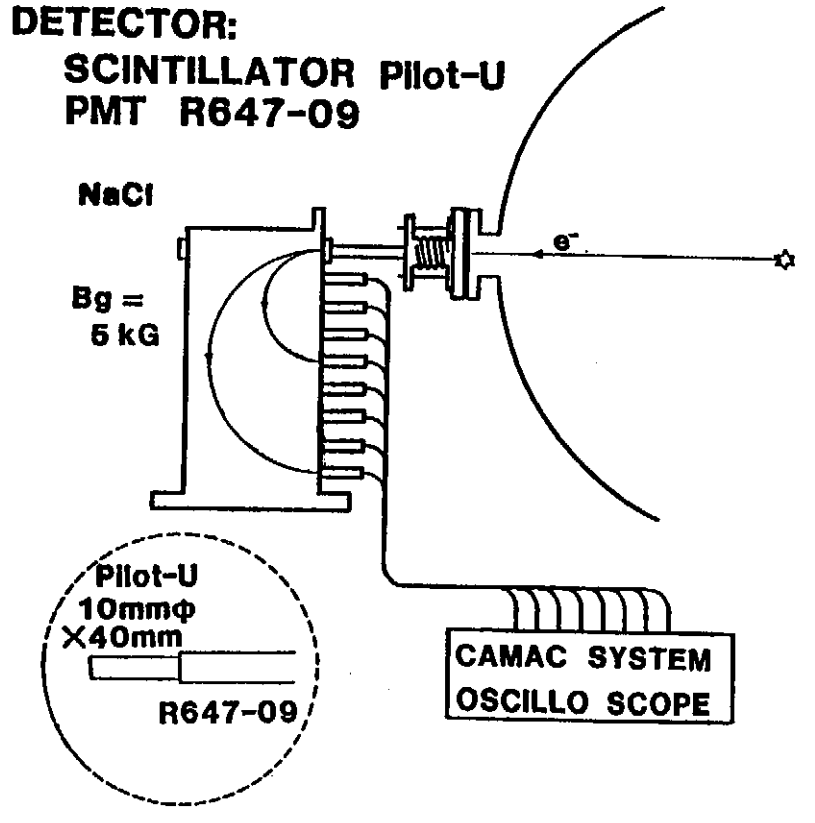

CHANNEL: 8

from 3.1MeV to 22.6MeV step 2.8MeV
CHANNEL WIDTH 0.6MeV

Fig.2 Schematic of 20MeV ESM.

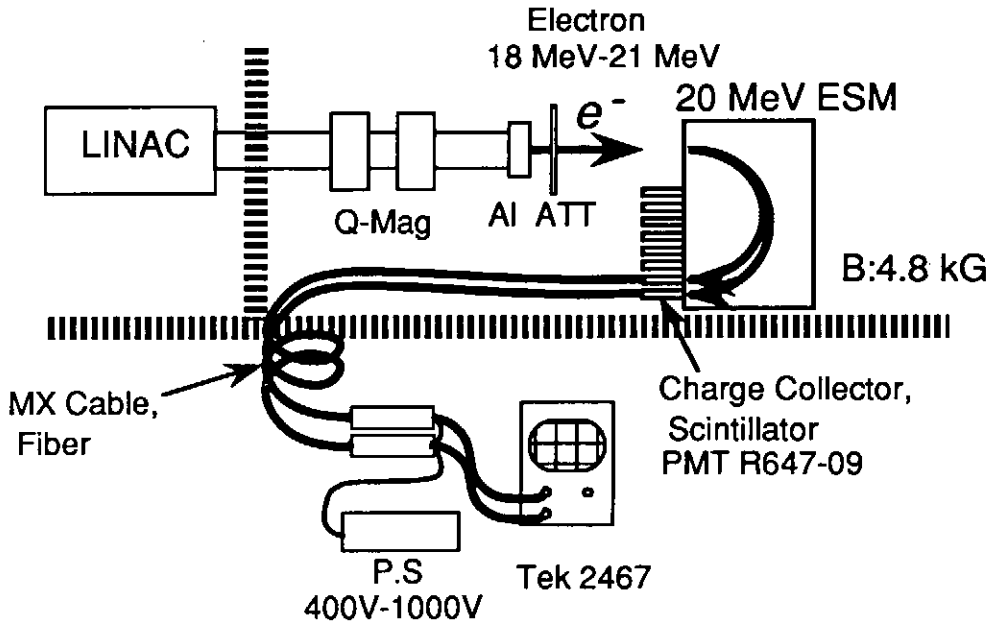

Fig.3 ESM calibration setup by LINAC.

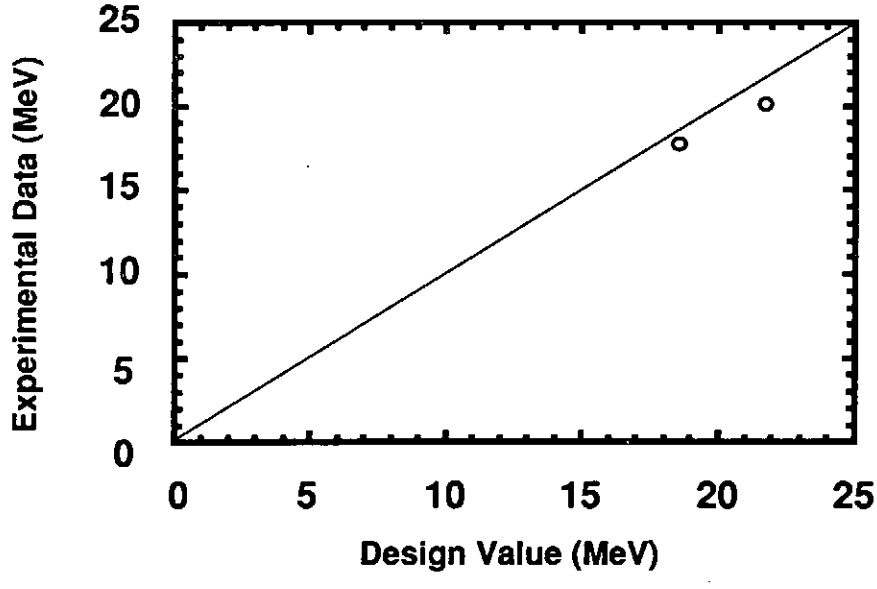

Fig.4 Comparison between the designed (line) and measured electeonenergy (point).The deviation from the designed value is 5%

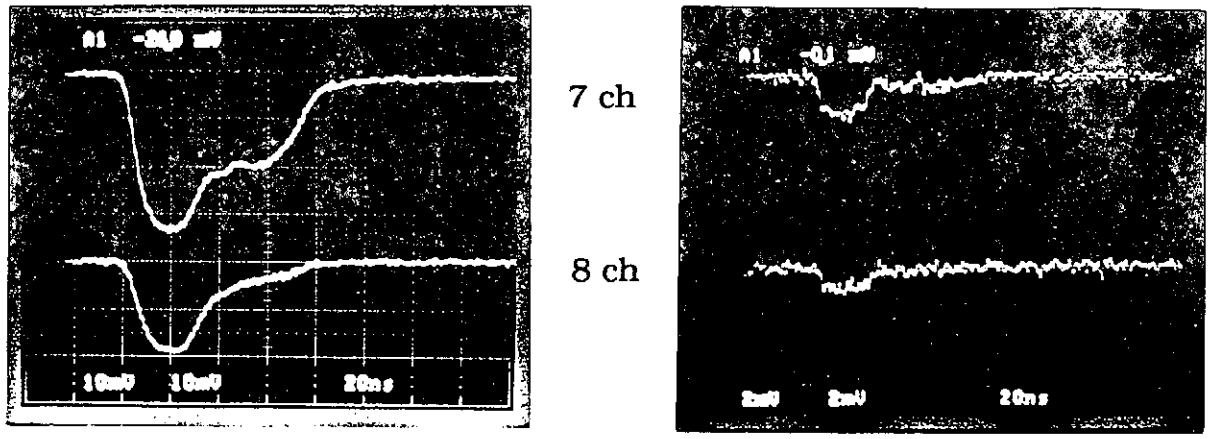

PMT Charge collector

Fig.5 Oscilloscope traces of PMT and charge collector currents for the electron energy of 20MeV.

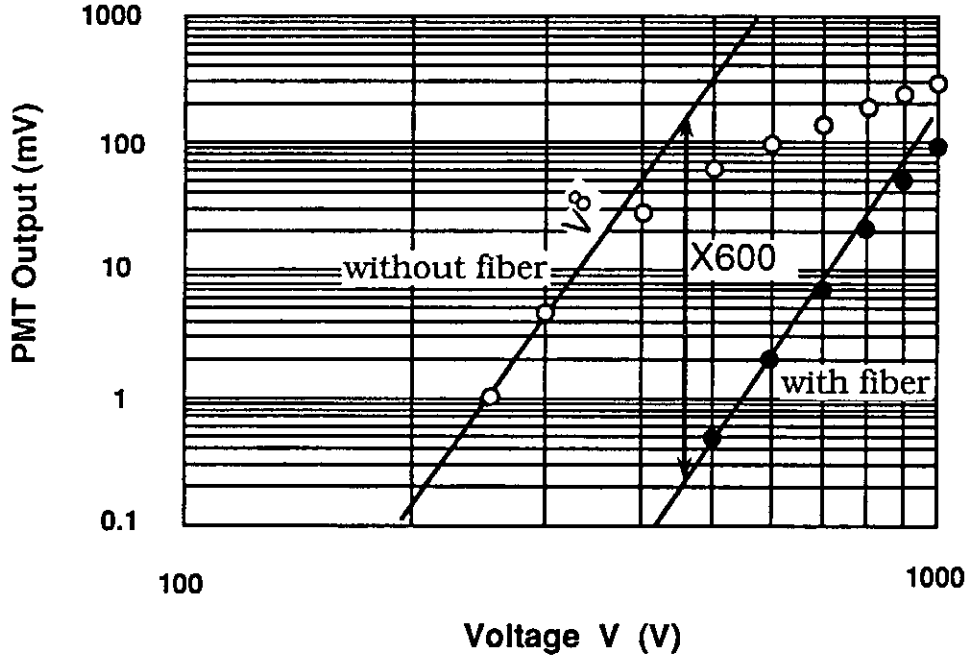

Fig.6 PMT output when the applied voltage are varied from 400 to 1000 V. $\eta_F = 1.67 \times 10^{-3}$ is determined from the vertical sift of the two lins. The line slope N is 8.

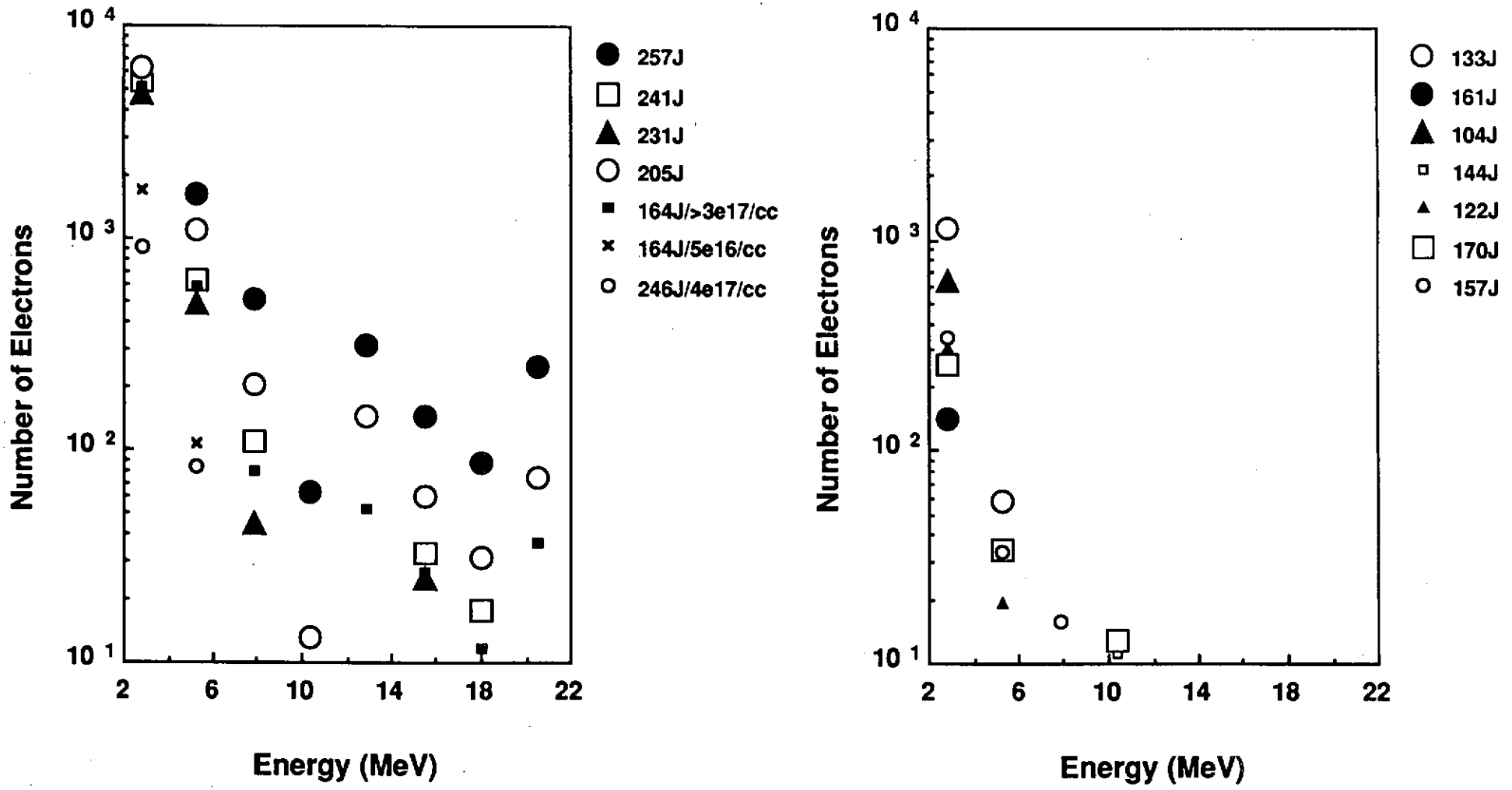

Fig.7 Energy spectra of the electrons from the plasma. Number of electrons
(a) with the double line both at and out of resonance and
(b) with the single line irradiation at the resonance(1-2x10^{17}/cc)

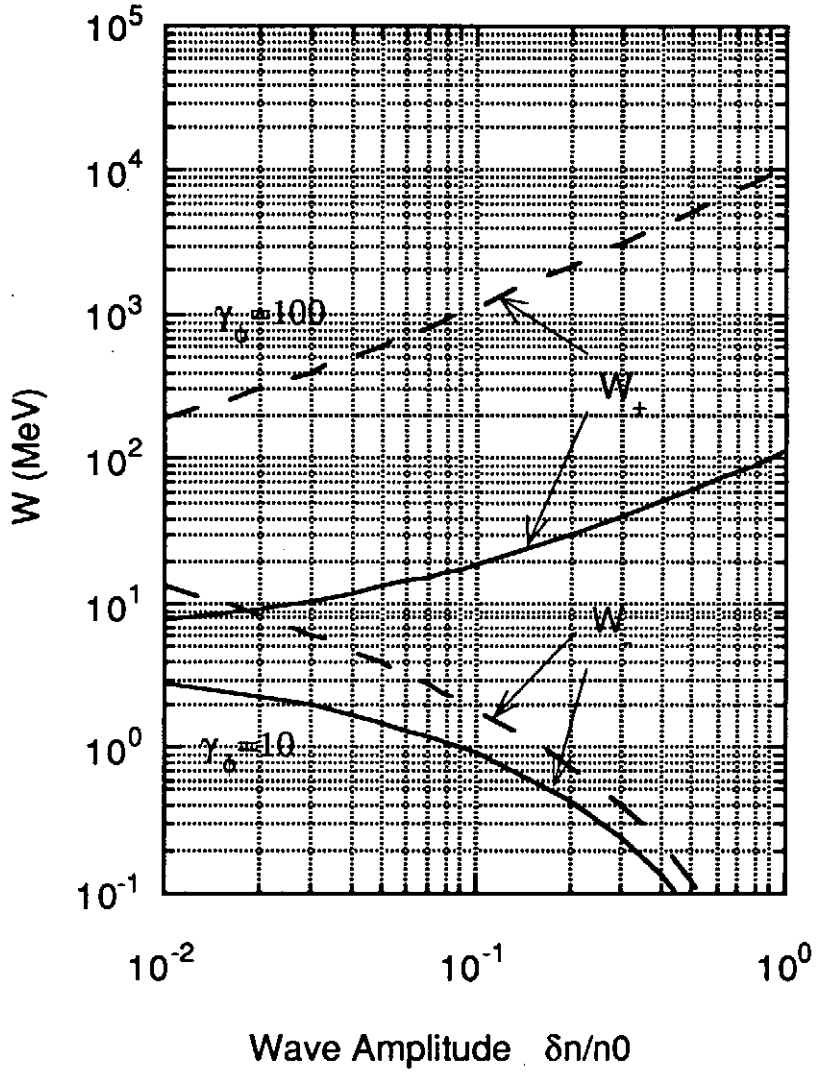

Fig. 8 Minimum(W-) and maxmum (W+) kinetic energy of electrons for γ_ϕ=10 (CO_2 laser) and γ_ϕ=100 (Glass laser).

Stabilization of Double Line Oscillation for Beat-wave Acceleration

K. Matsuo, Y. Kitagawa, K. Sawai, K. Morioka, and S. Nakai

Institute of Laser Engineering, Osaka University
Yamada-oka 2-6, Suita, 565, Japan

§1. Introduction

One of the most importance for the beat-wave acceleration[1] is double line oscillation of a laser, since a beat of the double line drives a plasma wave. For this purpose, we used the LEKKO VIII Electron-Beam controlled CO_2 laser system[2] and obtained stable double line oscillation both by injection-locking, that is, by injecting *CW* CO_2 laser into the oscillator cavity and by feedback controlling the cavity length.

§2. Cavity length fine control by PZT

A piezoelectric translator(PZT) control setup is shown in Fig. 1. To most simply obtain stable double line oscillation, we injected only the 9P line, but not the 10P line, which is spontaneously excited in the cavity. For the gas mixture of CO_2:N_2:He=8:19:73, a *CW* CO_2 laser(NEC CL111B) provides a 16W output of 9P(22) line. About 10% of the 9P(22) output was injected into the TEA oscillator cavity of the LEKKO VIII system. A part of the injected light, leaked out from the cavity, was monitored by a calorimeter C_1. The PZT can drive the cavity mirror M_1, so as that, when 1000V is applied on the PZT, the cavity length moves 12μm. A software "Lab VIEW II" controls a personal computer Macintosh IIfx linked PZT. Typical block diagram inside the left-bottom box in Fig. 1 is shown in Fig. 2. The Lab VIEW is an icon-based graphical programming system for building software modules for data acquisition, data analysis and instrument control. Thus we obtained the tuning curve of cavity, as seen in Fig. 3. The smoothed curve is the best fitted sinusoidal one. The *CW* CO_2 laser heating of the intercavity optical components[3] and also the *CW* laser output ripples might cause the data scatter

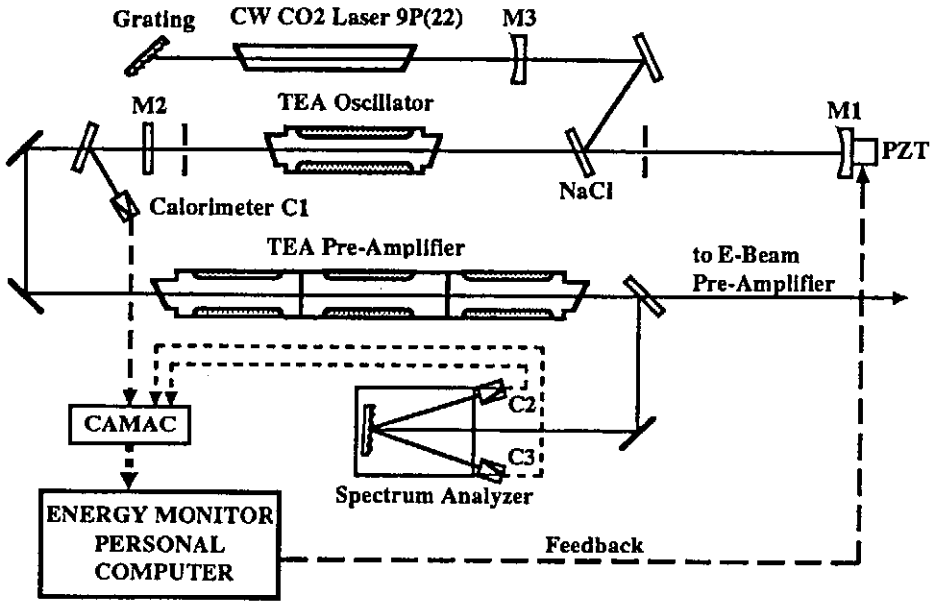

Fig. 1. Setup for double line oscillating the LEKKO VIII CO2 Laser system.The broken line denotes a feedback-control loop(used in §3). (M1:Au Coated Spherical (10m) Mirror, M2:Flat Ge Mirror R=35%, M3:Spherical (5m) ZnSe Mirror R=65%)

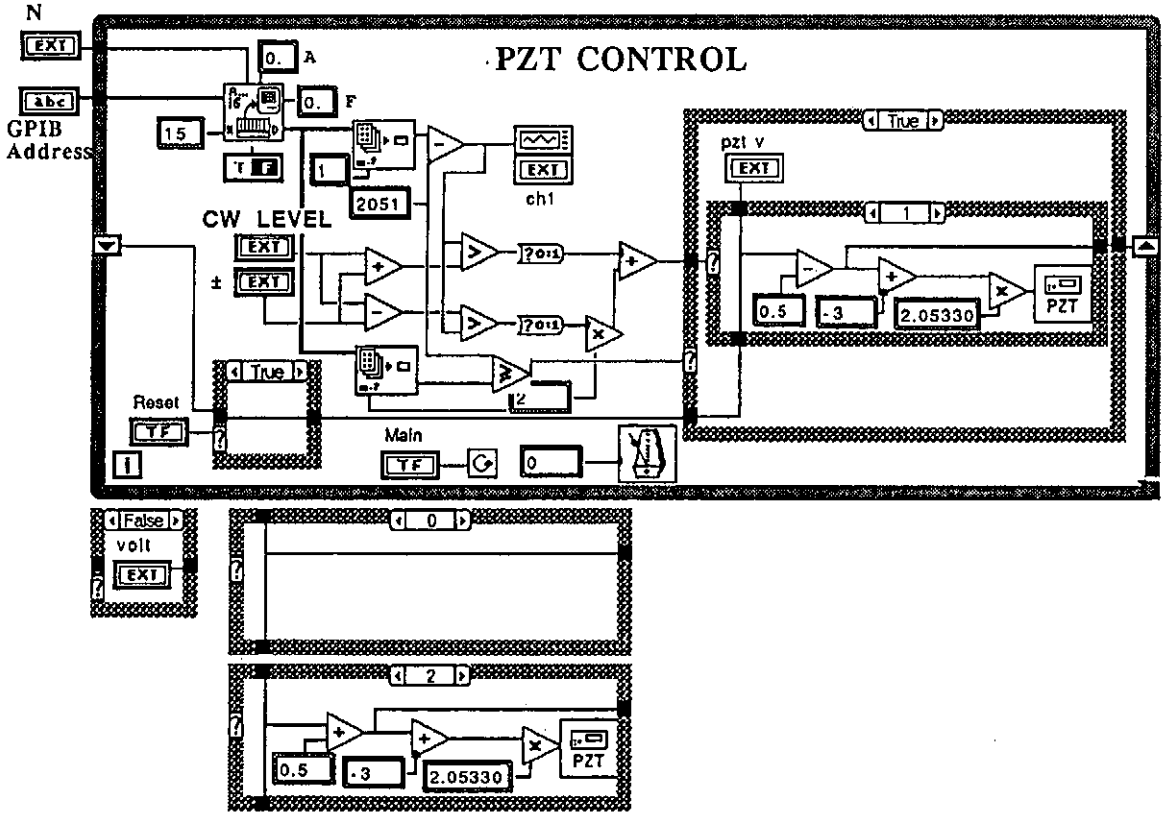

Fig. 2. Block diagram for the PZT control in the Lab VIEW II icon This shows the diagram inside the left-bottom box in Fig. 1.

and shift from the sinusoidal curve, which demands us to keep the cavity in a constant temperature condition.

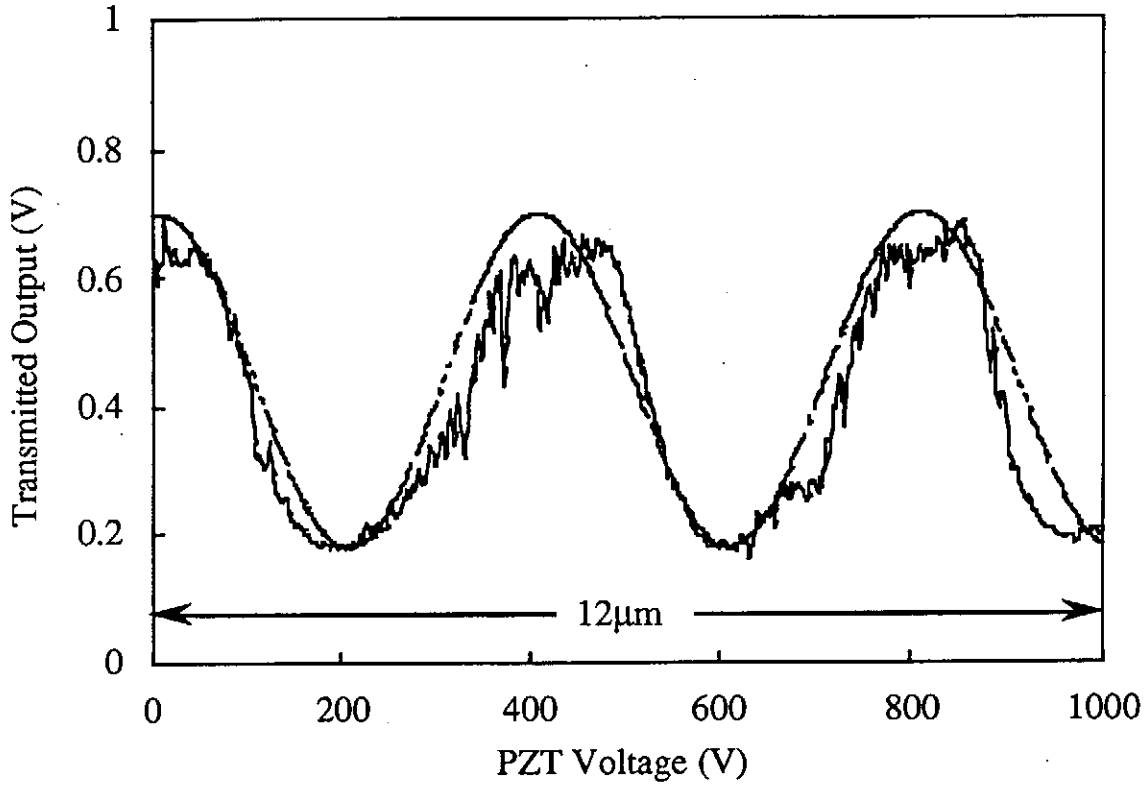

Fig. 3. CW 9P(22) light transmitted thrugh the cavity.
The smoothed curve is the best fitted sinusoidal one.

Then the oscillator is fired and the output is sliced to 1ns by double Pockels cells driven by a LTSG (laser trigger spark gap). After amplified in the TEA pre-amplifier, a 1ns pulse goes to an electron-beam(E-Beam) pre-amplifier. Both the lines are monitored by calorimeters C_2 and C_3 through a spectrum analyzer, separately. The output of each line is plotted vs PZT voltage in Fig. 4. It seems that for the voltage of 450V we can get the equal output, i.e., 0.3mJ for each line, as shown in Fig. 4. Even though fixing the voltage at 450V, however, the output goes out from the constant line in a few minutes (maybe 5 min. or so), as shown in Fig. 5. It might come from a few-minutes change of longitudinal mode of the *CW* CO_2 laser as well as a mechanical change of the cavity length due to such that some decrease of a gas in the oscillator or the temperature increase inside the cavity.

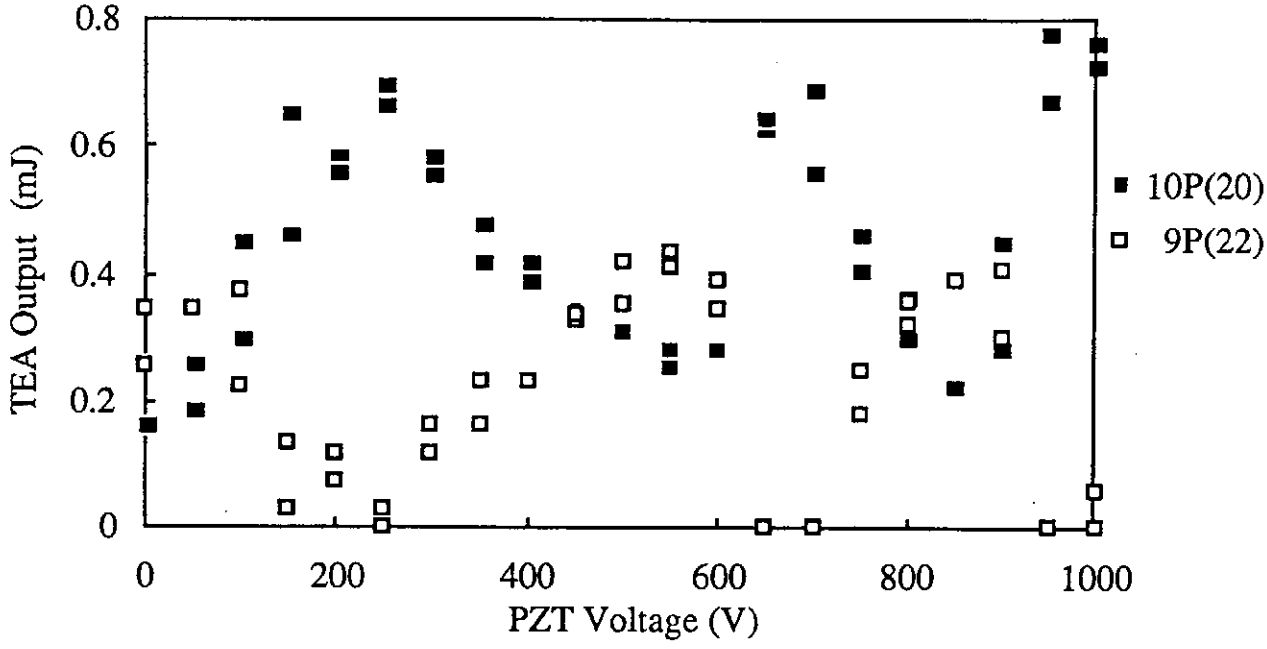

Fig. 4. 10P(20) and 9P(22) signals which was separated by spectrum analyzer, when PZT voltage increased to 1000V in steps of 50V.

§3. Feedback control of cavity

To improve the above-mentioned temporal decrease of the two line outputs, we tried to feedback-control the cavity length. We fedback the output from C_1 through a CAMAC-ADC, linked to a personal computer Macintosh IIfx, to the PZT driver. The software "Lab VIEW II" controlled the whole feedback system. The feedback linkage controlled the cavity length so constant as to tune to the injected 9P(22) line and to provide stable and constant outputs, as shown in Fig. 6, which shows a good improvement comparing with that in Fig. 5. The remained problem is to remove the small ripples of 10~20 seconds, as shown both in Figs. 5 and 6, which comes from the *CW* CO_2 laser.

Fig. 7 shows outputs of the spectrum analyzer with and without feedback control. A straight line indicates the constant total output energy, all over which line scatter the data without feedback(open circle). Once the feedback loop operates, the points, formerly scattered over the line, converge to the central small shadow area.

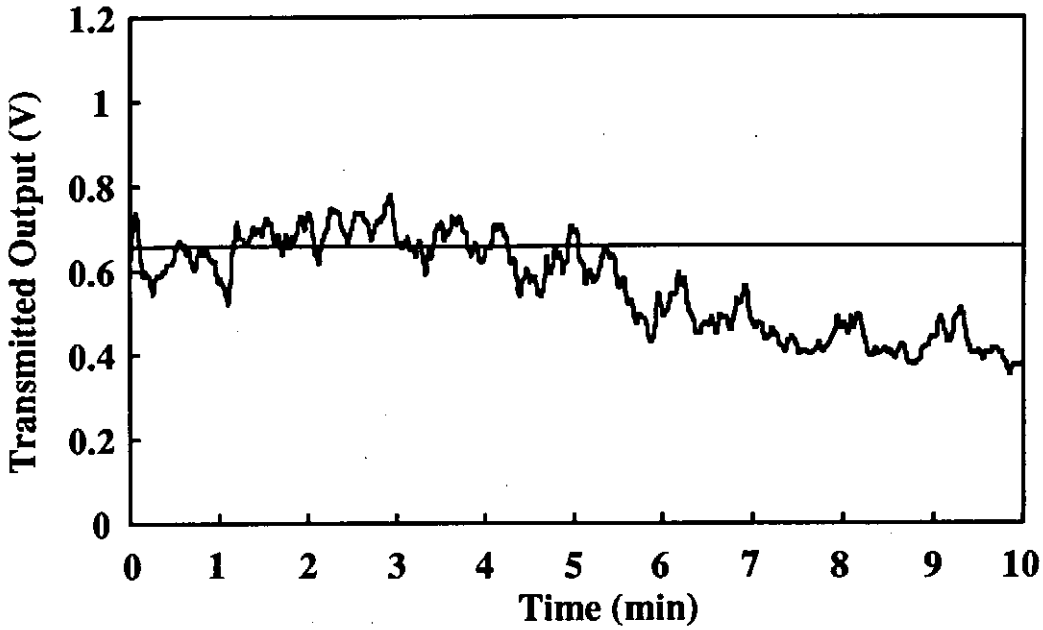

Fig. 5. CW 9P(22) output stability without feedback .

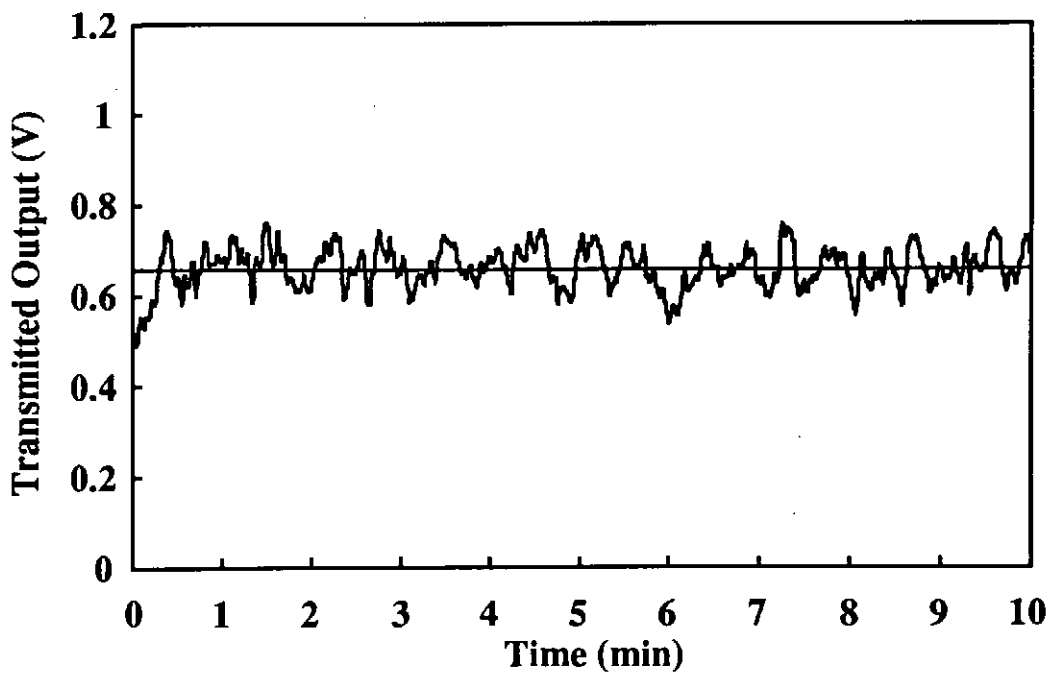

Fig. 6. CW 9P(22) output stability with feedback .

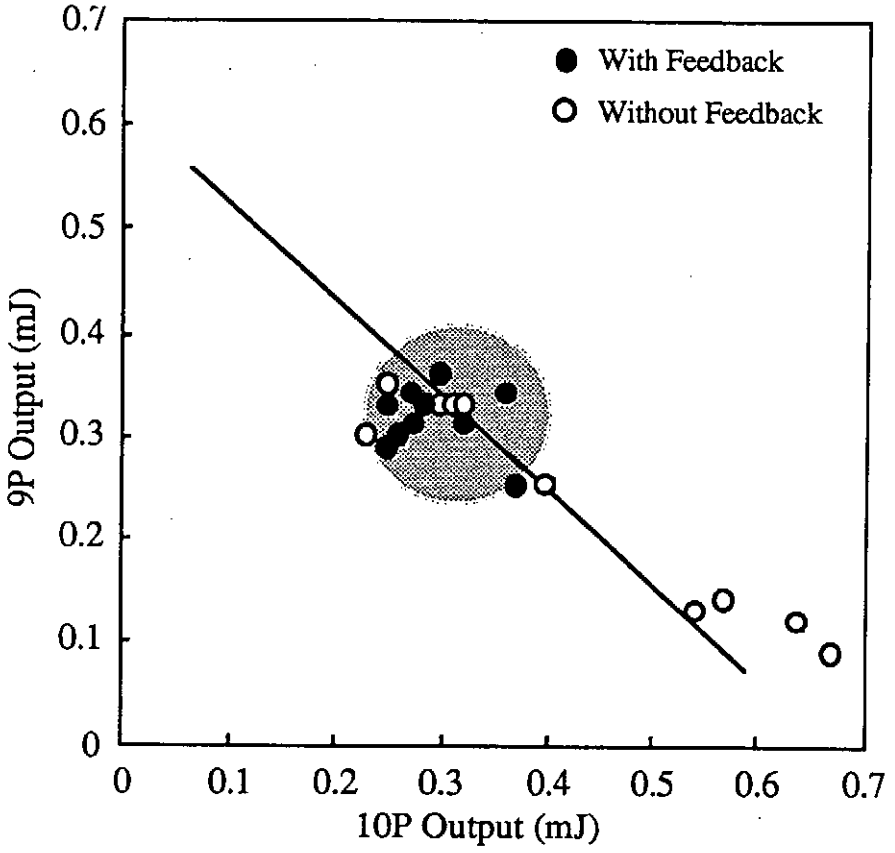

Fig. 7. 10P(20) and 9P(22) output balance.
Shadow indicate area of $\sigma \geq 90\%$

The large-amplitude plasma wave is driven by the ponderomotive force, i.e., the two wave product $\alpha_1\alpha_2$, as

$$A(t) = A(0) + \frac{1}{4}\alpha_1\alpha_2(w_p / k_0)t, \tag{1}$$

Where $\alpha_j \equiv eE^{(j)}/m\omega_j c$, j=1, 2 [4]. Also its saturated amplitude becomes

$$Ak_0 = \left(\frac{16}{3}\alpha_1\alpha_2\right)^{\frac{1}{3}}, \tag{2}$$

Thus, rather a product of the two lines is required than each line intensity or balance, so that we, here, define the output balance of the double line as:

$$\sigma \equiv \frac{4(10P)(9P)}{\{(10P)+(9P)\}^2}, \tag{3}$$

where (10P) and (9P) denote the output of the 10P and 9P line, respectively.

σ of 90%, we think, is enough for the beat-wave excitation, which means that (10P):(9P)=6:4 or 4:6. The fraction of σ ≥90% is about 50% of the whole shots without feedback(open circle), while the fraction of σ ≥90% becomes higher than 90% with feedback(closed circle in the shadow).

§4. Results

[1] Using the PZT driven mirror, we succeeded in keeping the cavity length constant.

[2] Feedback-controlling the PZT, we obtained stable double line output (σ ≥90%).

[3] The shot rate of σ ≥90% is 50% without feedback, and higher than 90% with feedback.

We will be able to experiment on Beat-Wave Acceleration efficiently.

Acknowledgement

We acknowledge useful discussions with C. Clayton of UCLA and Y. Sakawa, Nagoya University.

Reference

(1) Y. Kitagawa, K. Sawai, K. Matsuo, K. Morioka et al., Phys. Rev. Lett., **68**, 48(1992).

(2) C. Yamanaka et al., IEEE J. Quantum Electronics, **QE-17**, 1678(1981).

(3) Vas. DEV et al., Optics Communications, **65**, 5(1988).

(4) M.N. Rosenbluth and C.S. Liu, Phys. Rev. Lett.,**29**, 701(1972).

Development Electron Beam Source for Beat-Wave Acceleration

K. Morioka, K. Sawai, Y. Kitagawa, K. Matsuo, and S. Nakai
Institute of Laser Engineering, Osaka University
Yamada-oka 2-6, Suita, 565, Japan

§1 Introduction

A beat wave of double line CO_2 laser (10.6μm, 9.6μm) has excited a relativistic plasma wave of amplitude δn/n~5%. Then the plasma wave trapped and accelerated plasma electrons[1]. Since the wave of δn/n~5% needs an electron beam not less than 1MeV to trap and accelerate. Also, we need to synchronize a electron pulse with a laser pulse of 1ns width. Nevertheless, the electrical synchronization in the present system is difficult to avoid 20-ns jitter, which demands us to prepare at least a few-ns-rise and few-tens- to 100-ns-wide electron beam. So we have tried to develop an electron beam of 1MeV and the pulse width of ~100ns. We present here the results of the beam development and the beam characteristics.

§2 Design and development of electron beam source

Experimental set up for the electron beam source as well as the beat-wave acceleration is shown in Fig.1. The beam source consists of a capacitor bank of 640kV-0.02μF and a gun diode and its equivalent circuit is shown in Fig. 2. A 4-atm-SF_6 gas-gap switch fires the bank with an electrical trigger, and an 100ns electron beam pulse of about the bank voltage is transported to a carbon diode in a gun chamber by a 45-m 56-Ω coaxial cable. The bank output voltage and current wave forms are shown in Fig. 3.

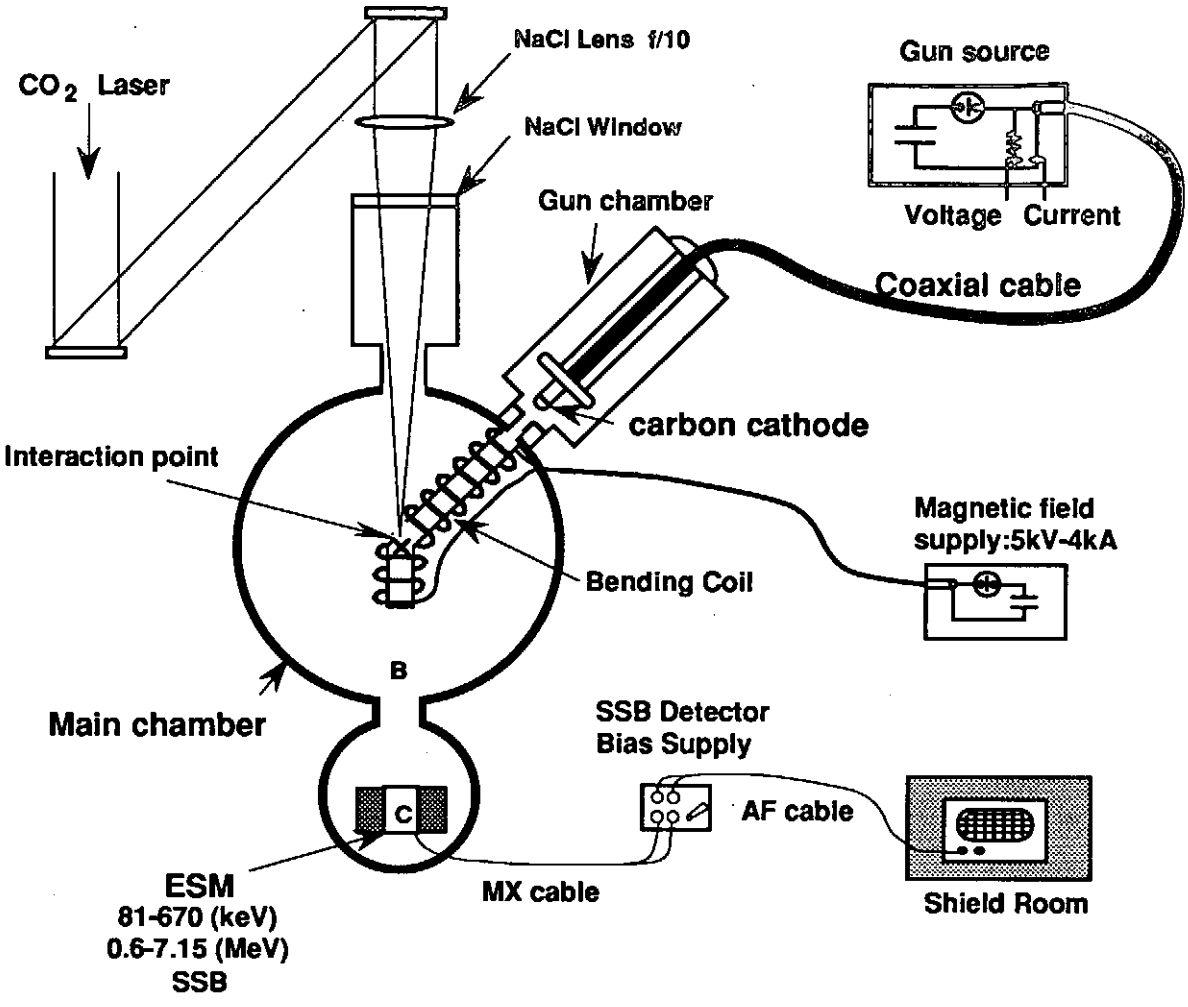

Fig. 1. Set up of electron beam source for beat-wave acceleration

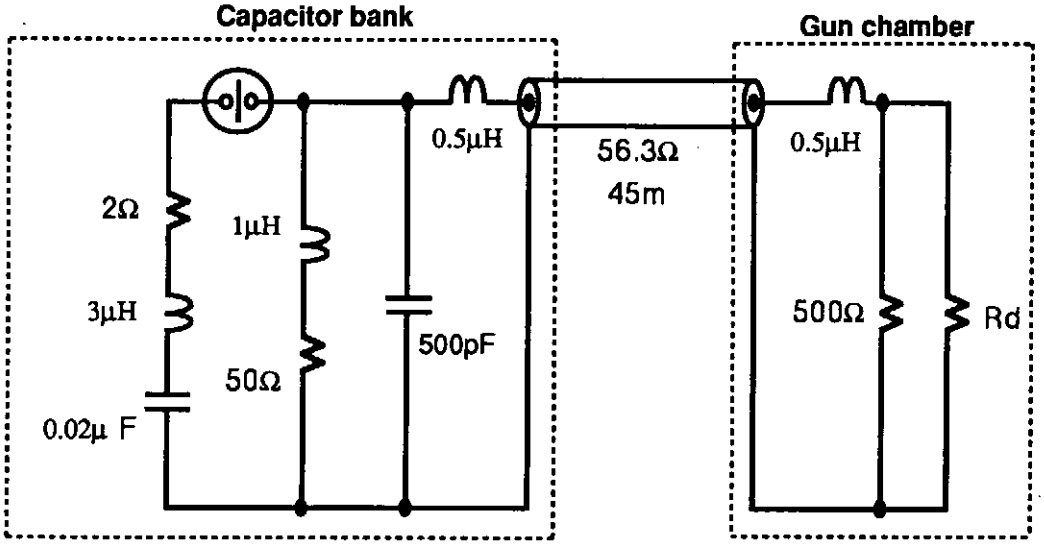

Fig. 2. Equivalent circuit diagram of electron beam source, Rd:diode impedance.

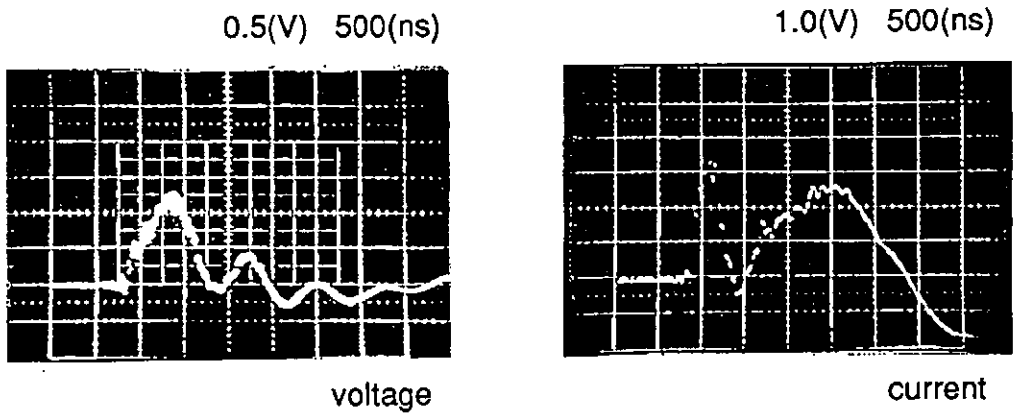

Fig. 3. Output voltage and current wave forms of capacitor bank for 320kV charge.

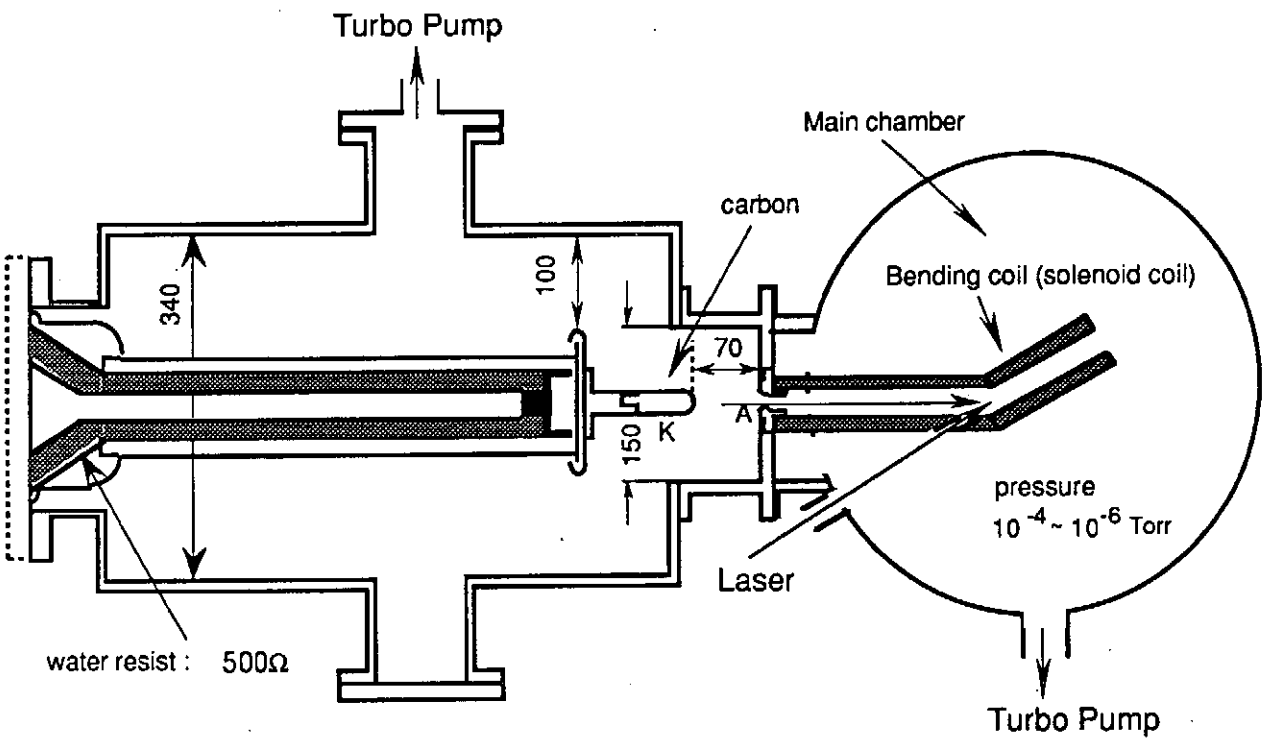

Fig. 4. Gun chamber

The gun chamber is shown in Fig. 4. Two turbomolecular pumps evacuated gun and main chambers to 10^{-4}~10^{-6} Torr, respectively. A numerical simulation has predicted that a charging voltage of 640kV implies a diode voltage of 750kV with 200ns rise, supposed the diode impedance of 500Ω, much higher than the bank or the cable. We, therefore, designed the diode as that the cathode head is hemisphere of 12.5mm radius and the distance to the cathode is 70mm and the anode hole is 10mm in diameter, to make the diode

impedance much higher than 50Ω enough to reflect an input pulse back to the bank. This design will result in yielding higher emitted beam energy than that expected from the bank voltage. That is, we expected the electron beam of >1MeV from the bank voltage of ~500kV.

A bending solenoidal coil guides the emitted beam to the center of the main chamber and bends it by 30° to align with the laser beam. The coil is driven by a 200μs-pulse current, and the peak field attains to 1T and focuses the beam diameter to less than 5mm.

§3 Measurement of electron beam energy

We measured the emitted electron beam energy by using two electron spectrometers(ESM). The one ESM covers the energy from 240 to 670keV and the other from 0.6 to 7.15MeV. A rare-earth-cobalt dipole magnet bends the electrons by 180°. The detector consists of 5-channel silicon surface barrier detectors (SSB) of EG&G ORTEC. Since an electron pair creation needs 3.6eV in the silicon active area, one injected electron of 1MeV, for instance, creates 2.8×10^5 electron pair, or 8.9×10^{-14}C. An 0.6MeV electron yields 5.3×10^{-14}C. The time resolution of the SSB is <3ns.

Figure 5 shows the ESM signals from 0.6 to 5.63MeV for the charging voltage of 480kV and the bending coil field of 0.5T. The distance between the bending coil end and the ESM is 7.8cm(point "B"). To protect x-rays and electrons from hitting directly the SSB, we put a lead(Pb) block with a hole of 6mm diameter in front of the ESM. For both the 0.6MeV and 1.1MeV signals, the rise time and the pulse width are ~100ns and ~150ns, respectively. Note that the signal timing and pulse width agree exactly with those of the first peak of the bank current, as seen in Fig.3. The output of 1.1MeV channel is about 3nC, yielding the number of the injected electrons to be about 3.3×10^4. At the end of this section we will discuss the current necessary for the beat-wave acceleration. The 0.6MeV output of ~6nC yields the injected electrons of $\sim1.1\times10^5$. No true signals are detected at the 2.59MeV or more channels.

To check whether the 1.1MeV signal is true electron or spurious, since 1.1MeV is twice the charging voltage(480kV), we put the ESM far at 63cm(point "C"). Figure 6 shows ESM signals for the charging voltage of

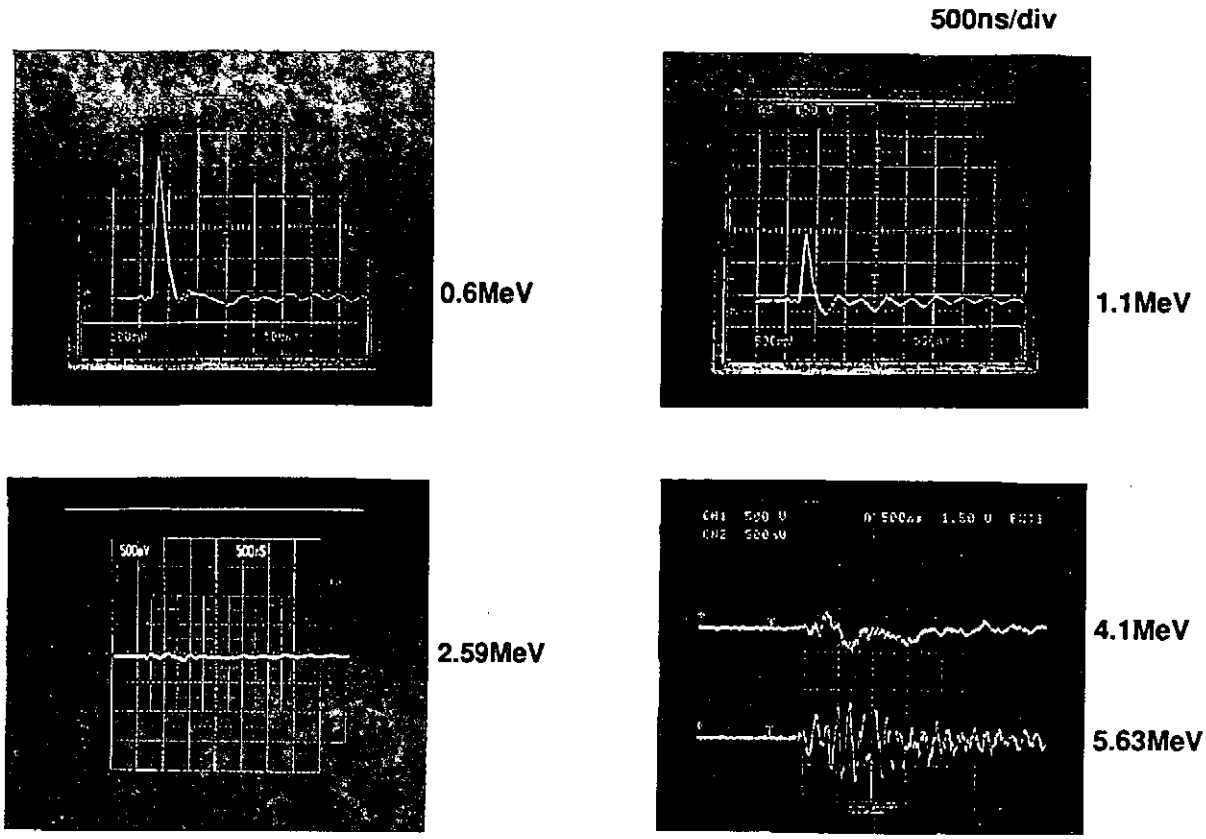

Fig.5 ESM output signals at 7.8cm for 480kV charge and the field of the bending coil of 0.5T.

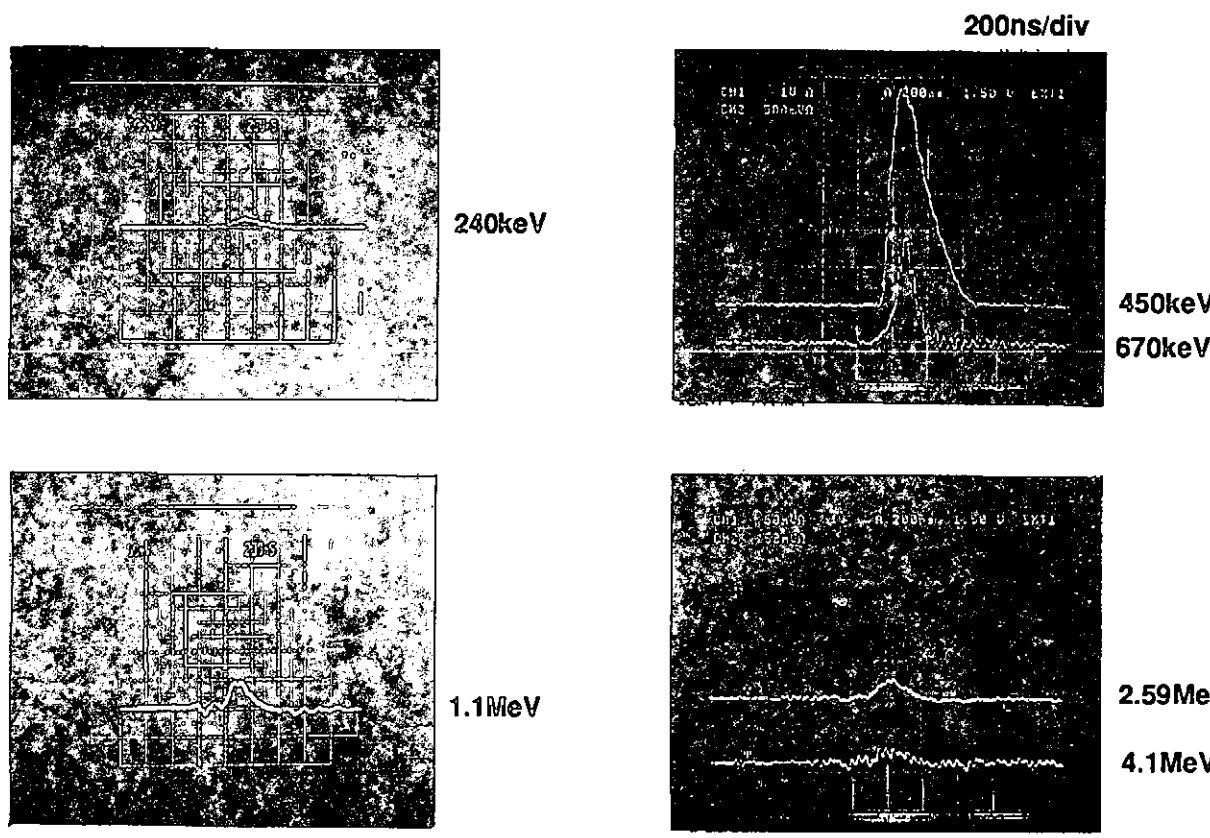

Fig.6 ESM output signals at 63cm for 640kV charge and the field of the bending coil of 0.75T.

640kV and the bending coil field of 0.75T. The lead block is not used this time. The signals of 0.45 to 1.1MeV will be true, since those signals decrease as increasing the distance, but the signals of 2.59MeV and more will be noise, because the signal levels are the same order of those in Fig. 5, from which we fixed the noise levels. Furthermore, by putting a bending magnet in front of the ESM and by using an aluminum foil to filter the low energy electrons out, we confirmed that the 1.1MeV signal is true.

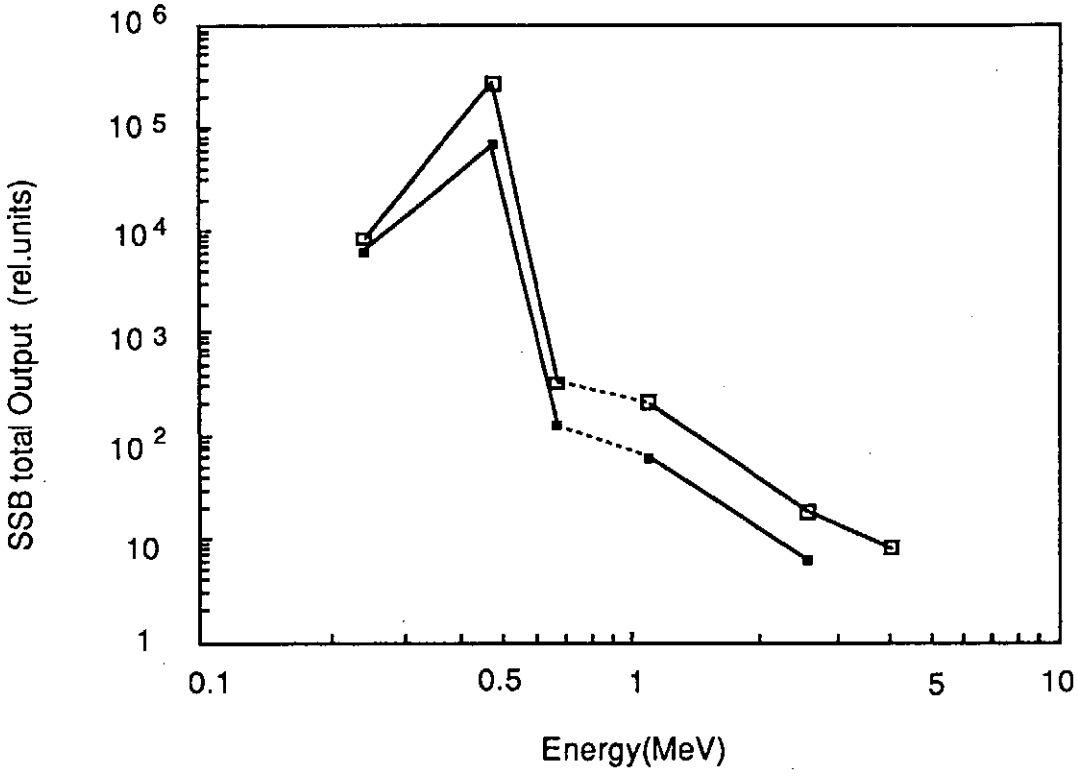

Fig. 7 Energy spectrum of the electron beam. Magnetic field of the bending coil is 0.75T. Data from 240keV to 670keV and data from 1.1MeV to 7.59MeV are from different ESM, respectively; the charging voltages is 560kV (■) and 640kV (□).

The energy spectrum at 63cm, thus obtained, is shown in Fig. 7 for the charging voltage of 560kV and 640kV. Broken lines connect two different energy regions. 200μm-aluminum filters are put on the SSB heads both at 450keV and 670keV channels. The difference between two charging voltages is within the detector resolution, so that both the peaks are reasonably seen at around 450kV. The 1.1MeV point is one order higher than the noise level of about 50 for 640kV, as seen in the figure. where the SSB output of 1000 corresponds typically to 78pC.

Since the 150ns- and 5mm-diam.- electron beam cannot interact but with a 1ns- and 0.3mm-diam.- laser light, in order to accelerate at least one 1MeV electron the number of the beam electrons should be larger than 4.2×10^4. Though this condition is marginally satisfied now, the beat-wave experiment might demand one hundred time stronger beam to overcome the recent plasma electron acceleration result[1].

§4 Conclusions

1) We succeeded in developing the electron beam source for the beat-wave acceleration.
2) We obtained 1MeV or more electron beams by charging the capacitor bank with 640kV or less.
3) The beam characteristics are:
   The rise time is ~ 100ns and the pulse width is ~150ns.
   The number of the electrons injected into the SSB is
   $\sim 1.1 \times 10^5$ for 500keV and
   $\sim 3.3 \times 10^4$ for 1.1MeV.

We will soon accelerate the 1MeV electron beams by the laser beat wave.

References

[1]Y. Kitagawa, K. Sawai, K. Matsuo, K. Morioka et al., Phys. Rev. Lett., **68**, 48(1992).

[2]A. Kawabata, *"Electronic Materials. Components and Materials Analysis"*, 7th edition, PP57-62.155-202, 1989, Corona Publishing.

Observation of Beam Energy Shift Caused by Plasma Wakefield

A. Ogata, A. Enomoto, K. Nakajima, H. Nakanishi
KEK, National Laboratory for High Energy Physics
Oho,Tsukuba 305 Japan
T. Shoji
Plasma Science Center, Nagoya University
Chikusa-ku, Nagoya, 419-11 Japan
Y. Nishida and N. Yugami
Department of Electrical and Electronic Engineering, Utsunomiya University
Ishi-machi, Utsunomiya 321, Japan

Abstract

The energy shifts of linac electron beams caused by the plasma wakefield were measured in plasmas with density on the order of 10^{12}cm^{-3}. The linac provided a sequence of several bunches which generated wakefield in a plasma. The wakefield in turn caused the energy change in bunches. Data processing taking account of the finite bunch length which was comparable, or even longer than, the plasma wavelength tells that the observed energy change, if converted into the values at the bunch center, amounted to $\sim 20\text{MeV/m}$ in certain cases. The energy spectra were qualitatively consistent with calculations. The buildup of the wakefield was not obvious after the maximum bunch.

1. Introduction

A plasma wakefield accelerator (PWFA) is one of the plasma-based-type accelerators showing promise to produce ultrahigh accelerating gradients which are necessary in the next generation of particle accelerators, and it is the only one among them that has demonstrated the acceleration of bunched electrons.[1] In the PWFA, a high-intensity relativistic electron bunch excites a large amplitude plasma wave with a phase velocity equal to the light velocity, which, in turn, accelerates a trailing low-intensity test bunch.[2]

Our experiments on the PWFA was conceived by the use of a high-intensity electron beam for the positron production in the KEK linac.[3] The linac provides us with a sequence of multiple bunches which generate wakefields in a plasma to accelerate or to decelerate trailing bunches. Analysing the energy of each bunch, we can observe the energy transfer between the bunches through plasma waves without a test charge beam. The theory tells us that the plasma wakefields are enhanced at certain plasma frequencies which are resonant with the linac bunch frequency. Because the plasma frequency is determined by the plasma density, we can probe the resonances by controlling the plasma density. The preliminary experiments have reported[3,4] an energy

shift of 12MeV at the maximum in a low density plasma of the order of 10^{11}cm^{-3}. The obtained energy shifts are consistent with, or even larger than, the values predicted by the linear theory.[3]

The present paper describes experiments in a plasma with the density on the order of 10^{12}cm^{-3}. The next section describes experimental apparatus, *i.e.*, the linac and plasmas. Section 3 inspects what the linear theory predicts when our experimental parameters are applyed. Results of experiments are given in section 4, in terms of energy shifts and energy spectra. Two major findings are 1) energy shifts larger than the prediction in first and second bunches, and 2) no wakefield buildup after the third bunch. The discrepancies between the prediction is discussed in section 5. The last section contains conclusions.

2. Experimental apparatus

In the KEK PF electron linac for positron generation, a beam emitted by a gun is compressed to less than 2nsec in a sub-harmonic buncher. The 2856MHz rf buncher then separates the 2nsec pulse into a train of 6 bunches with a 350psec, or 0.104m spacing. They are then accelerated up to $\sim$ 500MeV. Bunches with a total charge of $5-10$nC are focused on a plasma by a quadrupole triplet at the end of the linac. The rms radius and length of the bunches are around 1mm and 3mm, respectively.

The plasma chamber has a diameter of 50mm and a length of 1m with a $0.5-1$kG solenoid magnetic field. The plasma of unit length gives the plasma wakefield directly in MeV/m unit. Ionization is realized by a helicon wave,[5] which is excited by a $5-10$MHz and 1kW rf wave fed through a helical antenna. The discharge pulse has a duration of 10msec and a rate of 0.5Hz equal to the linac beam rate. Argon gas is fed through a gas-flow controller to maintain a neutral gas pressure of $4-8\times10^{-4}$torr for a plasma density of $2-8\times10^{12}$cm^{-3}.

A Langmuir probe measures the plasma temperature and density at the longitudinal and radial center of the plasma. Besides the standard Langmuir probe, current to a titanium end plate of the plasma chamber was sometimes used to diagnose the plasma temperature and density. A PCD array combined with 488nm filter was also used to measure the transverse plasma profile. The plasma temperature ranged $2-5$eV, and the rms plasma radius was around 5mm. The plasma density is controlled by changing the gas flow rate, the solenoidal magnetic field and/or the rf power.

A combination of a bending magnet and a streak camera makes it possible to measure the energy spectrum of each bunch. Bunches analyzed in the bending magnet travel in air over a length of 0.5m to a mirror, while radiating Cherenkov radiation. The mirror reflects only the radiation, transmitting the electron beam. The reflected radiation is finally focused on the streak camera. Since the energy aperture of the magnet is only 15MeV, it cannot cover the energies of all the bunches. So we inserted a slit in front of the streak camera and swept the analyzing field.

Integration of each energy spectrum gives the bunch intensity of each bunch.

We found that the total charge was distributed among the six bunches by the ratio approximately 0.0781 : 0.297 : 0.269 : 0.232 : 0.103 : 0.018 in the present experiment. The standard deviation of each bunch intensity was about 25% calculated from 40 energy spectra. The reproducibility was not assured if an intermission, usually longer than 30min, was taken during the linac operation. These ratios are depicted in the figures of this paper occasionally.

3. Predictions of linear theory

Let us first examine what the linear theory predicts.[3] If all the bunches and the plasma are on axis, the resultant wakefield is linear summation of the individual wakefield, which is a function of both the plasma density and the position. The position dependence is given in Fig. 1, and the density dependence is given in Fig. 2. In the calculation of these two figures, it is assumed that the total charge of 10nC is distributed by the ratio already described, and that each bunch has longitudinal Gaussian distribution with standard deviation of 3mm, and transverse parabolic distribution with radius of 1.4mm, which is eqivalent to the standard deviation of 0.75mm in Gaussian distribution if normalized by the total area.

Figure 1 shows the predicted amplitude of the longitudinal wakefield on the axis at certain plasma density, *i.e.*, $n_e = 5.05 \times 10^{12}\mathrm{cm}^{12}$, as a function of the longitudinal position. One can consider this as a time evolution of the wakefield. Bunch positions and their intensities are also given here. Black lines in Figure 2 show the prediction of the amplitude of the longitudinal wakefield at each barycenter of a bunch, as a function of the plasma density.[3] At resonant densities where $\omega_p = n\omega_{rf}$ with integer n, all bunches are decelerated to produce the maximum amplitude of wakefield behind the bunch train. Figure 1 is a case where a resonant condition $n = 7$ is satisfied. If we could inject a test bunch when the wakefield is maximum-positive, we could demonstrate most effective acceleration, though it is impossible in the present setup.

In the next section, we will show the experimentally-obtained barycenter energy shift caused. In the plasma with density of $\sim 10^{11}\mathrm{cm}^{-3}$, we have observed the barycenter energy differences almost equal to the peak of the plasma wakefield.[3] However, in a denser plasma as in the present experiments, we have to take account of the fact that the bunch length is comparable to, or even longer than, the plasma wavelength. Figure 1(b) shows the plasma wakefield around the third bunch together with the longitudinal bunch shape, when the density is $5.05 \times 10^{12}\mathrm{cm}^{-3}$. Though the main body experiences decelerating field, the head and tail experience accelerating field. In addition, bunches have finite size also in the radial direction. The observed barycenter energy shifts should fit to the averaged wakefield over the bunch volume.

This averaged wakefield was calculated under following assumptions and shown by gray lines in Fig. 2. What assumed are that 1) the energy distribution in the absense of a plasma is Gaussian and independent of the longitudinal distribution, and that 2) a plasma modifies the energy distribution without changing the longitudinal distribution.

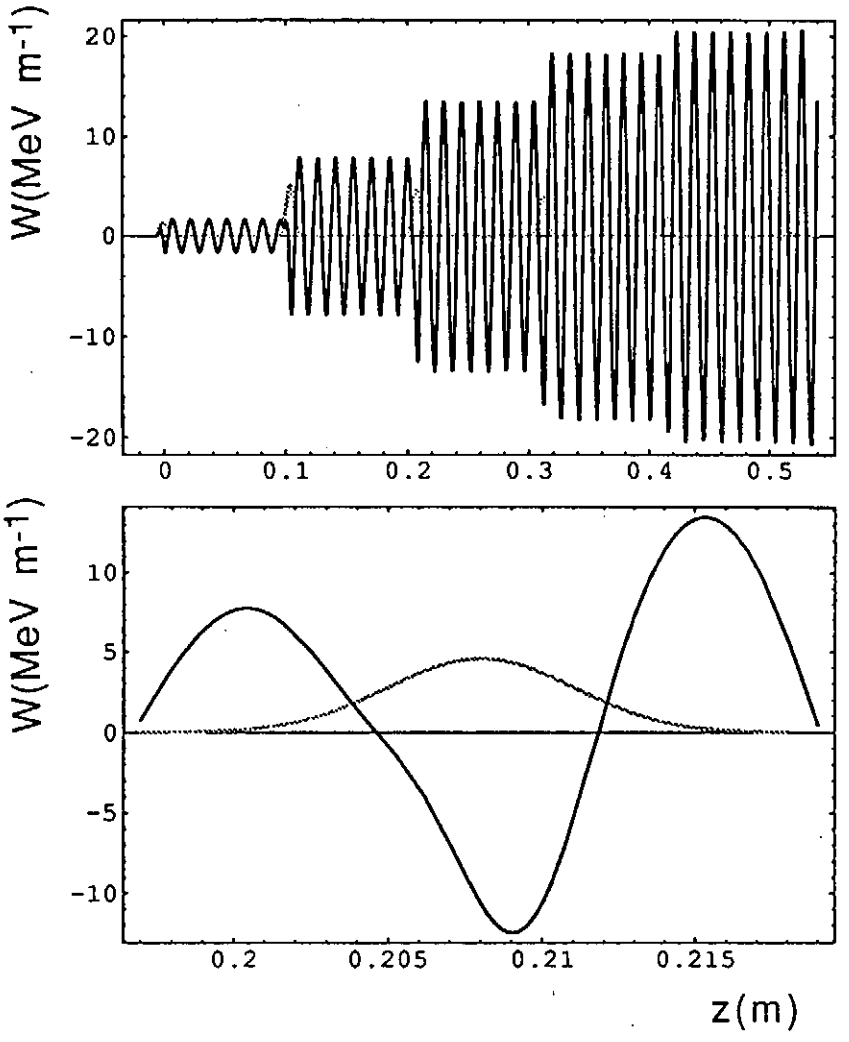

Figure 1: (a)The amplitude of the longitudinal wakefield at $n_e = 5.05 \times 10^{12}\mathrm{cm}^{-3}$ on the axis as a function of longitudinal position. (b)Enlargement of (a) around the third bunch.

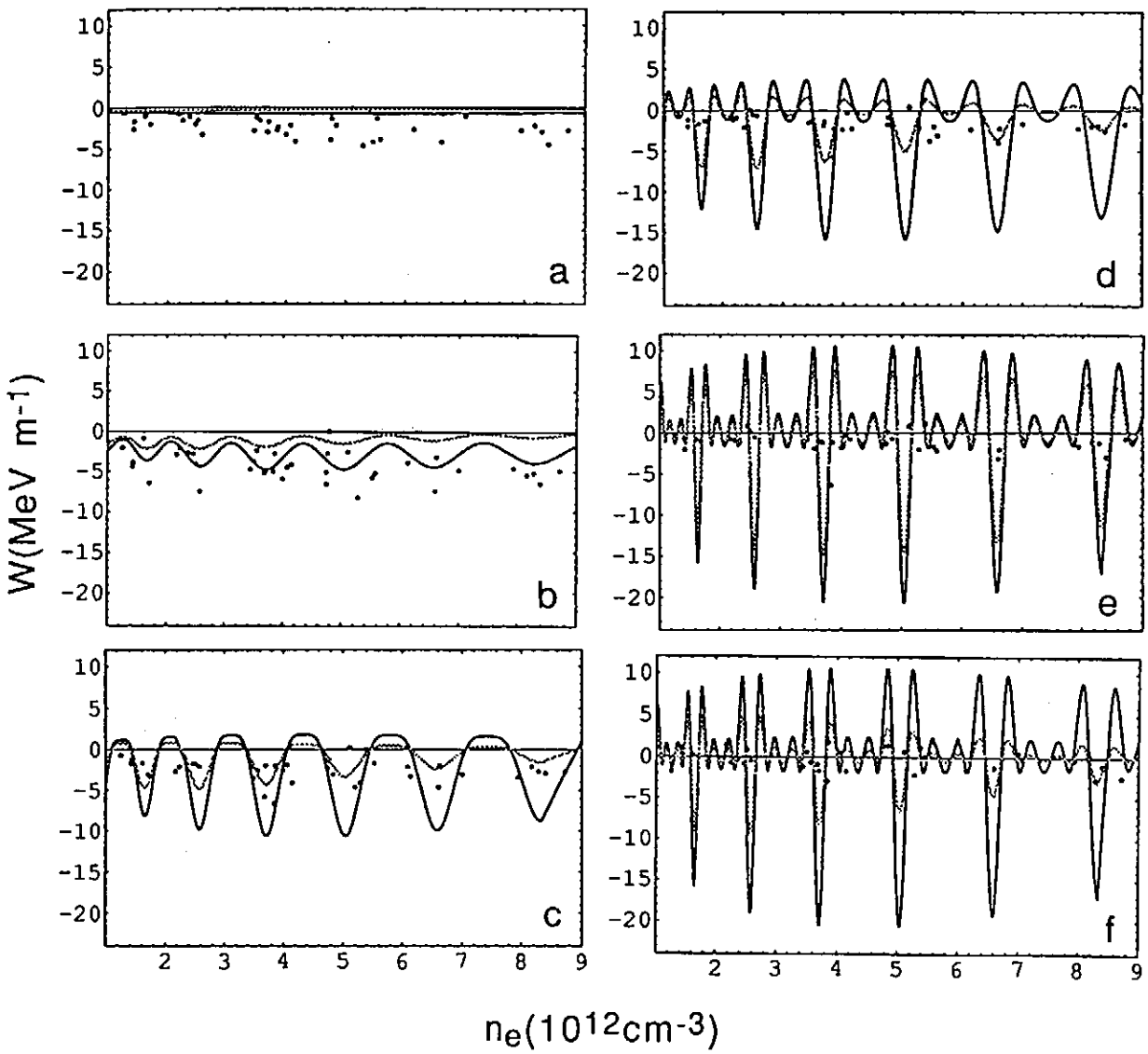

Figure 2: The amplitude of the longitudinal plasma wave. Black lines show calculated value at the bunch centers, gray lines show calculated values averaged over the bunch volume, and points show the observed values. (a) first bunch, (b) second bunch, (c) third bunch, (d) fourth bunch, (e) fifth bunch and (f) sixth bunch.

4. Experimental results

4.1. Energy Shift

Barycenter differences between experimentally-obtained energies with and without the plasma were calculated for all the bunches as a function of the plasma density, which are also shown in Fig. 2. Because the Langmuir probe cannot afford the absolute plasma density correctly, the conversion coefficient from the probe voltages to the plasma densities is adjusted so that the resultant plasma frequencies of the third bunch show resonances where the theory predicts. The scattering of the data points is mainly due to the timewise non-uniformity of the plasma density. Spacewise, the longitudinal uniformity is not assured. Though the variation during the time for the bunches passing the plasma is negligible, the variation during the scanning of the magnetic field of the energy analyser, which requires about 50 linac beams, often amounts to $10^{11}\mathrm{cm}^{-3}$. It should be noted that the spacewise uniformity in the longitudinal direction was neither assured.

The agreement between the calculation and the experiments in Fig. 2 is poor. The observed enrgy shifts are larger than the calculation (gray lines) in the first three bunches, comparable to the calculation in the fourth bunch, and smaller in the fifth and sixth bunches. In the first two bunches, the observed energy shifts are even larger than the calculated wakefield at the bunch center (black line). Some data suggest that the wakefield at the bunch center exceeds $20\mathrm{MeVm}^{-1}$ in the second bunch.

The buildup of wakefield in a train of bunches is considered to be useful in order to increase the transformer ratio.[7] However, Fig.2 denies the buildup of the wakefield at least in the third through sixth bunches. Similar phenomenon has already been found,[4] where a bunch with the maximum intensity showed appreciable energy shift, while the bunch following just after this maximum one made no energy change. We have no database to judge whether this is due to only technical problems, physical ones, or both. Technical problems include a fact that the bunches were not on a same axis because of the transversal wakefield,[6] the result of which is discussed in the next section. The small plasma radius ($\sim$ 5mm) made this more serious. The physical problems include some nonlinear mechanism.

4.2. Energy spectra

Let us examine the experimentally-obtained energy spectra in detail. We will first pay attention to barycenter energies in the absence of a plasma. It was found that the latter bunches have the smaller barycenter energies. This is because of the wakefield caused by the interaction between bunches and the linac structure; the latter bunches are more decelerated by the wakefield built up by the preceding bunches. This wakefield in the absence of a plasma is calculated and shown in Fig. 3 as a function of longitudinal position.[8] Experimantally-obtained barycenter energy of each bunch is also given. In the calculation, only the fundamental mode was taken into account, and

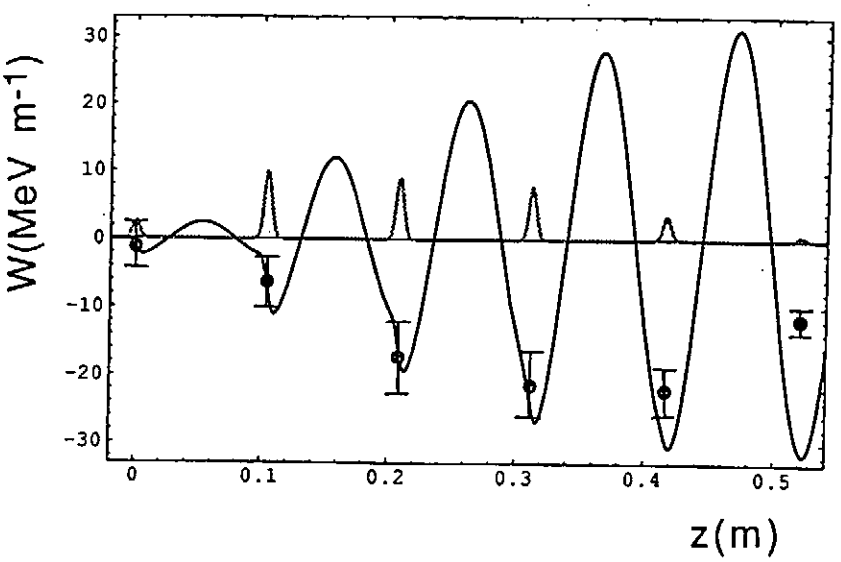

Figure 3: Longitudinal wakefield caused by the linac structure and the observed barycenter energies of the bunches.

the loss factor was assumed to be $3.75 \times 10^{13}\mathrm{VC}^{-1}\mathrm{m}^{-1}$ according to ref.8. The linac length is 80m and the initial beam energy was assumed to be 470MeV.

The agreement between the experiments and the theory is excellent in first three bunches, but deteriorates gradually in the latter bunches. This is probably because the latter bunches are off-centered by the transverse wakefield also characteristic to the linac structure.[6] This must contribute to the fact shown in Fig. 2 that the wakefield does not build up in the latter bunches.

Figure 4 gives three pairs of energy spectra with and without a plasma for the first three bunches at $n_e = 5.2 \times 10^{12}\mathrm{cm}^{-3}$. The data points show the observed values, while the gray lines are the results of trial to explain these distributions. Let us begin from the case of no plasma. We first assumed that the longitudinal distribution of a bunch was Gaussian as shown in Fig. 5(a). Hitherto measurements using a streak camera support this assumption. Next, it was assumed that the dependence of the beam energy upon the longitudinal position was governed solely by the wakefield caused by the linac structure, which has already been shown in Fig. 3, but enlarged and shown again here by the black line in Fig. 5(b) as the beam energy dependence on the distance along the beam axis for the third bunch. We can imagine that Fig. 5(b) shows three-dimensional diagram in the (z, E) phase-space, the third axis of which shows population; the mapping of this diagram onto z-axis is Fig. 5(a), the Gaussian distribution. If we map it onto the another axis, we can generate the energy spectrum of the third bunch, which is given by a gray line in upper box of Fig. 4(c).

The plasma excites its own wakefield in the third bunch, which was calculated and shown in Fig. 5(c). The bunch feels both the wakefield of the structure (the black line of Fig. 5(b)) and this plasma wakefield. The total is shown by the gray line in Fig. 5(b). From this gray line and the assumption of the Gaussian distribution, we can reconstruct the energy spectrum, which is shown by the gray line in lower box of Fig. 4(c). Figures4 (a) and (b) are also derived by the same procedure.

The first bunch has broader spectra than predicted. The second bunch has a high energy tail in the absence of the plasma, which is wiped out by the plasma. This is a phenomenological reason why the barycenter difference with and without the plasma is larger than predicted. Aside from these observations, the calculation well predicts the absolute positions and widths of the spectra macroscopically in the second and third banches. Microscopically, we find that the calculated energy spectra have steep cut-off edges at the low-energy side. This is due to the assumption that the distributions in the (z, E) phase space were given by lines, which were not unique-valued but often folded in the low-energy side. Actual distribution should have width around the lines to broaden the spectrum.

5. Discussions

The previous section reports two findings. One is that the buildup of wakefield was not successful at the third through sixth bunches. It is probably because all the

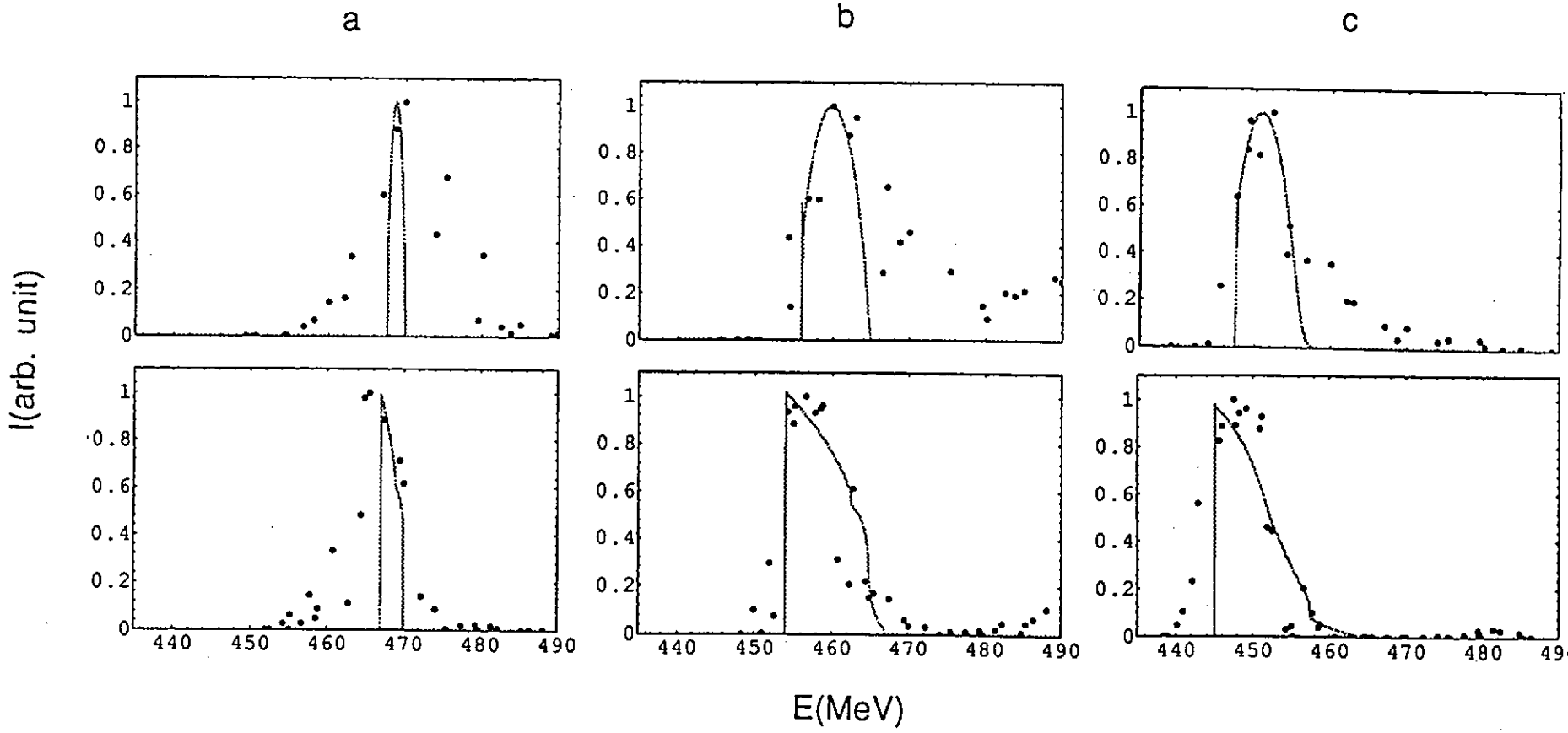

Figure 4: Energy spectra of the first three bunches in the absence of a plasma(upper) and in the presence of the plasma(lower) with density of $n_e = 5.2 \times 10^{12}\mathrm{cm}^{-3}$. Data points show experimentally-obtained, while gray lines show theoretical. (a)first bunch, (b)second bunch and (c)third bunch.

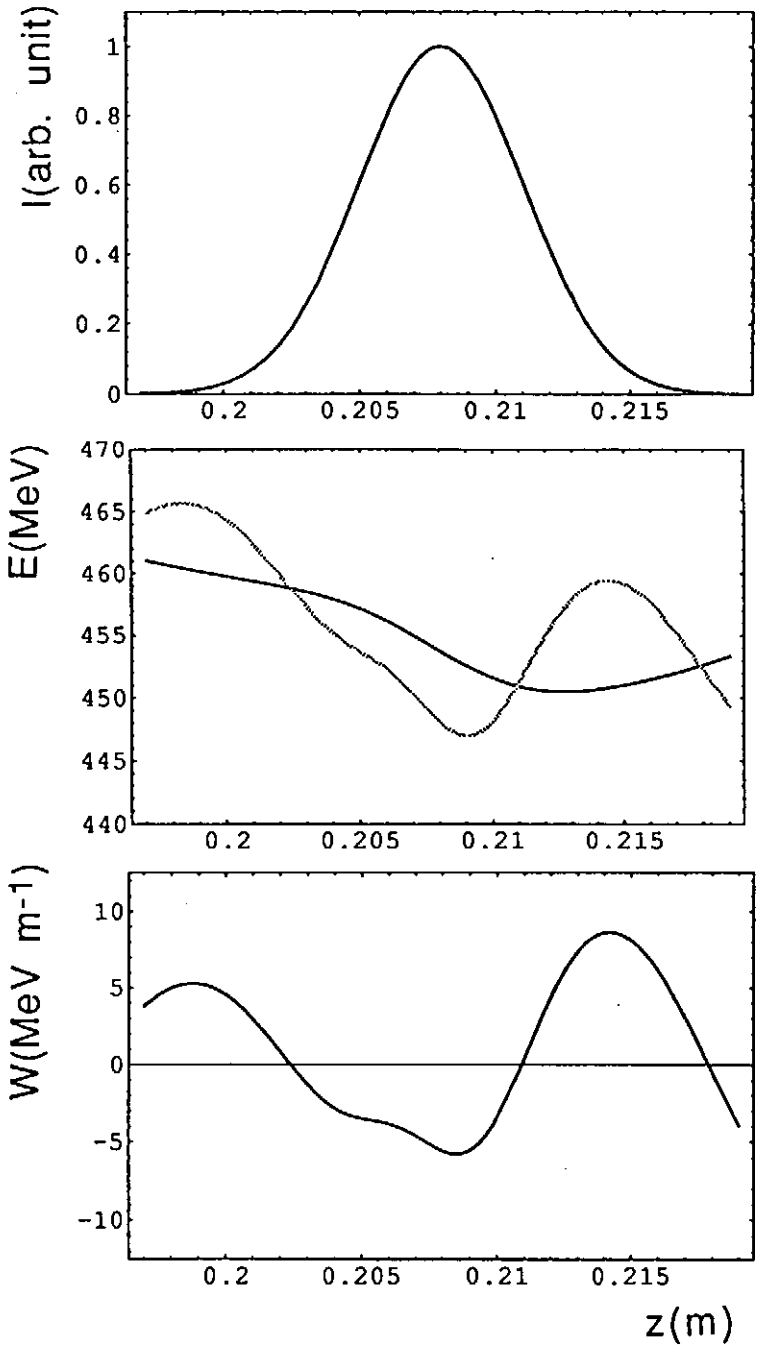

Figure 5: (a)Longitudinal particle distribution of the third bunch. (b)Beam energy dependence on the distance along beam axis. The black line shows the case without a plasma, while the gray line shows the case with the plasma of $n_e = 5.2 \times 10^{12}\mathrm{cm}^{-3}$. (c)Wakefield change caused by a plasma of $n_e = 5.2 \times 10^{12}\mathrm{cm}^{-3}$.

bunches were not on the same axis. If a trailing bunch is not on the same axis with the driving bunch, the longitudinal wakefield felt by the trailing of course becomes weak.

One may suspect that the radial plasma wakefield of the driving bunch further kicked the trailing bunch, as the wakefield of the linac structure did,[10] which further weakened the longitudinal wakefield felt by the trailing bunch. This effect certainly exists. However, because the radial force is decreased down to $1/\gamma$, which is $\sim 1/1000$ in our case, it is negligible.

It should be noted that this effect could be serious if both the number of bunches and the plasma length l were large, because the displacement of the n-th bunch is proportional to l^{n-1}. In the conventional linac structure, because the wavenumber can be characteristic to each bunch and can be different each other, the displacement cannot grow infinitely but only oscillate. This is called "Landau damping" by accelerator physicists.[10] In the case of the PWFA, we have only one wavenumber k_p, so we cannot rely on the Landau damping to treat the displacement.

The other finding of large energy shifts in the preceding two bunches is puzzling. The following speculation excludes the possiblity of nonlinear mechanism: The perturbed electron density must be approximately equal to the average electron density in a bunch, which is $\sim 5 \times 10^{11}\mathrm{cm}^{-3}$ if the charge of the bunch is 1nC. This value is smaller than the background density by a order of magnitude in these experiments. The self-focusing of the driving bunch can lead to the increase of the longitudinal wakefield, but this self-focusing is weak in our high γ bunches.

One may suspect the existence of bunches preceding to the first one, whose energy shifts are extraordinary large. Certainly, we have not scanned the streak camera once after we found the bunches. The existence of large preceding bunches are, however, not probable, because 1) the linac equips with a subharmonic buncher which compresses the width of the bunch train to less than 2nsec, 2) hitherto experience tells that, even if some spilled-out bunches exists, they make not head but tail, and 3) the observed plasma-density dependence (Fig. 2 (a)) is noisy but no resonant structure is found as in other bunches.

One comment should be made on the correlation between two distributions in the absense of a plasma; the longitudinal distribution and the energy distribution. We have fully neglected the correlation in calculating Fig. 2, while assumed the full correlation in calculating Fig. 4. The truth must exist somewhere between these two assumptions. It should be noted, however, that the plasma causes only the broadening in the energy spectra if we neglect the correlation in the absence of the plasma.

6. Conclusions

We have measured the plasma wakefiled caused by a sequence of bunches in plasmas with the density on the order of $10^{12}\mathrm{cm}^{-3}$, where the plasma wavelength is comparable, or even shorter than, the bunch length, 3mm. Data processing taking account of the bunch length has shown that the experimentally-obtained wakefield

was often larger than the prediction of the linear theory, which sometimes exceeded $20\mathrm{MeVm}^{-1}$ on the beam axis. The buildup of wakefield was not observed after the bunch with the maximum intensity appeared, probably because the trailing bunches were displaced when they entered the plasma.

References

1. J. B. Rosenzweig, D. B. Cline, B. Cole, H. Figueroa, W. Gai, R. Konecny, J. Norem, P. Schoessow and J. Simpson, Phys. Rev. Lett. 61 (1988) 98.
2. P. Chen, J. M. Dawson, R. W. Huff and T. Katsouleas, Phys. Rev. Lett. 54 (1985) 693.
3. K. Nakajima, A. Enomoto, H. Kobayashi, H. Nakanishi, Y. Nishida, A. Ogata, S. Ohsawa, T. Oogoe, T. Shoji and T. Urano, Nucl. Instr. and Meth. A292 (1990) 12.
4. A. Enomoto, H. Kobayashi, K. Nakajima, H. Nakanishi, Y. Nishida, A. Ogata, S. Ohsawa, T. Oogoe, Y. Suetsugu and T. UIrano, *Proc. 2nd. Eur. Part. Accel. Conf.*, Nice, 1990, (Editions Frontieres, 1990), P634.
5. R. W. Boswell, Plasma Phys. Controlled Fusion 26 (1984) 1147.
6. Y. Ogawa, T. Shidara and A. Asami, Phys. Rev. D43 (1991) 258.
7. K. Nakajima, Part. Accel. 32 (1990) 209.
8. K. L. F. Bane, P. B. Wilson and T. Weiland, in *Phys. High Energy Particle Accelerators,* AIP Conf. Proc. No.127, (Am. Inst. Phys., New York, 1983) p875.
9. M. Takao, Y. Ogawa, T. Shidara and A. Asami, *Proc. 1991 IEEE Particle Accelerator Conference*, to be published.
10. T. Suzuki, in *Advanced Accelerator Concepts,* AIP Cof. Proc. No.156, (Am. Inst. Phys., New York, 1987) p480.

Plasma Wakefield Acceleration Experiment By Using Twin Linac System

Y. Yoshida, T. Ueda, T. Kobayashi and K. Miya

Nuclear Engineering Research Laboratory, Faculty of Engineering, University of Tokyo,
22-2 Shirakata Shirane, Tokai-mura, Naka-gun, Ibaraki 319-11

A. Ogata, H. Nakanishi, K. Nakajima., A. Enomoto and H. Kobayashi

KEK, National Laboratory for High Energy Physics, Tsukuba, 305

H. Shibata and S. Tagawa

Research Center for Nuclear Science and Technology, University of Tokyo,
22-2 Shirakata Shirane, Tokai-mura, Naka-gun, Ibaraki 319-11

Y. Nishida and N. Yugami

Department of Electrical Engineering, Utsunomiya University, Utsunomiya, 321

Abstract

A new plasma wakefield acceleration experiment by using two 10 ps electron pulses from 28 MeV and 18 MeV linacs (the twin linac system) has been planed. One pulse makes the wakefield in the plasma, and the other pulse is used for a testing pulse. By changing the time difference between the two pulses, the timing of testing pulse can be matched to the phase of the wakefield. The estimated accelerating gradient is 200 keV / m. When a pulse train is used for the driving pulse instead of the 10 ps pulse, the maximum gradient of 8 MeV / m will be achieved.

1. Introduction

Plasma wakefield produced by high energy charged particles has been paid attention as a new accelerating mechanism for future high gradient accelerators. Recently, the theoretical and experimental studies on the plasma wake field acceleration have been progressed.

Argonne group did the first experiment on the wakefield acceleration by using a L-band linac.[1] They got an accelerating gradient of a few tens keV / m by using a very unique experimental system which divided one pulse into a driving pulse and a testing pulse. KEK group attained the high accelerating gradient of 12 MeV / m by using a 500 MeV nanosecond pulse which had a several bunches from a S-band linac.[2]

It is important for the high accelerating gradient to attain a high transformer ratio (increment of energy of test pulse / decrement of energy of driving pulse), and a high density plasma. For that purpose, more detailed experiments are necessary.

In this paper, a new plane on plasma acceleration experiment by using two 10 ps electron pulses from 28 MeV and 18 MeV linacs (the twin linac system) at University of Tokyo is reported.

2. Twin Linac System

Both 28 MeV and 18 MeV S-band (2856 MHz) electron linacs (28L & 18L) produce various kinds of pulses from 10 ps to 4.5 μs. Single electron pulse with pulse width of 10 ps is produced by a 1/6 sub harmonic buncher (SHB). Fig 1 shows the schematic diagram of the twin linac system. In the twin linac system,[3] both linac can be operated simultaneously. The timing of the two pulse can be changed by controlling the three phase shifters inserted in the trigger line of the electron gun of 18L, the 467 MHz SHB line of 18L, and the 2856 MHz line of 18L. The time zitter between the twin pulse is less than 10 ps.

In the plasma wakefield acceleration experiment, a 10 ps big pulse (28 MeV, 500 pC) is used for the driving pulse, and a 10 ps small pulse (18 MeV, less than 50 pC) is used for the testing pulse. The timing of the testing pulse can be matched the phase of the wakefield by changing the time difference between the two pulses.

In some cases, a pulse trains (pulse period is 350 ps.) is used for the driving pulse to attain high wakefield. The pulse width of the macro pulse is from 2 ns to 4.5 μs.

3. Experimental Setup

Fig. 2 shows an experimental setup of the plasma section. Two pulse beams from 28L and 18L overlap on a coaxial line in a plasma chamber by an achromatic beam line system which consists of three bending magnets and two Q-magnets. An argon plasma is produced in the chamber (147 mm in inner diameter and 360 mm in length) by a discharge between a LaB_6 cathodes and the chamber in synchronism with the linac pulse. The maximum plasma density is 10^{12} cm^{-3}. The detail of the plasma chamber has been reported elsewhere.[4]

The change of the energy of testing beam is detected by an energy analyzer. It is easy to distinguish the testing beam from the driving beam, because the difference of the energies of two beams is much large.

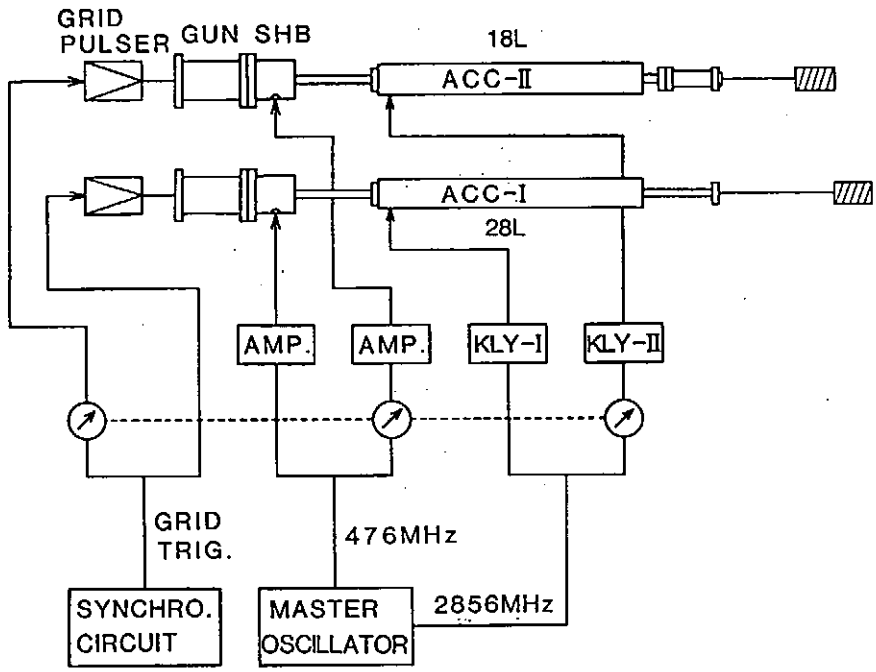

Fig. 1 Schematic diagram of twin linac system at university of Tokyo.

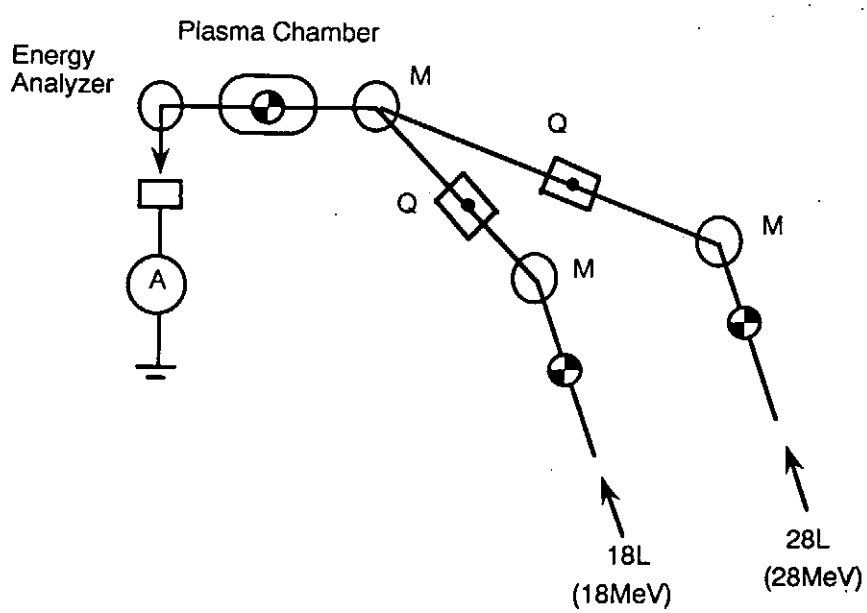

Fig. 2 Experimental setup of plasma section.

4. Estimation of Accelerating Gradient

The wakefield E caused by an impulsive bunch with charge σ is expressed by following equation:

$$\ddot{E} + 2\beta\dot{E} + \omega_p^2 E = E_0\dot{\delta} \qquad [1]$$

where ω_p and β are the plasma frequency and the damping frequency, respectively. By using parabolic approximation, its solution is given by

$$E = 4r_e m_e c^2 N / a^2 \, [2K_2(k_a) + 1 - 4(k_a)^{-2}] \qquad [2]$$

where a and K_2 represent a beam radius and the Bessel function, respectively. By using a 10 ps driving pulse (500 pC), the accelerating gradient is 2 MeV / m at the plasma density of 10^{12} cm^{-3}.

In order to attain higher gradient, a pulse train should be used for the driving pulse. In the condition that ω_p is equal to integral multiple of the bunch frequency, ω_l (2856MHz), the wakefield becomes higher. The ratio of wakefield caused by an infinite pulse train, $W(\infty)$, to that caused by a pulse, E_0, is given by

$$W(\infty) / E_0 = \omega_p / 2\pi\beta \qquad [3]$$

A 50 pC driving pulse gives the gradient of 200 keV / m at the plasma density of 10^{12} cm^{-3}. From the result of the predominant experiment, the ratio was about 40 in the case of a 50 pC driving pulse. Therefore, the achieved gradient by the pulse train will be 8 MeV / m.

References

1. J. B. Rosenzweig, et al., Phys. Rev. Lett., **61**, 90 (1988).
2. K. Nakajima et al., Nucl. Instr. Meth., **A292**, 12 (1990).
3. H. Kobayashi et al., Nucl. Instr. Meth., **B10/11**, 1004 (1985).
4. H. Nakanishi et al., Phys. Rev. Lett., **66**, 1870 (1991).

PARTICLE ACCELERATION BY MICROWAVE WITH SLOW WAVE STRUCTURE

T.WATANABE, K.OGURA[1], K.MINAMI[2] and M.M.ALI[1]

National Institute for Fusion Science, Nagoya, 464-01
[1]Graduate School of Science and Technology, Niigata University, 950-21
[2] Faculty of Engineering, Niigata University, 950-21

Microwave sources based on backward wave oscillators with intense relativistic electron beams are capable of producing high coherent radiation in the cm and mm wavelength regime[1,2,3]. When inner radius of waveguide is corrugated periodically along the axis, the dispersion relation of the microwave in the wave guide become periodic as a function of wave number along the waveguide axis, and backward wave with slow phase velocity come into existence. The resonant interaction between the slow wave and relativistic electron beam sustain the autonomous oscillation of the backward wave oscillator. Reverse process of the backward wave oscillators will be capable of acceleration of slow electron beams to relativistic regime by microwave.

Numerical analysis for particle acceleration by a high power microwave with a finite length slow wave structure has been made by **HIDM2D**, which is a general purpose computer program to solve nonlinear development of boundary value problems described by partial differential equations[4].

We consider a corrugated waveguide in which the inner wall radius varies with the axial coordinate z according to $a(z)$ as shown in Fig.1.

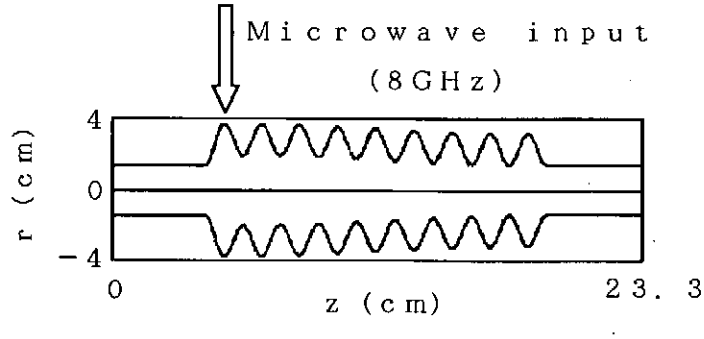

Fig.1 Cross section of slow wave structure for particle acceleration.

Average inner radius of the wave guide is slightly changed so as to coincide the maximum and minimum cutoff frequency of local dispersion relation of the microwave at thick and slender part of the waveguide. High power microwave is introduced from the lefthand side of slow wave structure (thickest

part of the waveguide) with frequency same to the local maximum cut off frequency ($\simeq 8GHz$). Fundamental mode of microwave is assumed to be TM01 mode. Both ends of the waveguide are straight cutoff size waveguide for the applied microwave. A strong external axial magnetic field is applied to the wave guide. Uniform low energy electron beam with density n and velocity $v(<0)$ is assumed to be present initially.

Coupling of microwave and electron beam is expressed by Maxwell's equations and relativistic fluid equations. The set of these nonlinear partial differential equations includes three independent variables (r, z, t). In order to save computer time, we have developed a power expansion method. The final form of the equations to be solved is given by

$$(1) \quad 0 = \frac{\partial n}{\partial t} + \frac{\partial (nv)}{\partial z}$$

$$(2) \quad 0 = \frac{\partial v}{\partial t} + v\frac{\partial v}{\partial z} + \frac{1}{\mathrm{m}\gamma^3}\left(\mathrm{e}E + \frac{T}{n}\frac{\partial n}{\partial z}\right)$$

$$(3) \quad 0 = \frac{\partial^2 E}{\partial t^2} - \mathrm{c}^2\frac{\partial^2 E}{\partial z^2} + \frac{4\mathrm{c}^2}{a(z)^2}(E - S(z,t)) - \frac{2\mathrm{c}^2\, a'(z)}{a(z)}\left(\frac{\partial E}{\partial z} + \frac{\mathrm{e}}{\varepsilon_0}n\right) - \frac{\mathrm{e}}{\varepsilon_0}\left(\frac{\partial (nv)}{\partial t} + \mathrm{c}^2\frac{\partial n}{\partial z}\right)$$

where $\gamma = 1/\sqrt{1 - v^2/\mathrm{c}^2}$, and c, e, m and ε_0 are light velocity, unit charge, electron mass and dielectric constant of vacuum, respectively. $E(t,z)$, $n(t,z)$ and $v(t,z)$ correspond to electric field (in z direction) of microwave, density and velocity of electron beam, respectively. $S(z,t)$ represents the external source of microwave. Periodic boundary condition is assumed. Example of the numerical calculation is shown in Fig.2.

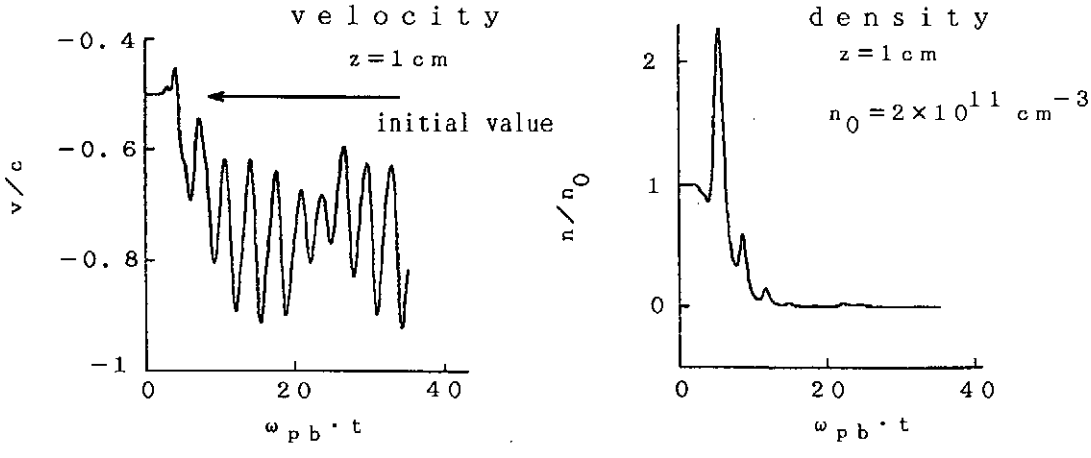

Fig.2 Example of the numerical calculation for the electron beam acceleration by microwave with slow wave structure.

References

[1] Y.Carmel, K.Minami, R.A.Kehs, W.W.Destler, V.L.Grnatstein, D.Abe and W.L.Lou, "Demonstration of Efficiency Enhancement in a High-Power Backward-Wave Oscillator by Plasma Injection", Phys. Rev. Lett. **62**, 2389-2392, (1989).

[2] M.M.ALI, K.OGURA, K.MINAMI, T.WATANABE, W.W.DESTLER and V.L.GRANATSTEIN: "Linear analysis of a finite plasma-filled backward wave oscillator", Phys. Fluids, in printing.

[3] T.WATANABE, K.OGURA, K.MINAMI and M.M.ALI: "Effect of Beam Energy Spread on Radiation Intensity in a High-Power Backward Wave Oscillator with Finite Length", J. Phys. Soc. JPN, in printing.

[4] T.WATANABE: "HIDM, A New Numerical Scheme to Solve Partial Differential Equations": Proceedings of the International Symposium on Supercomputing, (Kyushu University Press, (1991)), 229-235.

Electron Acceleration by v_pxB Mechanism in Vacuum

Noboru Yugami and Yasushi Nishida

Department of Electrical and Electronic Engineering,

Utsunomiya University

Recent interests of charged particle accelerators are focused on generating a much higher acceleration gradient. In the last decade some of new acceleration schemes using a longitudinal electric field of the wave, including a plasma wake field accelerator (PWFA), a plasma beat wave accelerator (PBWA) and a v_pxB scheme (or a surfatron), have been proposed.[1-8] Some of the experimental results based on the above mentioned scheme have been reported to give the higher acceleration gradient. The new schemes using plasmas can be expected to generate much higher electric field, but it is also easy to predict some difficulties of controlling plasma parameters. The v_pxB acceleration phenomena have been observed in the experiments of microwave-plasma interaction.[9,10] In this scheme a static magnetic field is applied vertically to the wave propagating direction and the particles are accelerated along the wave front at constant phase with respect to the wave, and the acceleration continues until the trapping condition breaks.

In the v_pxB system a charged particle is trapped in an electromagnetic wave (TM wave) with a phase velocity v_p propagating in the z direction immersed in a static magnetic field B_0 in the x direction (Fig. 1).

The analysis of the interaction between a wave and a particle can be described using the equation of motion of the particle. The electromagnetic wave propagating in the z direction has a longitudinal component of the electric field written by

$$E_z(z,t) = E_m \sin(kz-\omega t)\hat{z}, \qquad (1)$$

where k and ω are the wave number and an angular frequency of the wave,

respectively. The phase velocity of the wave is defined as $v_p = \omega/k$.

The equation of motion of the charged particle is expressed as

$$\frac{d(mv)}{dt} = qE_z + qvxB_o. \quad (2)$$

In the configuration shown in Fig. 1, this equation is rewritten as follows:

$$m_o \frac{d(\gamma v_y)}{dt} = qB_o v_z, \quad (3)$$

$$m_o \frac{d(\gamma v_z)}{dt} = qE_z - qB_o v_y. \quad (4)$$

One can obtain next equation from the energy conservation law,

$$m_o c^2 \frac{d\gamma}{dt} = qv_z E_z, \quad (5)$$

where m_o and γ are the rest mass of the particle and the relativistic factor of the particle, respectively. One can easily obtain the criteria for trapping condition, $E_m > \gamma_p B_O v_y$ from Eq.(4).

In the non-relativistic case, $\gamma_p \approx 1$, for the particle is trapped in the wave ($v_z = v_p$), $v_y = (c^2 - v_z^2)^{1/2}$ holds, and the trapping condition becomes as:

$$E_m > \gamma_p(c^2 - v_z^2)^{1/2}B_o \approx \gamma_p(c^2-v_p^2)^{1/2}B_o = cB_o \quad (6)$$

$$v_E = E_m/B_o > c.$$

This formula represents the trapping condition for the nonrelativistic case and is referred later to explain the experimental results.

Figure 2 is a schematic diagram showing an electron beam gun, a slow wave structure and an energy analyzer. The injected electron is initially accelerated by a high voltage power supply, with maximum energy and current of 100 keV and 1 mA, respectively. A hair-pin type cathode is made of a tungsten filament which is originally made for an electron microscope. The accelerated electrons through the accelerator are detected by an electron energy analyzer which consists of a pair of permanent magnets yeilding a uniform magnetic field of 200 G.

The pulsed electromagnetic wave is generated by a magnetron which is

triggered by the external timer with a typical pulse width of 5 μs in repetition at 10 Hz. The power sources has a maximum power of 10 kW, the emitted frequency was measured by comparing with the standard oscillator to give 2.459 GHz.

The static, vertical magnetic field for a v_pxB acceleration is generated by a pair of saddle shaped external coils with the uniform length 32 cm (less than 3 % uniformity; 40 cm for 5 %) in the z direction and 5 cm (less than 3 %) in the y direction. A maximum field strength of 10 G is measured at the center of the accelerator. This value should be strong enough to demonstrate the v_pxB principle in the experimental parameters.

A schematic view of the slow wave structure of the TM mode is shown in Fig. 3, and its dimensions are listed in Table 1. This structure consists of parallel fin electrodes with 48 cm long in the wave propagation direction. Its propagation mode of the microwave is designed to be $2\pi/3$ mode and the phase velocity is 0.464c (corresponding energy of 66 keV) at the RF frequency of 2.45 GHz. The cross section of the structure is rectangular.

An example of experimental results is shown in Fig. 4. The horizontal and vertical axes indicate the incident electron energy E_o and the energy increment $\Delta\varepsilon$, respectively. Symbols, ○, △ and □ stand, respectively, for the value of the external magnetic field of 0, 2 and 3 Gauss. When B_o = 0 G, the accelerator operates as the conventional linac. Therefore one can easily compare the v_pxB accelerator with the conventional one in a same machine. The slow wave structure strongly resonates with the microwave around E_o = 52 and 66 keV. Data show that the energy increment of the v_pxB scheme is larger than that of the conventional one at every incident electron energy. When the incident beam energy is 66 keV, for example, the observed electron energy is 79.0 keV ($\Delta\varepsilon$ = 13.0 keV) with a static magnetic field of 3 G, while

in the conventional accelerator the energy reaches 76.0 keV corresponding $\Delta\varepsilon$ = 3.0 keV.

Figure 5 shows the energy increment as a function of the static magnetic field intensity. Up to 2.6 G, the energy increment $\Delta\varepsilon$ is proportional to B^2, i.e., $\Delta\varepsilon - \Delta\varepsilon(B_o = 0\ G)$ B^2, while over 2.6 G, $\Delta\varepsilon$ decreases sharply. This dependence can easily be explained by the Lorentz force acceleration in the y direction. After the value of B_o exceeds 2.6 G, the electron cannot be trapped by the wave potential anymore. These results mean that the trapping condition is no longer maintained. The underlying physics producing a critical magnetic field B_c = 2.6 G is explained in the following section.

As seen in Eq.(6), the trapping condition is $v_E = E_m/B_o > c$, i.e., the electrons are continuously accelerated until the trapping condition breaks down. The experimental parameters are listed in Table 2. The electric field E_m was obtained from the relation between the energy increment of the conventional linac mode and the length of the accelerator cavity. B_{exp} indicates the magnetic field under which the maximum acceleration energy is attained. Here v_E is normalized by the speed of light c. At every incident energy, v_E is smaller than c, that is, the trapping condition was not satisfied in the experiments. However, above results cannot give the information of the time when electrons detrap from the wave potential. The detrapping time t_c can be determined by the equation,[11]

$$\omega t_c = \frac{(1-\delta^2)^{0.5}}{\delta} - \cos^{-1}\delta + kz(0) - \frac{kv_x(0)}{\omega_c} \qquad (7)$$

where $\delta = \omega_c^2/\omega_b^2 << 1$, $\omega_c = qB_o/m$ and $\omega_b^2 = qE_zk/m$.

To explain the experimental data, assuming z = 0, v_x = 0 at t = 0, one can obtain

$$\omega t_c = \frac{(1-\delta^2)^{0.5}}{\delta} - \cos^{-1}\delta$$

and using $\delta << 1$, Eq.(7) is rewritten as

$$\omega t_c = 1/\delta . \qquad (8)$$

The time τ is a time duration of the electron travelling with a constant velocity corresponding to the incident energy. The differences τ and t_c vary from 1.1 to 2.2 nsec. Although the experimental data and the calculated results are slightly different, it is shown that these are in fairly good agreement after taking into account of the following conditions; The incident electron is injected obliquely to the z axis, so that the value of τ is greater than that of the tabulated. When the present machine is used as a conventional linear accelerator without a static magnetic field, the electron beam is adjusted to traverse the region with maximum field strength in the slow wave structure. In other words, the maximum particle energy could be reached in the conventional mode. In the case of v_pxB accelerator, however, the orbit of the electron beam bends slightly, because of the slow beam velocity, and the electron cannot travel in the area with the maximum field strength. Therefore the existence of the critical magnetic field (2.6 G at 62 and 66 keV) can be interpreted by the present theory.

In the present state, unfortunately we cannot perform the precise computer simulation by employing the real experimental parameters with using the realistic machine structure. If we could do those simulations much clear interpretations are expected and these are our future tasks.

A new electron linear accelerator based on the v_pxB acceleration scheme has been demonstrated to work successfully in a vacuum system. The experimental results show that proposed scheme accelerates the electron more effectively than the conventional linear accelerator. The measured data are in good agreement with the theoretical results containing weak relativistic effects.

References

1) T. Tajima and J. M. Dawson, Phys. Rev. Lett. 43, 267–270 (1979).

2) P.Chen, J. M. Dawson R. W. Huff and T. Katsouleas, Phys. Rev. Lett. 54, 693–696 (1985).

3) R. Sugihara and Y. Mizuno, J. Phys. Soc. Jpn. 47, 1290–1295 (1979).

4) Y. Nishida, M. Yoshizumi and R. Sugihara, in Proceedings of the Thirteenth Annual Anomalous Absorption Conference, Banff, Alberta, Canada, 5–10 June 1983, (unpublished) p.F7; Phys. Lett. 105A, 300–302 (1984); Y. Nishida, M. Yosizumi and R. Sugihara, Phys. Fulids 28, 1574–1576 (1985).

5) C. Joshi and T. Katsouleas, in Laser Acceleration of Particles, edited by C. Joshi and T. Katsouleas, AIP Conf. Proc. No. 130 (AIP, New York,1985).

6) T. Katsouleas and J. M. Dawson Phys. Rev. Lett. 51, 392–395 (1983).

7) Y. Nishida, N. Yugami, H. Onihashi, T. Taura and K. Otsuka, Phys. Rev. Lett. 66, 1854–1857 (1991), and references therein.

8) A.Loeb and L. Friedland, Phys. Rev. A 33, 1828–1835 (1986).

9) Y. Nishida, in Laser Interaction and Related Plasma Phenomena, edited by H. Hora and G. Miley (Plenum, New York, 1986), Vol. 7, pp. 811–825.

10)Y. Nishida, in Proceedings of the Nineteenth International Conference on Phenomena in Ionized Gases, Invited Papers, (July 10–14 1989, Belgrades, Yugoslavia) edited by Vida J. Zigman, pp. 186–194; A Variety of Plasma, Proceedings of the 1989 International Conference on Plasma Physics, edited by A. Sen and P. K. Kaw. Indian Academy of Sciences, pp. 39–55.

11)Y. Terashima, J. Phys. Soc. of Jap. 30, 2210–2217, (1991)

Table 1.
Dimensions of slow wave structure
d: interval between fins; t: fin thickness; *l*: fin depth; h: height; a: width

E_o (keV)	v_p	d(mm)	t(mm)	*l*(mm)	h(mm)	a(mm)
66.0	0.454c	19.0	2.0	25.8	104	110

Table 2.
Experimental parameters of the electron trapping.

E_o(keV)	E_m(kV/m)	B_{exp} (G)	v_E(xc)	t_c(ns)	τ (ns)	P(kW)
62	16.6	2.6	0.21	4.7	3.5	10
66	20.0	2.6	0.26	5.6	3.5	10

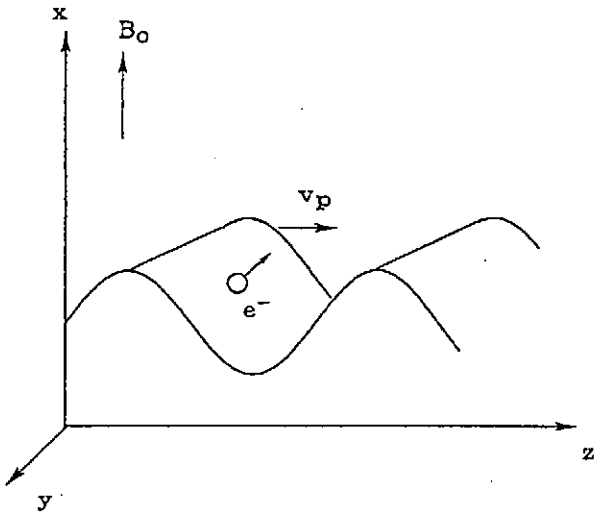

Figure 1

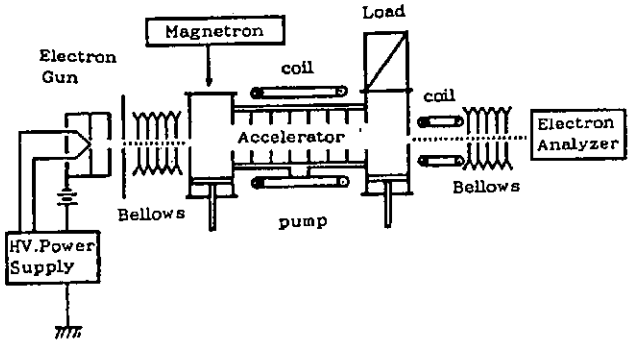

Figure 2

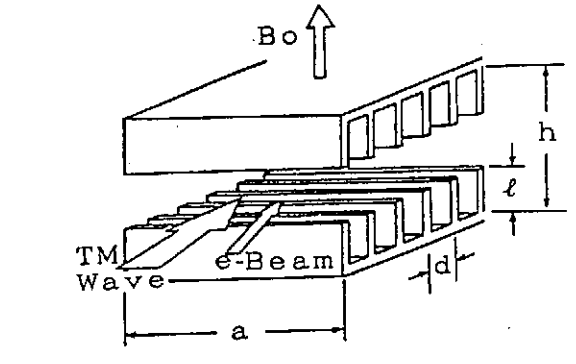

Figure 3

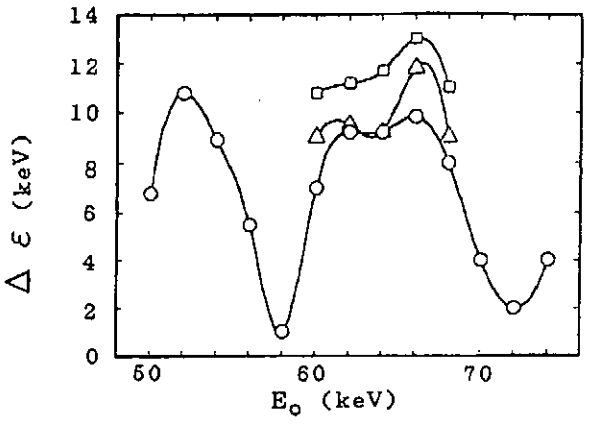

Figure 4

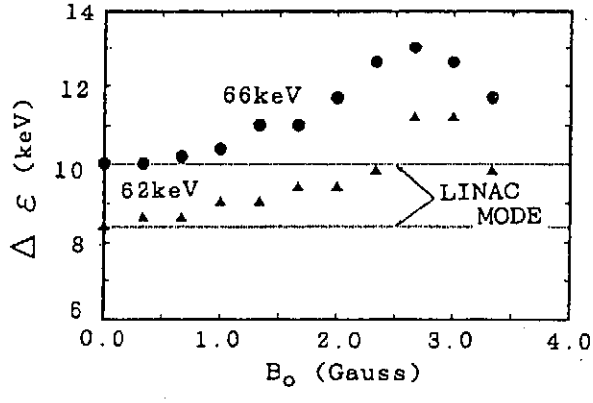

Figure 5

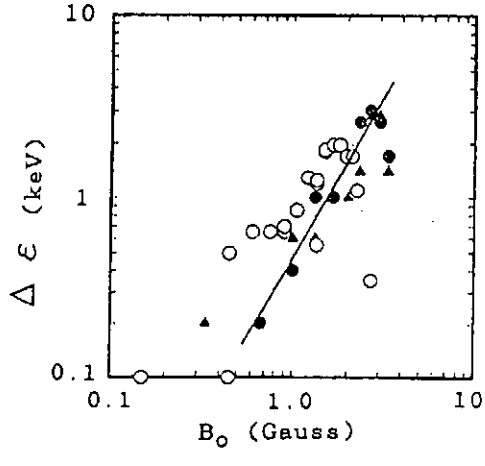

Figure 6

Multi-Laser-Beam Accelerator

Ryo SUGIHARA

Plasma Science Center, Nagoya University, Nagoya 464-01

A system of phased multi-laser beams can construct an effective slow wave which traps and accelerates electrons if an external magnetic field is applied so as to obey the $V_p \times B$ acceleration principle. The shape of an individual laser beam is chosen to be Gaussian in one dimension, and the wave field is assumed to be linearly polarized. The beam divergence accompanied by the Gaussian beam is also taken into account. A necessary condition for the electron trapping is obtained. Acceleration of the electron satisfying the condition is continuous and subsequently, arbitrarily large energy is theoretically possible.

KEYWORDS: $V_p \times B$ acceleration, particle trapping, new accelerator, Gaussian laser beams, polarized laser beams

§1. Introduction

Particle acceleration by the use of the intense field of a laser beam is an interesting and important topic in view of a high-energy particle accelerator. Use of a plasma wave excited by a laser beat wave may be one of the plausible methods, and a number of studies have been conducted[1,2]. Numerous difficulties against the realization of the beat wave accelerator are, however, expected to emerge mainly from plasma nonlinearities which are very hard to control[3].

Direct coupling between a single laser beam and the particles has been given little consideration because the gain by the particles is limited to the energy of the quiver motion due to the field of the laser. Only Kawata et al.[4] and Cicchitelli et al.[5] proposed ideas for the direct use of the laser field for energizing particles. The acceleration, however, takes place only during one

cycle in the former and a half-cycle in the latter out of the intense laser pulse and then is limited. By contrast, Takeuchi et al.[6,7] have found that even a transverse electromagnetic (EM) wave can trap and continuously accelerate the charged particles due to the principle of $V_p \times B$ acceleration[6-10], provided that the wave phase velocity is slower than the light velocity c. This is a big motivation to the present proposal. We will show here that, without any slow wave structure, phased laser beams (propagating at light velocity) can trap and accelerate the charged particles continuously if relevant parameters satisfy the $V_p \times B$ acceleration condition.

§2. Configuration

Imagine a system made up of a large number of Gaussian laser beams which run parallel to each other and are arranged two-dimensionally. Such a system is depicted in Fig.1; the coordinates are also given therein. Here λ is the wavelength, a is the radius of an individual laser beam and d is the distance between neighboring laser beams. An essential assumption is that the EM wave be linearly polarized. That is, the wave electric and magnetic fields are supposed to be given by $\mathbf{E}(\mathbf{r}',t) = \mathbf{e}_{y'}E(\mathbf{r}',t)$ and by $\mathbf{H}(\mathbf{r}',t) = -\mathbf{e}_{x'}E(\mathbf{r}',t)$ where $\mathbf{e}_{x'}$ and $\mathbf{e}_{y'}$ are the unit vectors in the x'- and y'-directions. In reality, $\mathbf{E}$ has a small E_z component and also $\mathbf{H}$ has small H_y and H_z components so as to satisfy Maxwell's equations. They are, however, negligibly small if $ka >> 1$, which is the case in this paper. Plausibility of this assumption will be discussed in §4 in more detail. We assume that the phases of the electric field between the nearest two beams differ by an amount of $\Delta\lambda$ and we introduce an angle θ_0 by $\tan\theta_0 = \Delta\lambda/d$. An important point is that a static magnetic field $\mathbf{B}_0$ is applied along the x'-axis. We also assume $| z' | << z_r$ (the Rayleigh range), then the electric field may be given by $E(\mathbf{r}',t) \propto \sin\psi' \exp[-\{x'^2 + y'^2\}/a^2]$ and $\psi' = kz' - kct + \alpha, \alpha$ the phase angle. Therefore the electric field of the

phased multi-laser beams may be given by

$$E(\mathbf{r}', t) = -\bar{E} \sum_{n=-\infty}^{\infty} \sin\phi'_n \exp[-\{x'^2 + (y' - nd)^2\}/a^2], \tag{1}$$

where $\bar{E} = E_0(d/a\sqrt{\pi})$ and $\phi'_n = kz' + knd\tan\theta_0 - kct$. The intensity of a beamlet is taken so that the average magnitude over the y'-direction of peak electric field in the phased laser beams becomes E_0 irrespective of beam overlapping. We assume that the radius a is large enough compared with the transverse dimension of an electron (or positron) beam, and that the charges traverse the vicinity of the center of each laser beam. This may allow $x' = 0$ in eq.(1). Then we replace the cylindrical laser beams with one-dimensional (slab) Gaussian beams, and a is now the half-width of an individual laser (sheet) beam.

§3. Wave-Particle Interaction

Now we obliquely inject a test particle with a charge q and investigate the interaction. The wave field is inhomogeneous and then the equation of motion would not be tractable. We study a limiting case which allows an analytic treatment. Keeping $\Delta\lambda/d = \tan\theta_0$ constant, we take the limits of $d \to 0$ and $\Delta\lambda \to 0$. We note that the summation over n now reduces to an integral over d and have

$$E(\mathbf{r}', t) = -\mathbf{e}_{y'} E_m \sin\phi', \tag{2}$$

$$E_m = E_0 \exp[-(ka\tan\theta_0/2)^2], \tag{3}$$

where $\phi' = kz' - kct + ky'\tan\theta_0$. The resultant *wave* is formed by a superposition of an infinite number of waves. Its k is not normal to the *wave* front and consequently, the *wave* does not satisfy $\nabla \cdot \mathbf{E} = 0$. This limit, however, gives valuable information when realistic cases are investigated. Then, for a while, we use this *wave* and call this system the continuous laser beam system (CLBS).

Now we construct the equation of motion for the test particle. For the convenience of calculation, the coordinates are turned around the x'-axis by θ_0 and then we have

$$md(\gamma \mathbf{v})/dt = q\mathbf{E} + (q/c)\mathbf{v} \times \mathbf{e}_x(B_0 + H), \tag{4}$$

where $E_y = -E_m \cos\theta_0 \sin\phi$, $E_z = -E_m \sin\theta_0 \sin\phi$, $H = E_m \sin\phi$ and γ is the Lorentz factor. It is noted that the phase ϕ is now written as

$$\phi = (k/\cos\theta_0)(z - ct\cos\theta_0). \tag{5}$$

Therefore the phase velocity V_p along the z-axis is $V_p = c\cos\theta_0 < c$. Thus we have an effective *slow* EM wave. Let us think of the motion of the particle in the wave frame which runs with the velocity of $V_p = c\cos\theta_0$ in the laboratory frame. The v_x is safely put to zero and we investigate the motion in two-dimensional space. With the Lorentz transformation, the equation of motion in the new frame is now

$$md(\Gamma V_y)/dT = (q/c)(\gamma_p V_p B_0 + V_z B_t), \tag{6}$$

$$md(\Gamma V_z)/dT = qE_z - q(V_y/c)B_t, \tag{7}$$

$$mc^2 d(\Gamma)/dT = qV_z E_z + q(V_y/c)\gamma_p V_p B_0, \tag{8}$$

where $B_t = \gamma_p B_0 + H/\gamma_p$, $\gamma_p = (1 - V_p^2/c^2)^{-1/2} = 1/\sin\theta_0$, $\Gamma = (1 - V_y^2/c^2 - V_z^2/c^2)^{-1/2}$ and each capital letter corresponds to the counterpart of the lower-case letter in the laboratory frame and the phase ϕ should be replaced with $\Phi = kZ/(\gamma_p \cos\theta_0)$.

First we discuss the trapping of the particle. Using the same set of eqs.(6),(7) and (8), Takeuchi[10] showed the occurrence of particle trapping by an elliptically polarized EM wave that has E_y and E_z in our terminology. Although his E_y and E_z are slightly different in phase from ours, his calculation suggests that the trapping is possible for our *wave*, too.

Suppose that the particle is continuously accelerated along the Y-axis following the $V_p \times B$ acceleration principle. This implies that the particle is only confined (or trapped) in a definite region in the Z-direction. Subsequently, eq.(7) will provide the condition of particle trapping. We now denote the right hand side of (7) by F_z. Using $E_z = -E_m \sin\theta_0 \sin\Phi$ and the definition of B_t, we have

$$F_z = -qE_m \sin\theta_0 \sin\Phi(1 + V_y/c) - q(V_y/c)B_0/\sin\theta_0. \tag{9}$$

The first term on the right hand side of eq.(9) includes two kinds of forces. One, $-qE_m \sin\theta_0 \sin\Phi$, is a longitudinal force induced by the projection of $\mathbf{E}(\mathbf{r}', t)$ on the Z-axis and the other, $-qE_m \sin\theta_0 \sin\Phi \cdot (V_y/c)$, is the force that traps the particle in a moving magnetically neutral sheet, as is discussed in ref.4. Suppose that the test particle with a high initial energy ($\gamma_0 >> 1$) is trapped by the wave and that the motion of the particle reaches a quasi-stationary state with $V_y \doteq c$ and $V_z \doteq 0$. Then the left hand side of (7) is zero and subsequently, F_z should be zero. Thus we have

$$2E_m \sin\theta_0 \sin\Phi_c = B_0/\sin\theta_0,$$

where $\Phi_0 = kZ_0/\gamma_p \cos\theta_0$ indicates the locked phase[8,9]. Hence we have a condition for trapping,

$$B_0 < B_c(\theta_0) \equiv 2E_m \sin^2\theta_0. \tag{10}$$

This is a necessary condition for the particle to be trapped and accelerated quasi-stationarily in our model field (2).

In Fig.2 the region of $\phi_0 \equiv \phi(0)$ of particles which are eventually trapped is shown as a function of B_0 for $E_0 = 1.0, \theta_0 = 0.05\pi$, $v_{y0} = 0$ and $v_{z0} = V_p = c\cos\theta_0$. No trapped particles are found to exist for $B_0 > B_c(\theta_0)$. This tendency has been confirmed for various sets of E_0 and θ_0, and we believe that the result verifies the necessary condition of trapping for CLBS.

The energy of the particle monotonically increases in time, oscillating around a linear curve, asymptotically approaches the curve, and the state becomes quasi-stationary, as was assumed above[6-10]. This behavior is common to $V_p \times B$ acceleration, and we consider here this eventual quasi-stationary state. We have $V_{z0} \doteq 0$ as well as $V_y \doteq c$, and eq.(8) then yields $mc^2 d\Gamma/dT \doteq q\gamma_p V_p B_0$. Using the relation $d\Gamma/dT = d\gamma/dt$, we obtain

$$mc^2 d\gamma/dt \doteq q\gamma_p V_p B_0. \tag{11}$$

Expression (11) is again an expression common to $V_p \times B$ acceleration. In this case, by (11), $mc^2\gamma$ approaches $mc^2\gamma = q\gamma_p B_0 V_p t$ and, using $\gamma^{-2} \doteq 1 - (v_y/c)^2 - (V_p/c)^2 = \gamma_p^{-2} - (v_y/c)^2 \to 0$, we approximately have $v_y = c/\gamma_p$. That is, the tightly trapped charge is accelerated linearly in time, and its velocity converges to a point $(v_y, v_z) = (c/\gamma_p, V_p)$ on the light circle.

So far, discussions have been for the limiting case of $d = 0$. Now considerations are extended to the case of $d \neq 0$ by using expression (1) with $x' = 0$. In Fig.3 we show a trapping region in $a - d$ parameter space for $E_0 = 1.0$, $B_0 = 0.1E_0 \sin^2\theta_0$ and $\theta_0 = 0.02\pi$. For $d = 0$, we use condition (10) with (3). This gives

$$ka_c\theta_0 = 2[\ln(2E_0 \sin^2\theta_0/B_0)]^{1/2}, \tag{10}$$

a_c denoting a critical a over which no trapping occurs. When $d \neq 0$, we actually solve the equation of motion. It is found that the a_c is very close to the upper limit of a for rather wide d, e. g. , $d < 3a_c$. This implies that E in eq.(2) can be used for the same range of d. It is also numerically understood that eq.(11) gives quite an exact approximation for energy gain.

§4. Discussion

We argue about the limiting form of E in eq.(2). The E in eq.(1) with finite d but $d << a$ will satisfy Maxwell's equations. For a relativistic electron, the difference between fields with $d << a$ and $d = 0$ might make no sense; then,

in the numerical evaluation of trapping regions, the upper limit of a for $d \to 0$ and that for small $d \neq 0$ should be smoothly connected. Thus the results obtained by using E and H in the limit of $d = 0$ is meaningful.

The Gaussian beam accompanies the beam divergence. The injected particle is accelerated, its γ soon becomes $\gamma >> 1$ and converges to $(v_y, v_z) = (c/\gamma_p, V_p) = (c\sin\theta_0, c\cos\theta_0)$ or, in the original frame, $(v'_y, v'_z) = (c\sin 2\theta_0, c\cos 2\theta_0)$. The particle does not escape from or cannot traverse the beam unless $2\theta_0 > \theta_d$ where θ_d is the divergence angle and is given by w_0/z_r with w_0 the waist of a laser beam and $z_r \equiv \pi w_0^2/\lambda$ the Rayleigh range. The w_0 may be replaced with a and hence, θ_d of this beam will be given by $\theta_d = 2/ka$. Thus the particle will traverse the beam without suffering from beam divergence if $2\theta_0 >> 2/ka$ or $ka\theta_0 >> 1$. In Fig.3 the line $ka = 1/\theta_0$ is given by a dotted line. It is evident that the relation $ka\theta_0 >> 1$ is equivalent to $z_r >> \mid z' \mid$ where $\mid z' \mid$ is the projection of the particle orbit on the axis of a beamlet during the passage of the particle through the beamlet. In the figure we have $ka_c\theta_0 \approx 3$, which may be critical in view of satisfying the condition. As $ka\theta_0$ increases, E_m, the effective electric field, decreases exponentially, which is a drawback to this acceleration scheme. We may, however, not worry about the beam divergence if the divergenceless beam, the Bessel beam, can be used. In this case, z_r may not have meaning and $ka\theta_0$ could be less than unity unless $ka < 1$. Experiments[11,12] verify the existence of beams closely related to the Bessel beam. Theoretically a Bessel-Gaussian beam is a plausible and approximate solution to Maxwell's equations[13].

Whether a plane-polarized Gaussian beam exists is a most important question. Theoretical predictions[14,15]*1 are available for it though no experimental evidence has ever been obtained. Meanwhile, for $a >> \lambda$, we were able to produce a beam which was approximated by a linearly polarized plane wave

[1]* K.Shimoda: private communication; he showed the existence of such a solution clearly and elementally.

except for its very edges.

The number of beams needed is also a crucial issue to be discussed. We use the CLBS approximation. Suppose the acceleration lengths are y_a and z_a for obtaining an energy W, and then we have $z_a = W/(q\gamma_p B_0)$ from eq.(11) and

$$y_a = z_a \sin 2\theta_0 = 2W \sin^2\theta_0 \cos\theta_0 / qB_0. \tag{13}$$

Therefore the number of beams needed will be $y_a/d = 2W \sin^2\theta_0 \cos\theta_0/qdB_0$.

An example is given for accelerating electrons to 1 TeV. Suppose $\theta_0 = 0.02\pi$, $ka\theta_0 = 3.0$ and $E_0 = 2\times 10^9$ V/cm. We choose $B_0 = 0.1E_0 \sin^2\theta_0$ which yields $B_0 = 0.95\ E_m \sin^2\theta_0$. The expression $z_a = W/(q\gamma_p B_0)$ implies that an 800-m device provides 1 TeV electrons. Suppose $d = 2a$; eq.(13) indicates that we need $y_a/d = (kz_a/6)\theta_0 \sin 2\theta_0 = 660(\text{cm})/\lambda(\text{cm})$ laser beams and that, if $\lambda = 10^{-3}$ cm (CO_2 laser), y_a/d is 6.6×10^5. If a free electron laser with λ = 0.1 cm and E_0 = 2 GV/cm is available, the y_a/d will be 6.6×10^3. Since a single beam of this intensity is presently available, it may be technologically feasible to produce 6,600 - 660,000 laser beams, not now but probably in the future. The principle of acceleration presented in the paper is rather common and can be applied not only to laser beams but also to electromagnetic waves with longer wavelengths, and thus applications in the future cannot be passed over. Moreover, if we apply the principle to the case of obtaining GeV-order electrons, not TeV-order ones, the number of laser beams needed will be lessened by an order of 1/1000, and the resultant number will be more acceptable and the fields of application will be wide.

Radiation loss is one of the main concerns. The scheme under consideration belongs to $V_p \times B$ acceleration and therefore the loss must be similar to that estimated for the Surfatron[16,17]; the result seems to guarantee a negligible radiation loss.

In summary, we presented a new scheme of particle acceleration which

uses a system of phased multi-laser beams. The mechanism of trapping and acceleration belongs, in principle, to $V_p \times B$ acceleration, and the acceleration is unlimited. We demonstrated that if the system is composed of a sufficient number of laser beams, each of which has a 2×10^9 V/cm electric field, we may have 1 TeV electrons in an 800-m-long device with an external magnetic field of less than 3 kG.

The author acknowledges Dr.S.Takeuchi of Yamanashi University for his invaluable discussions and also thanks Prof.Y.Nishida of Utsunomiya University for his interest in this work and for comments. He is indebted to Prof.K.Shimoda of Keio University for his enlightening discussions and indications on the properties of laser beams.

References

1) T.Tajima and J.M.Dawson: Phys.Rev.Lett. **43** (1979) 267.

2) C.Joshi, T.Katsuoleas, C.E.Clayton, W.B.Mori, J.M.Kindel and D.W.Forslund: AIP Conf.Proc.No.156 *Advanced Accelerator Concepts*, Madison, ed. F.E.Mills (Am.Inst.Phys., New York, 1986) p.71.

3) R.Bingham, W.B.Mori and J.M.Dawson: AIP Conf.Proc.No.130 *Laser Acceleration of Particles*, Malibu, eds. C.Joshi and T.Katsuoleas (Am. Inst.Phys., New York, 1985) p.138.

4) S.Kawata, A.Manabe and S.Takeuchi: Jpn.J.Appl.Phys. **28** (1989) L704.

5) L.Cicchitelli, H.Hora and R.Postle: Phys.Rev.A **41** (1990) 3727.

6) S.Takeuchi, K.Sakai, M.Matsumoto and R.Sugihara: Phys.Lett. **122** (1987) 257.

7) S.Takeuchi, K.Sakai, M.Matsumoto and R.Sugihara: IEEE Trans.Plasma Sci. **SP-15** (1987) 251.

8) R.Sugihara and Y.Midzuno: J.Phys.Soc.Jpn **47** (1979) 1290.

9) Y.Nishida, M.Yoshizumi and R.Sugihara: Phys.Lett. **105A** (1984) 300.

10) S.Takeuchi: J.Phys.Soc.Jpn. **58** (1989) 1604.

11) J.Durnin, J.J.Miceli,Jr. and J.H.Eberly: Phys.Rev.Lett. **58** (1987) 1499.

12) K.Uehara and H.Kikuchi: Appl.Phys. **B48** (1989) 125.

13) F.Gori, G.Guattari and C.Padovani: Opt.Commun. **64** (1987) 491.

14) M.Lax, W.H.Louisell and W.B.McKnight: Phys.Rev. **A11** (1975) 1365.

15) D.N.Pattanayak and G.P.Agrawal: Phys.Rev. **A22** (1980) 1159.

16) T.Katsouleas and J.M.Dawson: Phys.Rev.Lett. **51** (1983) 392.

17) D.V.Neuffer: Phys.Rev.Lett. **53** (1984) 1026.

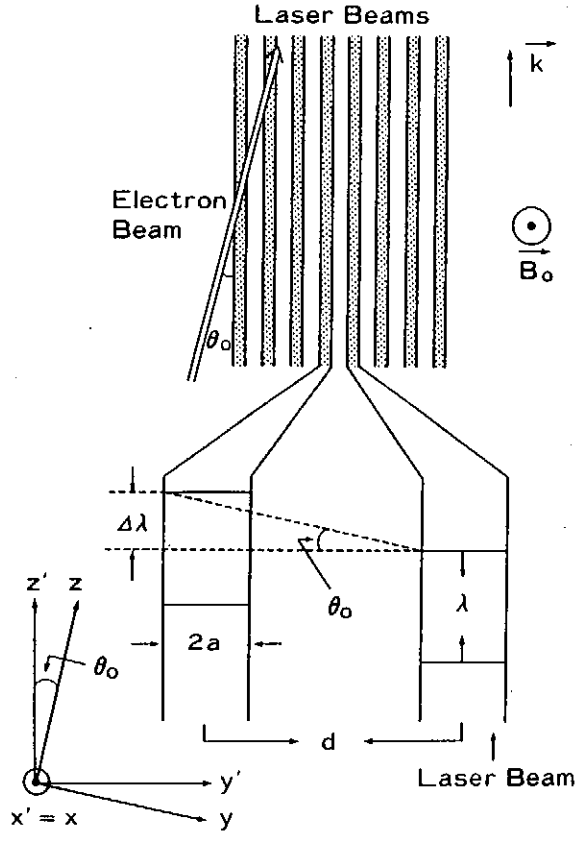

Fig.1. Schematic of the system of phased multi-laser beams. An individual beam is modeled with a slab with a Gaussian intensity distribution of electric field. λ is the wavelength and $\Delta\lambda$ is the phase difference between neighboring laser beams.

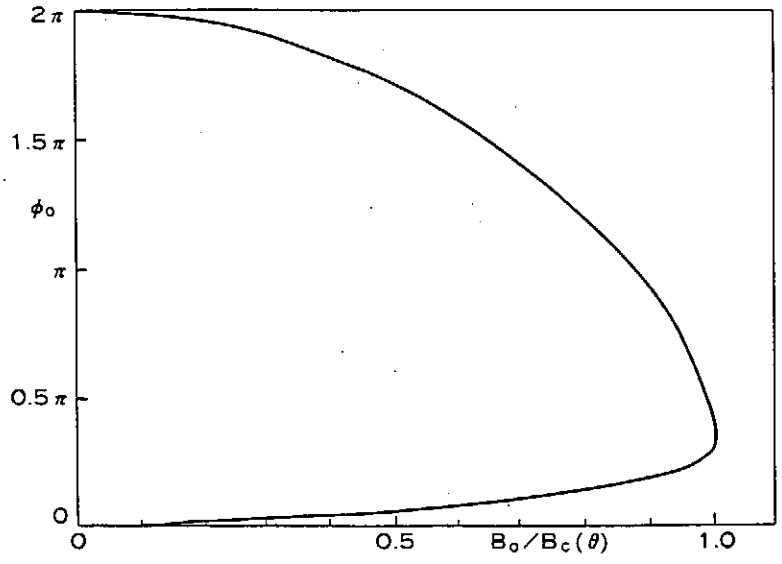

Fig.2. The trapping region in the limit of $d = 0$ in the $\phi_0 - B_0$ space. $\theta_0 = 0.05\pi$, $v_{y0} = 0$ and $v_{z0} = V_p = c\cos\theta_0$. A particle having initial values inside the curve is eventually trapped.

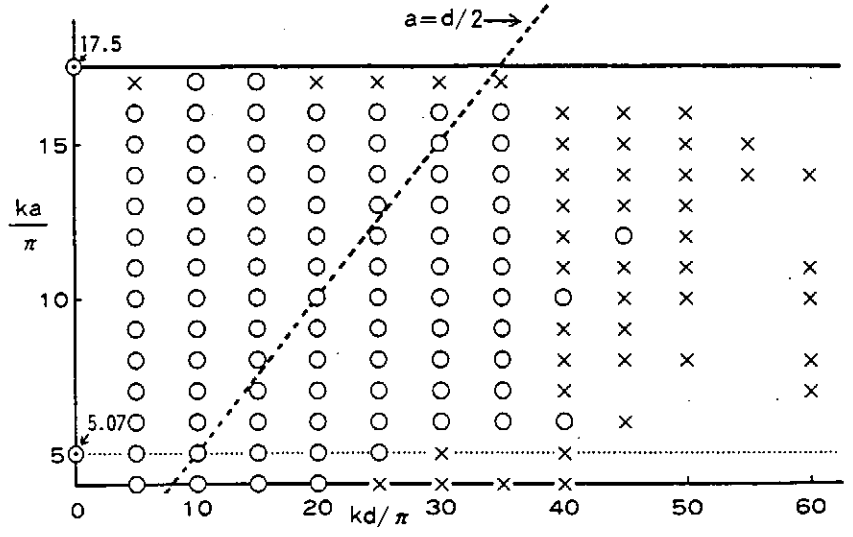

Fig.3. The trapping region for $d \neq 0$ in the $a - d$ parameter space for $\theta_0 = 0.02\pi$, $v_{y0} = 0$ and $v_{z0} = V_p$. We divide one period in $z_0' \equiv z'(0)$ in a beamlet into 40 cells and trace the orbit of a particle in each cell. In the cases of sets of a and d marked by $\times$, 1 to 10 particles out of 40 are eventually trapped, while for sets of a and d marked by $\bigcirc$, more than 11 particles are trapped. The solid and the dotted lines denote $ka_c(= 17.5\pi)$ and $ka = 1/\theta_0(= 5.07\pi)$ for the present parameters.

Electron Linear Accelerator using Phased Multi-Electromagnetic-Wave Beams

Kazue Otsuka, Noboru Yugami, and Yasushi Nishida
Department of Electrical and Electronic Engineering
Ustunomiya University,
Ustunomiya, Tochigi 321, Japan

Abstract

The motion of charged particles in a multi-electromagnetic wave-beam system (Multi-EM Beam) has precisely been investigated numerically. This system consists of a lot of plane electromagnetic-wave beams propagating in parallel each other, but each beam is successively delayed of its phase from the one to the other, making an apparent wave propagating obliquely to the original EM beams. In this system an electron beam is injected along the apparent wave propagation direction. When the static magnetic field is applied in parallel with the fluctuating magnetic field of the waves, it is observed that the charged particles are trapped in the apparent-wave trough and accelerated stably into high energy. For realizing the present scheme, a simple new system which consists of many mirrors but uses one EM beam is proposed.

1. Introduction

Recently much interest has arisen in plasma based high energy particle accelerator schemes.[1] The VpxB accelerator[2-4] is one of the promising scheme, and received much attention, where V_p is the phase velocity of the electron plasma wave. This scheme, however, needs high field, large amplitude plasma wave to be excited. For this purpose, the plasma wake-field[5-7] can be employed. It is also clear that the plasma wake-field can be used as the plasma based particle accelerator as its original ideas. The V_pxB electron linear accelerator[8,9] is another trend, which uses no plasma, but depends on the same scheme originally found in the plasma.[4] In this scheme, the slow-wave structure is employed for making a driver wave of the TM mode. The final energy of the particles in the plasma based accelerators depends mainly on the strong wave field of the plasma wave, the maximum field strength of which is decided by the cold-plasma wave-breaking to be found from Poisson's equation and assuming the oscillating density be the back ground plasma density, and is given

$$E_m \simeq \frac{\omega_p mc^2}{V_p e} \simeq 9.6 \times 10^{-2} N^{1/2} \quad (V/m), \qquad (1)$$

where N is the plasma density in m^{-3}. For example, $N = 10^{24} (m^{-3})$ gives $eE_m \simeq$ 100 GeV/m, which implies that the electrons could be accelerated to 1 TeV in 10 meters. The plasma based accelerators, however, have some difficulties in controlling the plasma itself in order to meet the conditions of the precisely tuned, stable and reliable accelerators.

On the other hand, the field intensity of the electromagnetic wave such as the laser light, for example, is given as

$$E_o \simeq 27\, I_o^{1/2} \quad (V/m) \qquad (2)$$

for I_o in W/m^2. Therefore, $I_o = 10^{19}$ W/m^2 gives $eE_o \simeq 85$ GeV/m, which is almost the same intensity as the plasma wave has. The laser light, however, cannot be used as the accelerator field as it is, because of the transverse wave, and so even if the electrons are injected into the wave area the average energy of the accelerated particles would be canceled out in a cycle; no net energy increment.

The efficient acceleration of electrons has been shown in the $V_p \times B$ accelerator[9], in which charged particles are trapped in the wave trough and accelerated along the wave front, perpendicular to the direction of the wave propagation. When an electromagnetic wave (EM wave) is used as a driver in the accelerator, it is difficult to realize the interaction of charged particles with the wave without any structure such as a slow wave structure, because the EM wave is a transverse mode propagating with a velocity of light in free space. In order to overcome this demand, a new scheme, a multi-electromagnetic wave-beam system (Multi-EM Beam), has been proposed.[10,11] This system consists of a lot of plane electromagnetic-wave beams propagating in parallel each other, but each beam is successively delayed of its phase from the one to the other. If we look over a part of the same phase, it seems that another apparent wave could propagate obliquely with a phase velocity $V_p = c \cdot \cos\theta < c$, where θ is an angle between the propagation direction of two waves, the real transverse wave and the apparent mode. In the slower wave, the charged particles could be trapped in the wave trough to interact with the wave.

We have investigated numerically the motion of charged particles in this system and have obtained the result that the charged particles are really trapped and accelerated stably into high energy. We already have shown a preliminary results earlier,[11] but here in the present paper a

precise numerical investigations have been performed.

In Sec.2 a theoretical review is given, and the results of numerical calculations are presented in Sec.3. Some discussions are given in Sec.4 and the paper is concluded in Sec.5.

2. Theory

1) The case of infinitesimally small beam width and separation.

We consider a multi-beam system consisting of electromagnetic wave-beams (multi-EM-beam system) as schematically shown in Fig.1, in which each beam, which should be considered within a Rayleigh length, propagates in parallel in the z direction. The phase of each beam is slightly delayed with an amount of α from beam to beam. Here, d, h and λ are, respectively, the beam width, the interval of a neighbouring beam and the wave length. Then, the x component of an electric field of the electromagnetic wave E_x, and the y component of a magnetic field B_y can be represented by the following functions,

$$E_x = - E_{x0} \sum_n \sin(kz - \omega t + n\alpha)[u(x - n(d + h)) - u(x - n(d + h) - d)], \quad (3)$$

$$B_y = - B_{y0} \sum_n \sin(kz - \omega t + n\alpha)[u(x - n(d + h)) - u(x - n(d + h) - d)]. \quad (4)$$

Here, u(x) is the step function and $n = 1,2,3,\cdots$.

Therefore, a connectecd line of the same phase makes another apparent wave front which propagates obliquely from the z direction. Now, we select a new coordinate system (x',y',z') which is twisted θ degrees from the original coordinates (x,y,z) as shown in Fig.1. Then, we obtain the electromagnetic field components which propagate in the z' direction:

$$E_x' = -E_{xo}\cos\theta \sin(k'z' - \omega t), \tag{5-a}$$

$$B_y' = -B_{yo}\sin(k'z' - \omega t), \tag{5-b}$$

$$E_z' = -E_{xo}\sin\theta \sin(k'z' - \omega t), \tag{5-c}$$

where all the values with prime denote those measured in the new coordinate system (x',y',z'). Here, we have assumed that the beam width d and the spatial interval h between the neighbouring beams are infinitesimally small, as d/λ and h/λ are much smaller than unity. However, in the later section, the finite size effects will be taken into considerations.

The relation for the phase delay, even in the present assumption of small d and h, is given as,

$$\frac{\alpha}{d+h}\,\frac{\lambda}{2\pi} = \tan\theta. \tag{6}$$

The relationship between the wave length, the wave number and the phase velocity measured in (x,y,z) frame and those in (x',y',z') frame are given, respectively:

$$\lambda' = \lambda\cos\theta, \tag{7}$$

$$k' = k/\cos\theta, \tag{8}$$

$$V_p = c\cdot\cos\theta. \tag{9}$$

In this case, the relativistic parameter, γ_p, measured with the wave phase velocity can be expressed with θ :

$$\gamma_p = (1 - V_p^2/c^2)^{-1/2} = 1/\sin\theta. \tag{10}$$

The phase velocity V_p in Eq.(9) depends on the angle θ, but is always slower than the velocity of light for $\theta > 0$. Therefore the charged particles can interact with the new apparent wave in (x',y',z') frame.

In the present paper, we consider electrons charged for acceleration.

The static magnetic field B_0 which is applied in parallel with the fluctuating magnetic field B_y produces magnetic neutral points denoted (A,B) in Fig.2.[12] The electric field E_x' at both sides of the point A and B are in the same direction, but the magnetic fields are in opposite, so that the attraction force, which comes from the Lorentz force, works on the electrons near the point A and the repulsive force works near the point B. The equations of motion for an electron in such a laboratory frame denoted with prime are given:

$$m_0 \frac{d(\gamma v_x')}{dt} = e\{E_x' - v_z'(B_y' + B_0)\}, \qquad (11\text{-a})$$

$$m_0 \frac{d(\gamma v_y')}{dt} = 0, \qquad (11\text{-b})$$

$$m_0 \frac{d(\gamma v_z')}{dt} = e\{E_z' + v_x'(B_y' + B_0)\}, \qquad (11\text{-c})$$

where m_0 is the rest mass of the electron and γ is the relativistic parameter defined by $\gamma = \{1 - (v_x^2 + v_z^2)/c^2\}^{-1/2} = \{1 - (v_x'^2 + v_z'^2)/c^2\}^{-1/2}$.

If the velocity v_z' of electron is nearly equal to the phase velocity V_p, it is convenient to analyze the motion of the particle expressed in the wave frame (X,Y,Z). The equation of motion Eq.(11-a ~ c), therefore, can be rewritten into the wave frame:

$$m_0 \frac{d(\Gamma V_x)}{dT} = -e\left(\frac{B_y}{\gamma_p} + \gamma_p B_0\right) V_z - e\gamma_p B_0 V_p, \qquad (12\text{-a})$$

$$m_0 \frac{d(\Gamma V_y)}{dT} = 0, \qquad (12\text{-b})$$

$$m_0 \frac{d(\Gamma V_z)}{dT} = e\left((c + V_x)\frac{B_y}{\gamma_p} + V_x \gamma_p B_0\right). \qquad (12\text{-c})$$

Here, all the capital letters represent the quantities measured in the wave frame. However, the values of the magnetic field component are measured in the laboratory frame for convenience in description. Equation (12-c) shows the force balance in the Z direction, and the term for B_y appearing in RHS, which includes "sin(KZ)" as seen in Eq.(5-b), gives rise to either attractive or repulsive force depending on its sign. If the first term in RHS in Eq.(12-c) is always larger than the second term, the magnetic neutral point exists and the electrons could be bunched into the point A, if the following inequality is satisfied,

$$(c + V_x)B_y/\gamma_p > V_x \gamma_p B_0. \qquad (13)$$

When the electron acceleration is considered to occur with a velocity close to the velocity of light, i.e. $V_x \rightarrow c$ in the Eq.(13), the following inequality must be satisfied

$$\frac{B_y}{B_0} > \frac{\gamma_p^2}{2} = \frac{1}{2\sin^2\theta}. \qquad (14)$$

Next, from Eq.(11-a), using the relation $E_x\cos\theta = cB_y\cos\theta = V_pB_y$, we can obtain the expression for energy gain of electrons

$$\frac{d(\gamma v_x')}{dt} = \omega_c V_p B_0, \qquad (15)$$

where $\omega_c = eB_0/m_0$ is the cyclotron frequency measured with the rest mass.

After integration over time with initial values $v_z' = V_p$ and $v_x' = 0$, one obtains

$$v_x' = \frac{V_p \omega_c t}{\gamma_p} \left(1 + \frac{V_p^2 \omega_c^2 t^2}{c^2}\right)^{-1/2}, \qquad (16)$$

and $v_x' \rightarrow c/\gamma_p$ can be obtained for $t \rightarrow \infty$. As the electron velocity in the z' direction is V_p, the total velocity of electron could be increased to

$$v \simeq \sqrt{(\gamma_p/c)^2 + V_p^2} = c.$$

By inserting Eq.(16) into the definition of γ given by the following relation:

$$\gamma = (1-(v_x'^2+V_p^2)/c^2)^{-1/2},$$

the energy gain for electron acceleration can be expressed as,

$$\gamma = \gamma_p(1+(V_p \omega_c t/c)^2)^{1/2} \simeq \gamma_p V_p \omega_c t/c \quad (V_p \omega_c t/c \gg 1). \qquad (17)$$

i.e. γ increases almost linearly with time after enough acceleration of charged particles.

2) The finite beam width effects

So far we have neglected the finite beam size effects, but in the actual case, the beam width, d, and the spatial interval, h, between the neighbouring beams, exists to make considerable effects. In this section, we will specifically discuss the case with the finite beam width d. It is not permitted in this system to assume the smooth wave front propagating in the z' direction. The electron will be delayed from the wave which is propagating along the z axis with light speed as schematically shown in Fig.3. The equations of motion for an electron are written in the components:

$$m_0 \frac{d(\gamma v_x)}{dt} = e(E_x - v_z(B_y + B_0)), \tag{18-a}$$

$$m_0 \frac{d(\gamma v_y)}{dt} = 0, \tag{18-b}$$

$$m_0 \frac{d(\gamma v_z)}{dt} = e v_x(B_y + B_0). \tag{18-c}$$

As the electric field E_x is changing sinusoidally, a half cycle of the wave corresponds to the acceleration phase (in the +x direction) for the electron and another half cycle to the deceleration phase.

Now, we assume that the initial velocity of electron is v_0, the twisting angle of electron is θ and the phase delay, which is produced after passing through one beam width, is α (see Fig.3). Then, as the phase velocity V_p is $\simeq v_0$, the following relationship can hold,

$$\theta = \cos^{-1}(V_p/c) \simeq \cos^{-1}(v_0/c). \tag{19}$$

If the electron is assumed to pass by only the acceleration phase successively from beam to beam, the continuous acceleration of electron can be accomplished. For realizing the system, the following condition on the beam width must be satisfied,

$$d+h < \frac{\lambda}{2} \frac{1}{\tan\theta} = \frac{\lambda}{2} \frac{1}{(\gamma_p^2 - 1)^{1/2}}. \tag{20}$$

This expression shows that the beam width can be determined only by the phase velocity V_p with a constant wave length (or a wave frequency).

When the finite size beams of EM wave are employed, the beam shape makes a key effect on the acceleration characteristics. In general, the laser beam has a Gaussian distribution in its cross section. Therefore, the multi-beam system could be assumed to have the shape expressed in Eq.(21),

$$E_x = E_{x0}\exp[-w\cdot\sin^2\{\frac{\pi}{d}(x' + \frac{d}{2})\}]\sin(k'z' - \omega t). \qquad (21)$$

The schematic structure of the cross section is shown in Fig.4. If w = 0, the beams are distributed uniformly in the x' direction, which corresponds to the case Sec.2-1. As w increases in Eq.(21), each beam has Gaussian cross section but distributes narrower and narrower in space.

3. Numerical calculations and results

1) The case of neglecting effects from finite beam width

As previously described, the beam width, d, and the spatial interval between the beams, h, are assumed infinitesimally small, for simplicity, $d \sim h \simeq 0$, and so the beams have apparently continuous structure, but the phase is gradually changing between them. Equation (12-a ~ c) can be used as the fundamental equations in this case. They must be calculated numerically by adding the equation $dX/dT=V_x$, $dY/dT=V_y$ and $dZ/dT=V_z$. We assume that the initial velocity $V_x(T = 0)$ in the X direction is zero. In order to perform calculations, the Runge-Kutta method is employed.

We took θ, B_0, B_y and E_x as parameters. The frequency of the EM-wave employed for the numerical calculations is 30 GHz, so that the wave length is 1 cm, and the wave number, k, is fixed to be 200π throughout the calculations.

(a) *The case of satisfying trapping condition*

When the trapping condition (Eq.14) of the electrons in a wave trough is satisfied, all the particles could never fly out from the wave. The typical results of this case are shown in Fig.5. Figure 5(a) displays the time history of the velocity V_x in the phase space and that of V_z in

Fig.5(b). The abscissa shows the phase kZ ($0 \sim 2\pi$) in one wave length. In the initial state, 400 electrons are injected uniformly into the whole phase-space ($0 \leq kZ \leq 2\pi$, $-0.1 \leq V_z/c \leq 0.1$), and the initial velocity in the X direction V_{x0} is 0. Here, the injection angle θ and the vertical magnetic field B_0 are decided by Eqs.(9) and (14) to give $\theta = 24.9°$ and $B_0 = 5$(G), respectively. The following parameters are kept constant throughout the calculations:

$E_x = 900$(kV/m), $B_y = 30$(G), $f = 30$(GHz), and $V_{z0}/c = 0.9$.

The corresponding trapping condition is $B_0 < 11.3$(G), which is fully satisfied in the present parameters. When time proceeds, it is clearly seen in Figs.5(a) and (b) that the particle bunching in the phase space and acceleration in the X direction occur. In this conditions, all the particles could remain in the same phase space as the trapping condition is satisfied. In order to clarify the trapping structure more precisely, the particles remaining in a wave length at the time $\omega T \gamma_p = 997$ are projected back to their initial positions in the phase space as an example is shown in Fig.6(a). In Fig.6(a), the particles injected in the center area are the ones trapped in the wave trough for a long duration. Those which exist at the top right hand corner having initial velocity $V_{z0}/c \simeq 0.05$ flow out to the next phase space because of no trapping. Although the initial velocity of each particle does not precisely coincide with the phase velocity of the wave in this scheme, still the electrons can interact strongly with the EM wave, and the electron trapping and acceleration occur.

Figure 6(b) shows an typical example of orbits of selected electrons in the phase-space. Here, we chose some typical initial conditions. As seen from the figure, some particles with $kZ = 0.8\pi$ and $V_z/c = 0.03$ are trapped well within the wave trough, while some others are not trapped to fly out. This point will be discussed in the later section.

(b) *The case of unsatisfied trapping condition*

Next, we have performed calculations on the electron motion under unsatisfied trapping condition. The examples of the parameters in this case are:

E_x = 300(kV/m), B_y = 10(G), f = 30(GHz), B_0 = 5(G), $V_p = v_0 = 0.9c$, and θ = 24.9°, which are kept constant throughout the calculation. The trapping condition is obtained $B_0 < 3.8$(G). An example of numerical calculations is shown in Fig.7. All the electrons in this case are detrapped in some stages, and finally delayed from the wave not to show the stable bunching of the particles, although some amounts of energy increment are observed.

2) The case of finite beam width

In the real system, the beam width d must be of finite size and the effects from this have to be taken into considerations. The numerical calculations have been performed based on the results given in Sec.2-2 by adding the relationship $dx/dt = v_x$, $dy/dt = v_y$ and $dz/dt = v_z$ with both a rectangular shaped and a Gaussian shaped beam. Note that in this case, the calculation have been performed in the coordinate system (x,y,z) because of easier to do.

(a) *The case with rectangular beam*

At first we have performed calculations with rectangular shaped beams. The typical example of the results are shown in Figs.8 (a) and (b), which show the variation of electron energy as a function of the time. The parameter of Fig.8(a) is the beam width d, and that of Fig.8(b) is the static magnetic field B_0. Other parameters are kept constant: E_x = 210(kV/m), B_y = 7(G), $V_p = v_0 = 0.99c$ ($\gamma_p = 7.1$), and f = 30(GHz). The static magnetic field

B_0 in Fig.8(a) is $B_0 = 0.25$ (G) which is below the critical value of trapping electrons of $B_c = 0.27$(G) calculated from Eq.(14). The beam width condition also has a restriction as is given by $d+h < 3.5\lambda$. Initially all the electrons are located at $z_0 = 0$. Figure 8(a) shows the calculated results, in which the trapping condition is satisfied and in Fig.8(b) the restriction on the beam width is satisfied. When the condition for the beam width is not satisfied, the electron can be accelerated continuously up to the time when the electrons come into the deceleration phase, but after that the electron energy does not increase anymore.

When the static magnetic field B_0 is larger than the value for the particle trapping, the electron energy can increase in early stage of the acceleration, but as the time passes by, the electron is detrapped from the wave trough and its energy does not increase anymore as seen in Fig.8(b).

Figure 9 shows the phase space display of the electron energy as a parameter of time variation. The abscissa is the phase in a wave length of the EM-beam propagating to the z direction with a speed of light. Initially all the electrons are injected uniformly in a phase space with a velocity $|v| = V_p$. Other parameters are $E_x = 210$(kV/m), $B_y = 7$(G), $f = 30$(GHz), $d = \lambda$, $h \rightarrow 0$, and $v_0 = V_p = 0.9c$ ($\gamma_p = 2.3$). The critical value, B_c, for electron trapping is $B_c = 0.27$(G), and the condition for a beam width is $d+h < 3.5\lambda$. It is clear from the figure that almost all the electrons are bunched to be accelerated and the particle energy increased in the phase-space. The bunching point is moving to be delayed from the wave phase. This is because that the phase in the abscissa is fixed to the EM-beam frame which is propagating with the speed of light, and so the electron is delayed from the wave beam to be taken over into the next neighbouring wave beam, where the wave phase is the acceleration phase. As a result, the continuous acceleration of electrons occurs. This is

exactly the characteristic nature of the Multi-EM-Beam accelerator system.

(b) *The case of Gaussian shaped beam*

When the cross section of the electromagnetic wave beam has the Gaussian distribution described in Eq.(21), still the trapping condition is fulfilled, the situation of the particle acceleration could change. The typical results of numerical calculation are shown in Fig.10 under the condition that the particles are trapped well within a wave trough. Here, the cross section of the beam shape changes depending on the w values in Eq.(21), and a typical shape with changing w has been shown in Fig.4. By using this beam, we have performed calculations on the particle acceleration similar to those shown previously. When 400 electrons are injected uniformly into the whole phase-space ($0 \leq kZ \leq 2\pi$, $-0.1 \leq V_z/c \leq 0.1$), the electrons are bunched to be accelerated into high energy as seen in Fig.10(a)-(b). However, the bunching strength seems to be weak compared with the previous case (see Fig.5), still the electron energy increases quite clearly.

4. Discussion

In the numerical calculations we have obtained enough acceleration of electrons in the multi-EM-beam system, even if each beam is the transverse wave. In order to understand the underlying mechanism more precisely, we have tried to obtain an effective potential in a wave frame propagating along the z' axis.

From the equation of motion Eq.(11-a), after the integration over T, one obtains for V_x

$$V_x = [\Gamma_o V_{xo} + \omega_c \gamma_p V_p (T - T_o) + \omega_c \gamma_p (W(Z) - W(Z_o))] / \Gamma, \quad (22)$$

where

$$W(Z) = Z + \frac{1}{\gamma_p^2}\frac{B_y}{B_o}\frac{1}{K}\cos(KZ).$$

By replacing $dT = \Gamma\, d\tau$, one obtains from Eq.(11-c)

$$LHS = \frac{1}{\Gamma}\frac{d^2Z}{d\tau^2}, \tag{23}$$

$$RHS = -\omega_c \left\{ V_x \gamma_p - (V_p \tan\theta + V_x)\frac{1}{\gamma_p}\frac{B_y}{B_o}\sin(KZ) \right\}.$$

After inserting Eq.(22) into (23) with putting $V_{xo} = 0$, one can finally obtain

$$\frac{d^2Z}{d\tau^2} = -\frac{dU(Z)}{dZ} + F(\tau), \tag{24}$$

where

$$F(\tau) = \Gamma(\tau)\,\omega_c V_p \tan\theta \frac{1}{\gamma_p}\frac{B_y}{B_o}\sin(KZ)$$

$$- \omega_c^2 \gamma_p^2 V_p \Gamma(\tau)\,\tau \left\{ 1 - \frac{1}{\gamma_p^2}\frac{B_y}{B_o}\sin(KZ) \right\}, \tag{25}$$

$$U(Z) = \frac{\omega_c^2 \gamma_p^2}{2}\left[W(Z)^2 - 2\left\{ W(Z) - \frac{W_o}{\omega_c \gamma_p} \right\} W(Z) \right], \tag{26}$$

with $W_0 = \Gamma_0 V_{x0} + \omega_c \gamma_p V_p T_0$. Equation (24) shows that the charged particles are moving in the equivalent potential U(Z), but that the existing of the function $F(\tau)$ exhibits to prevent the particle entrance into the next wave phase, because the potential becomes higher. The qualitative representation of the potential U(Z) is shown in Fig.11. In this example, the initial conditions were $V_{x0} = 0$ and $T_0 = 0$, and the particles were at $Z_0 = 0$. When the trapping condition Eq.(14) is satisfied, the potential well exists at certain phase ① or ② such as shown in Fig.11(a), and most of the particles represented by closed circles are trapped within this well. Some others denoted by open circles, however, cannot be trapped there depending on their initial phases. The particles, which are trapped within the well, can be accelerated to high enough energy.

If the trapping condition is not satisfied, the potential U(Z) has no well such as schematically shown in Fig.11(b), and the particle trapping necessary for enough acceleration does not occur.

The equivalent potential U(Z) is expressed by the quadratic function of W(Z), which means that U(Z) consists of the quadratic and the sinusoidal function as W(Z) includes the sinusoidal function. Therefore, the depth of the well becomes larger as the phase KZ. This, however, does not mean that the particles can be trapped easier as the phase becomes larger. In order to proceed the phase, say, for one wave length, some forces in the z direction have initially to act on electrons. In general, the phase velocity of the wave and the initial velocity of electrons in the z direction must be close to each other, for the strong interaction of the particles with the wave. Therefore, it is hard to imagine that the electrons initially come into the advanced phase by one wave length.

As mentioned above, the equivalent potential can be obtained from the

equation of motion, and the hill and well appear in this when the static magnetic field B_o is applied to satisfy the trapping condition of the particles. The well in the equivalent potential corresponds to the magnetic neutral point A in Fig.12 where the attractive force appears to bunch particles. The hill also corresponds to the magnetic neutral point but almost out of phase from the well and the repulsive force appears such as the point B in the same figure. The electrons in the phase space are affected from the potential structure including the hill and well as seen in Figs.5 and 7.

In the present system the most attractive merit is to use no slow wave structure such as necessary for the VpxB accelerator using TM mode. In order to realize the electron linear accelerator by using the present system, the quite precise adjustment is required for EM-beam handling. The Multi EM-beam accelerator should have many beams and satisfy several conditions such as (1) each beam should be slightly and precisely phased, (2) all EM-beams are in parallel at least in the acceleration area (or within a Rayleigh length), and (3) the beam width has also restriction given by Eq.(20). These conditions are not so difficult to realize with the present technology, if we could use the laser beams or short wave length microwave beams. An example of one realistic alignment for the electron linear accelerator is shown schematically in Fig.13, in which one rf beam source makes multi-beam system for acceleration and the wave energy could be used efficiently until the wave depletion becomes seriously important.

The acceleration rate of the present system can be compared with other systems using different acceleration principle such as the VpxB accelerator based on the TM mode and the conventional linear accelerator. The energy gain in the V_pxB accelerator with use of TE mode, and TM mode as well, can be expressed in Eq.(17), which is able to be rewritten by using

the coordinate x or z as follows,

$$\gamma = \gamma_p \{1 + \omega_c V_p \gamma_p x / c^2\}, \qquad (27\text{-a})$$

$$= \gamma_p \{1 + (\omega_c z / c)^2\}^{1/2}. \qquad (27\text{-b})$$

The energy increment, therefore, can be expressed as follows;

$$\frac{d\gamma}{dt} = \omega_c (\gamma_p^2 - 1)^{1/2}, \qquad (\text{for } t \gg c/V_p \omega_c) \quad (28\text{-a})$$

$$\frac{d\gamma}{dx} = \frac{\omega_c}{c} \gamma_p (\gamma_p^2 - 1)^{1/2}, \qquad (28\text{-b})$$

$$\frac{d\gamma}{dz} = \frac{\omega_c}{c} \gamma_p. \qquad (28\text{-c})$$

We can see from Eq.(28) that the energy increment depends on the wave phase velocity and the static magnetic field strength, and also see that the particles can be accelerated more effectively in the x direction by the amounts of γ_p ($\gg 1$) compared with the wave propagation direction (z direction). Although Eq.(28) gives the same acceleration rate independent of the acceleration principle, that is, the same amount of static magnetic field with the same phase velocity gives exactly the same energy increment independent of the acceleration principle. However, each principle has different trapping condition for B_o as is given,

$B_0 < 2B_y/\gamma_p^2$, (for Multi EM-beam) (13-a)

$B_0 < E_z/\gamma_p c$, (for TM mode)[9]

and the energy increment should be different in each system.

In general, the increment of particle energy depends on the wave field strength E_z (TM mode accelerator) or B_y (or E_x)(TE mode accelerator) as well as the static field strength B_0. In the conventional linear accelerator, there is, of course, no static magnetic field, and the energy increment is linearly proportional, in principle, to the wave electric field strength E_z and the machine length L.

Here, we compare the energy increment in different system when the magnetic field strength is at the critical value for particle trapping. In this situation we can obtain,

$$\frac{d\gamma}{dz} \propto \frac{2V_p}{\gamma_p c} \quad \text{(for multi EM-beam)} \qquad (29\text{-a})$$

$$\propto V_p. \quad \text{(for TM mode)} \qquad (29\text{-b})$$

The numerical examples are shown in Fig.14, in which we can see that the TM mode accelerator has better energy increment as V_p increases. The multi EM-beam system has the maximum energy increment in even smaller value of V_p/c. If this is very close to unity, $d\gamma/dt$ is sharply smaller with $1/\gamma_p$.

An example of the necessary parameters for obtaining certain amount of energy in each system can be calculated numerically by using Eqs.(27) and (28). The results are shown in Table 1, in which the particles having initial energy 1 MeV could be accelerated up to 1 GeV. Here, Δz (Δx) is

the minimum machine length in the z (x) direction necessary for obtaining the restricted amount of energy, and $E_x(E_z)$ and B_y are the wave field strength in each component, respectively. As clearly seen from Table 1, the most compact accelerator is the V_pxB linear accelerator with TM mode and then the multi-EM-beam mode one in this energy range.

5. Conclusion

We have discussed the trapping and acceleration of electrons in a new system: multi-electromagnetic wave beam system. In this system, we can use the transverse-wave with a phase velocity equal to the light speed c. By operating the phase shift between each EM beam, the effective slow wave structure can be realized for the strong interaction with electrons. Adding the static magnetic field B_0 in parallel with the wave field B_y, which is perpendicular to the wave propagation direction, the V_pxB acceleration mechanism can be constructed. When the trapping condition and the condition for the beam width are satisfied, electrons are trapped at the magnetic neutral point and can be accelerated to high energy close to the velocity of light. The acceleration mechanism has been analyzed by introducing the equivalent potential which shows the bunching and trapping of electrons. The numerical calculations have shown that the V_pxB accelerator schemes including the present multi-EM-beam system and the TM mode scheme are superior to the conventional linear accelerator. For realizing the present multi-EM-beam mode accelerator, the system with multi-mirrors but using single coherent EM wave beam is proposed.

Acknowledgement

The authors are greatly appreciated Prof. R.Sugihara and Dr. S.Takeuchi for their vivid discussions. A part of the present work is

supported by the Grant-in-Aide from the Ministry of Education, Science and Culture, Japan.

References

1. "Laser Acceleration of Particles" edit. by C.Joshi and T.Katsouleas, AIP Conference Proceedings No.130, American Institute of Physics, New York (1985), and references therein.
2. R.Sugihara and Y.Mizuno, J. Phys. Soc. Japan 47, 1290 (1979).
3. T.Katsouleas and J.M.Dawson, Phys. Rev. Lett. 51, 392 (1983).
4. Y.Nishida, M.Yosizumi and R.Sugihara, Phys. Lett. 105A, 300 (1984).
5. P.Chen, J.M.Dawson, R.W.Huff, and T.Katsouleas, Phys. Rev. Lett. 54, 693 (1985).
7. H.Nakanishi, A.Enomoto, K.Nakajima, A.Ogata, T.Urano, Y.Nishida, S.Ohsawa, T.Oogoe, and H.Kobayashi, Part. Accel. 32, 1645 (1989).
6. J.B.Rosenzweig, D.B.Cline, B.Cole, H.Figueroa, W.Gai, R.Koneeny, J.Norem, P.Schesson, and J.Simpson, Phys. Rev. Lett. 61, 98, (1988).
8. Y.Nishida and R.Sugihara, Laser Interaction and related Plasma Phenome na, Vol.7, Chap.9, p. 803 (1986). Plenum, New York.
9. Y. Nishida, N.Yugami, H.Onihashi, T.Taura, and K.Otsuka, Phsys. Rev. Lett. 66, 1854 (1991), and references therein.
10. R.Sugihara, Jpn.J. Appl. Phys. 30, 76 (1991).
11. Y.Nishida and K.Otsuka, Proc. of Inter. Conf. on Plasma Phys., New Delhi, India (1989), Vol.2, pp. 605-608.
12. S.Takeuchi, K.Sakai, M.Matsumoto, and R.Sugihara, Phys. Lett. A122, 257 (1987); IEEE Trans. Plasma Sci. PS-15, 251 (1987).

Figure captions

Fig.1. Schematic description of multi-electromagnetic wave beam system.

Fig.2. Electron acceleration in a transverse wave propagating across the static magnetic field which is applied in parallel with the fluctuating magnetic field of the wave. Point A denotes the bunching phase of elec trons, and point B refers to the repulsive phase.

Fig.3. Schematic description of the locus of electron beam measured in a wave frame.

Fig.4. Cross section of EM wave beam. $w = 0$ in Eq.(21) corresponds to the uniform amplitude in space, $w \neq 0$ refers to the Gaussian beams.

Fig.5. Electron distribution in the phase space with $d \rightarrow 0$, (a) V_x/c vs. KZ, and (b) V_z/c vs. KZ. Initially 400 electrons were uniformly distributed in each phase space.

Fig.6. Electron locus measured in the phase space. (a) Initial state of trap ped electrons which is projected back from the state measured at $\omega \gamma_p T = 997$.

Here, kZ_o shows the initial phase and V_{zo}/c refers to the initial velocity. (b) Electron locus in the phase space. Particles move along the arrow on each locus.

Fig.7. Electron distribution in the phase space with the trapping condition Eq.(14) unsatisfied. (a) V_x/c vs. KZ and (b) V_z/c vs. KZ.

Fig.8. Electron energy as a function of the acceleration time. (a) EM beam width is a parameter. $B_o = 0.25$ (G). (b) Static magnetic field strength B_o is a parameter. $d = h = \lambda/2$. Here, the critical value for particle trapping is $B_c = 0.27$ (G), $E_x = 210$ (kV/m), $V_p/c = 0.99$ ($\gamma_p = 7.1$), and f= 30 (GHz).

Fig.9. Electron energy distribution in a phase space. $E_x = 210$ kV/m, $B_o = 0.25$ G, $V_p/c = 0.9$ ($\gamma_p = 2.3$), $d = \lambda$, and $h = 0$.

Fig.10. Electron distribution in the phase space in the limit of d $\rightarrow$ 0. (a)V_x/c vs. KZ, and (b)V_z/c vs. KZ. E_x = 900 (kV/m), B_0 = 5 (G), θ = 24.9°. V_p/c = 0.9 (γ_p= 2.3), and f = 30 (GHz). The critical value for a particle trapping is B_c= 11.3 (G).

Fig.11. Particle locus in the phase space. (a)The initial state which is projected back from the state observed at the time $\omega \gamma_p T$ =1358. (b) Particle locus in the phase space. The initial conditions are denoted within the figure.

Fig.12. The equivalent potential U in which the electrons existing in the phase space are governed. (a) The particle trapping condition is satis fied, and (b) the trapping condition breaks. Particles existing in the phase ① and ② are trapped in the potential well, otherwise are moving freely.

Fig.13. Schematic structure of a realistic linear accelerator concept. 1: electron beam, 2: focussing mirrors, and 3: laser beam.

Fig.14. Energy increment as a function of the phase velocity. Comparison is made within several accelerator concepts. (a) Dielectric:TE wave accelerator using dielectrics for reducing the phase velocity. (b)Present mode (Multi-EM-beam) accelerator. (c) TM-mode accelerator known as the V_pxB accelerator.

Table 1. Parameters necessary for electrons with energy 1 MeV to be accelerated up to 1 GeV.

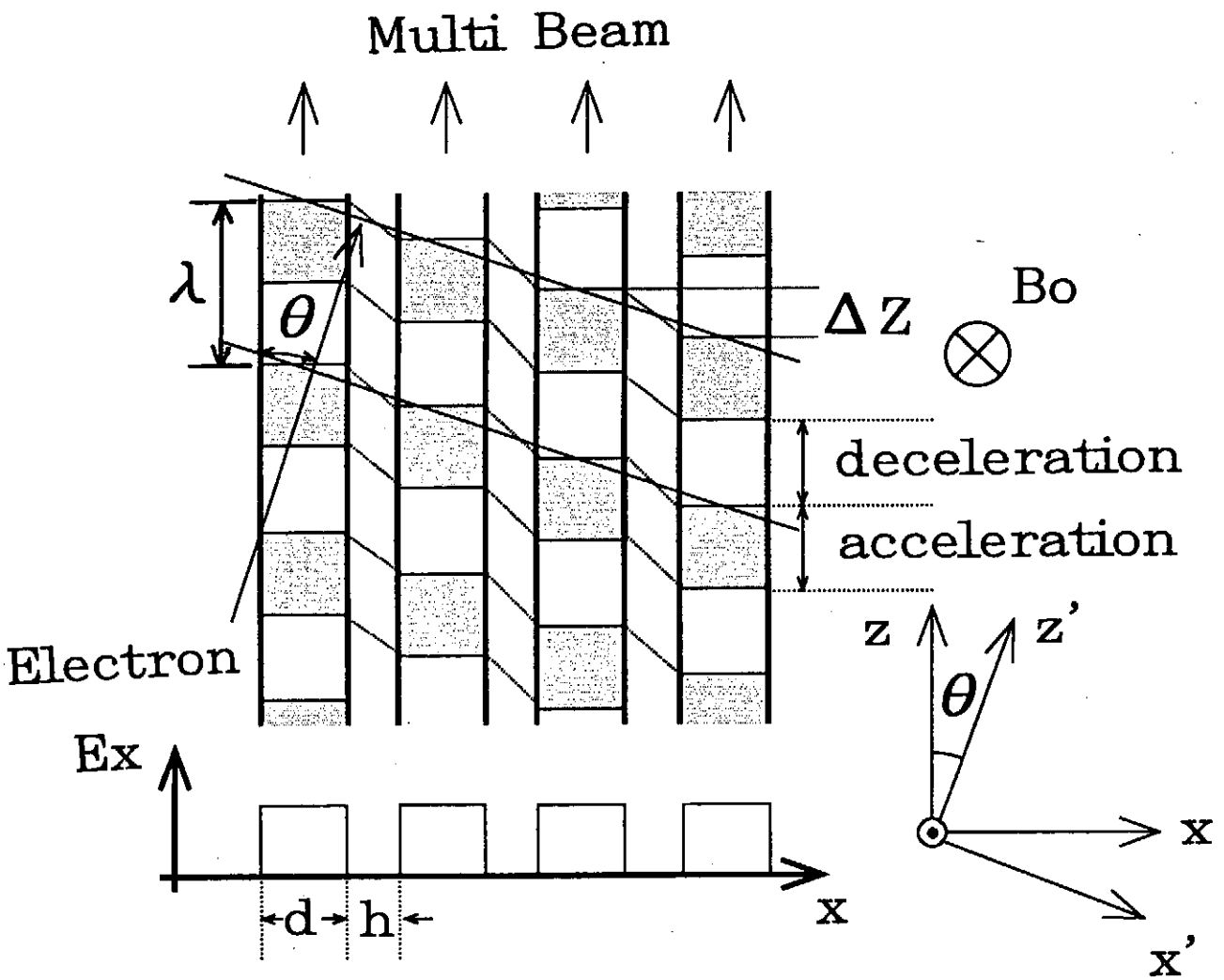
Multi Beam
λ
θ
ΔZ
Bo
deceleration
acceleration
Electron
Ex
d
h
x
z
z'
θ
x
x'

Fig. 1

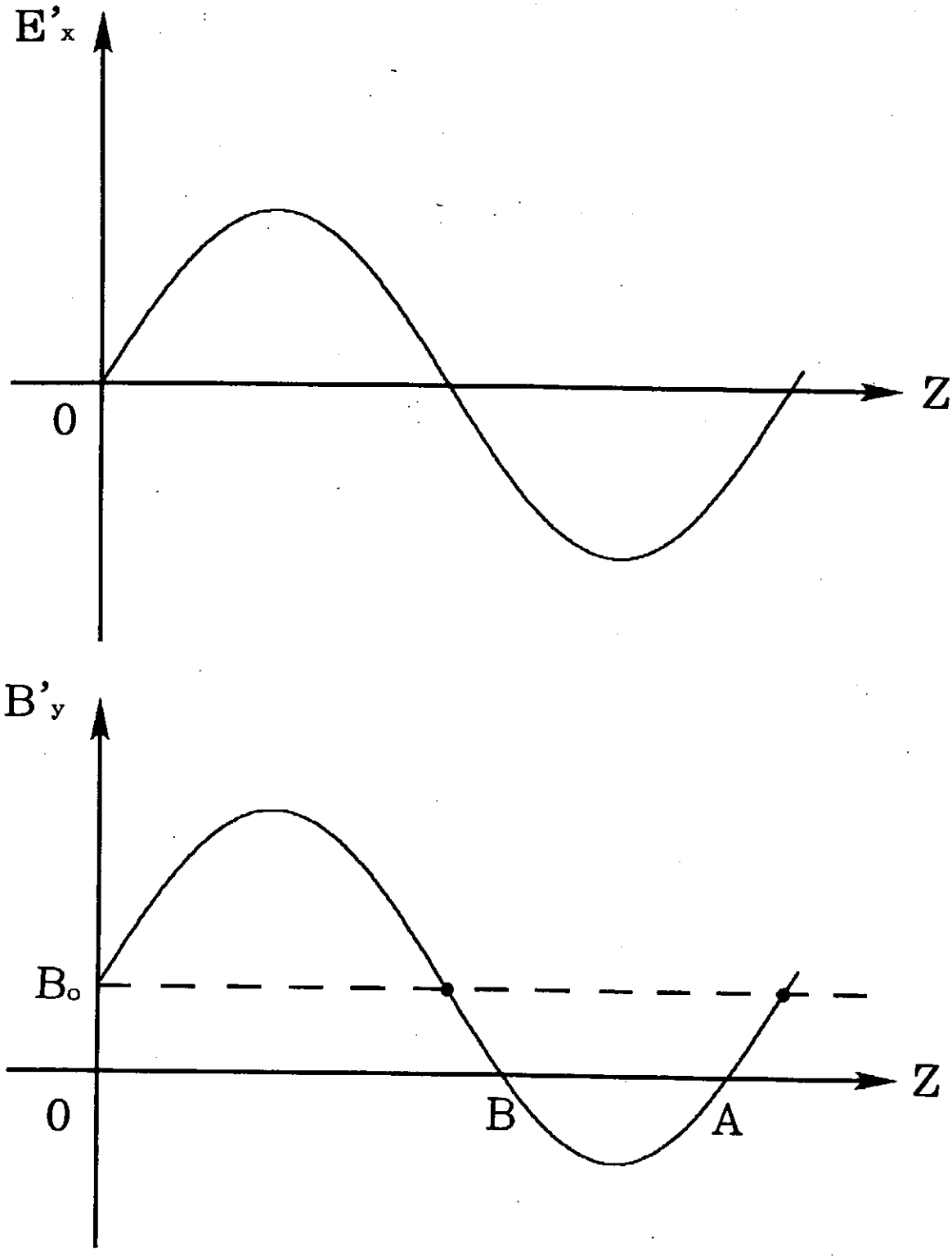

Fig. 2

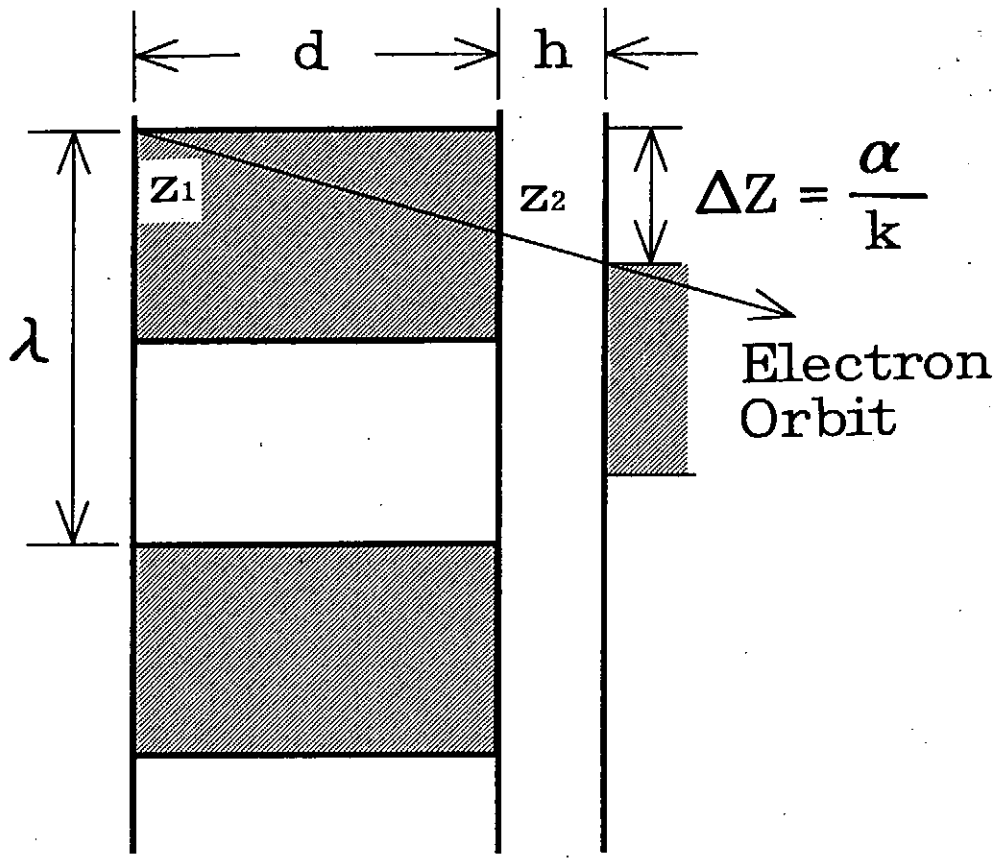

Fig. 3

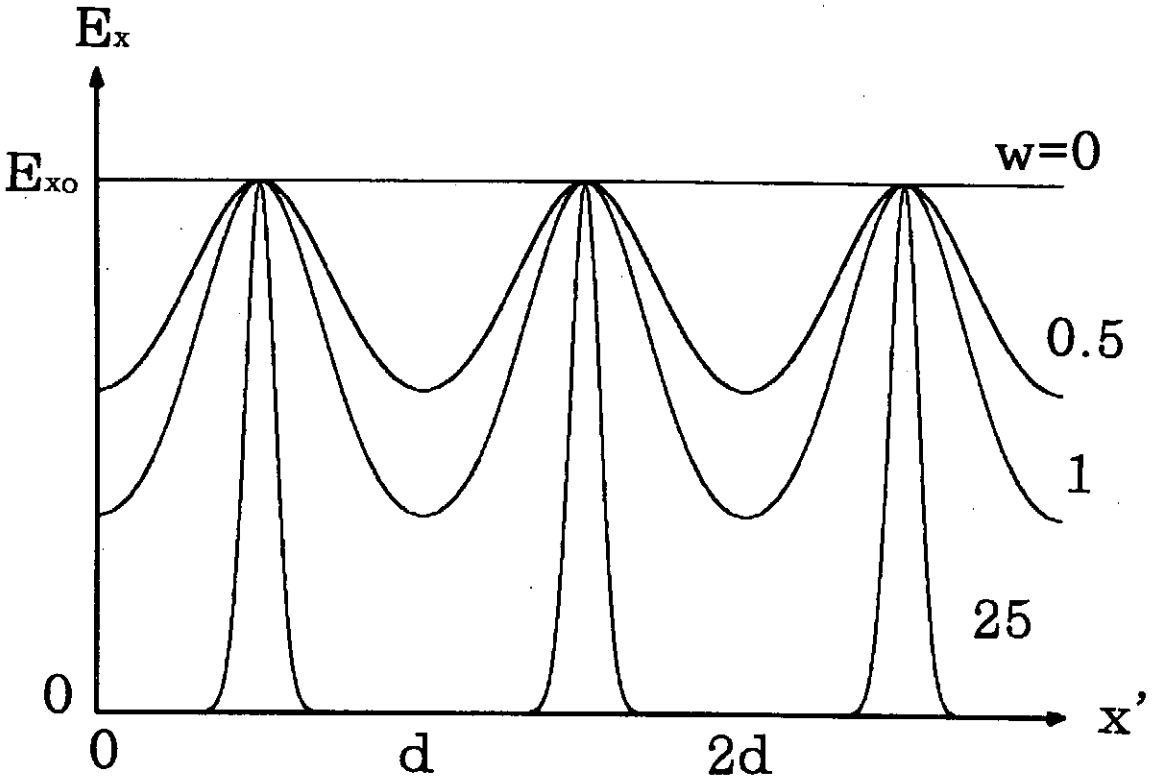

Fig. 4

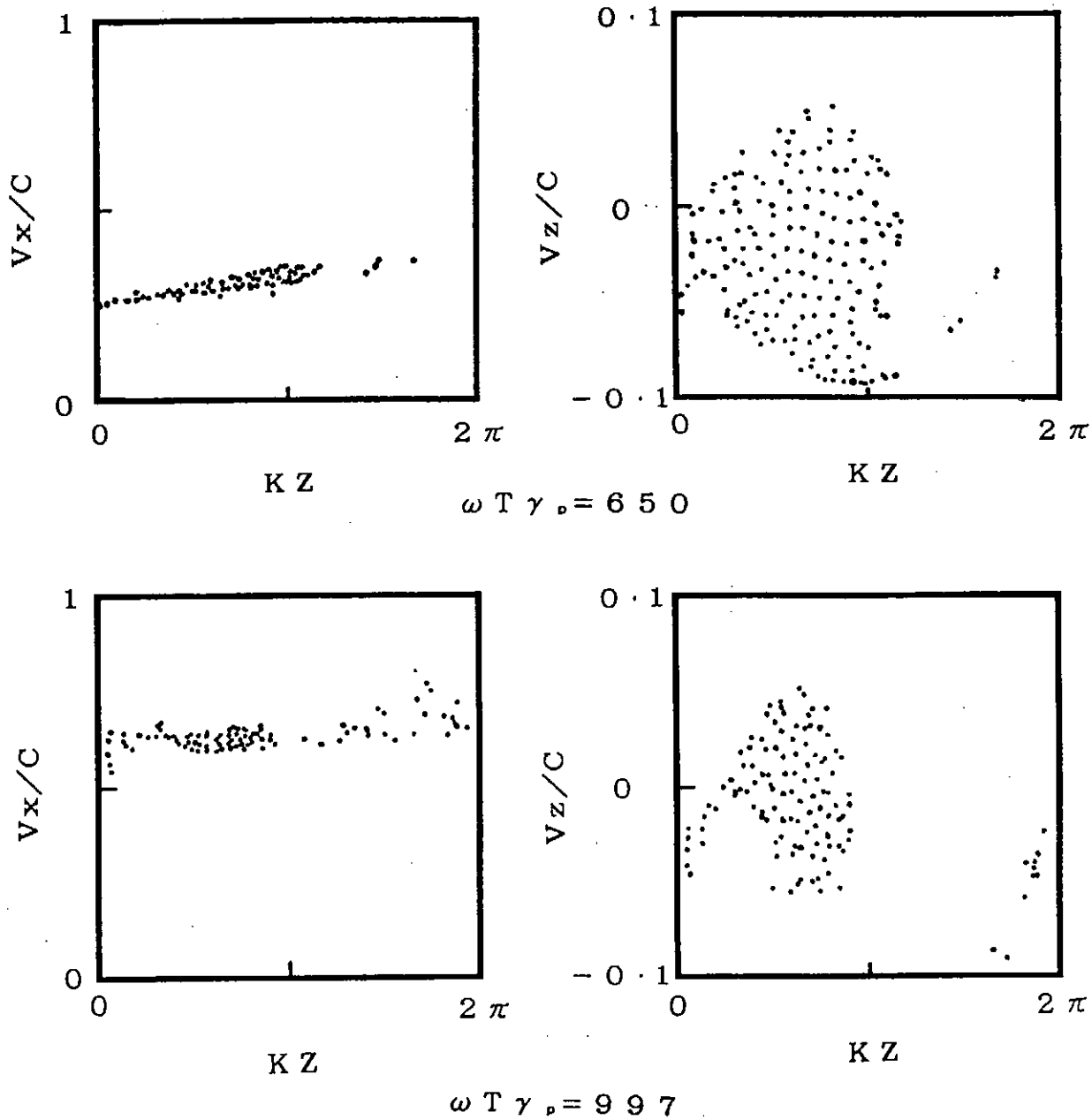
1
0
Vx/C
0
2 π
K Z
0 · 1
0
− 0 · 1
Vz/C
0
2 π
K Z
ω T γ p = 6 5 0
1
0
Vx/C
0
2 π
K Z
0 · 1
0
− 0 · 1
Vz/C
0
2 π
K Z
ω T γ p = 9 9 7
(a)
(b)

Fig. 5

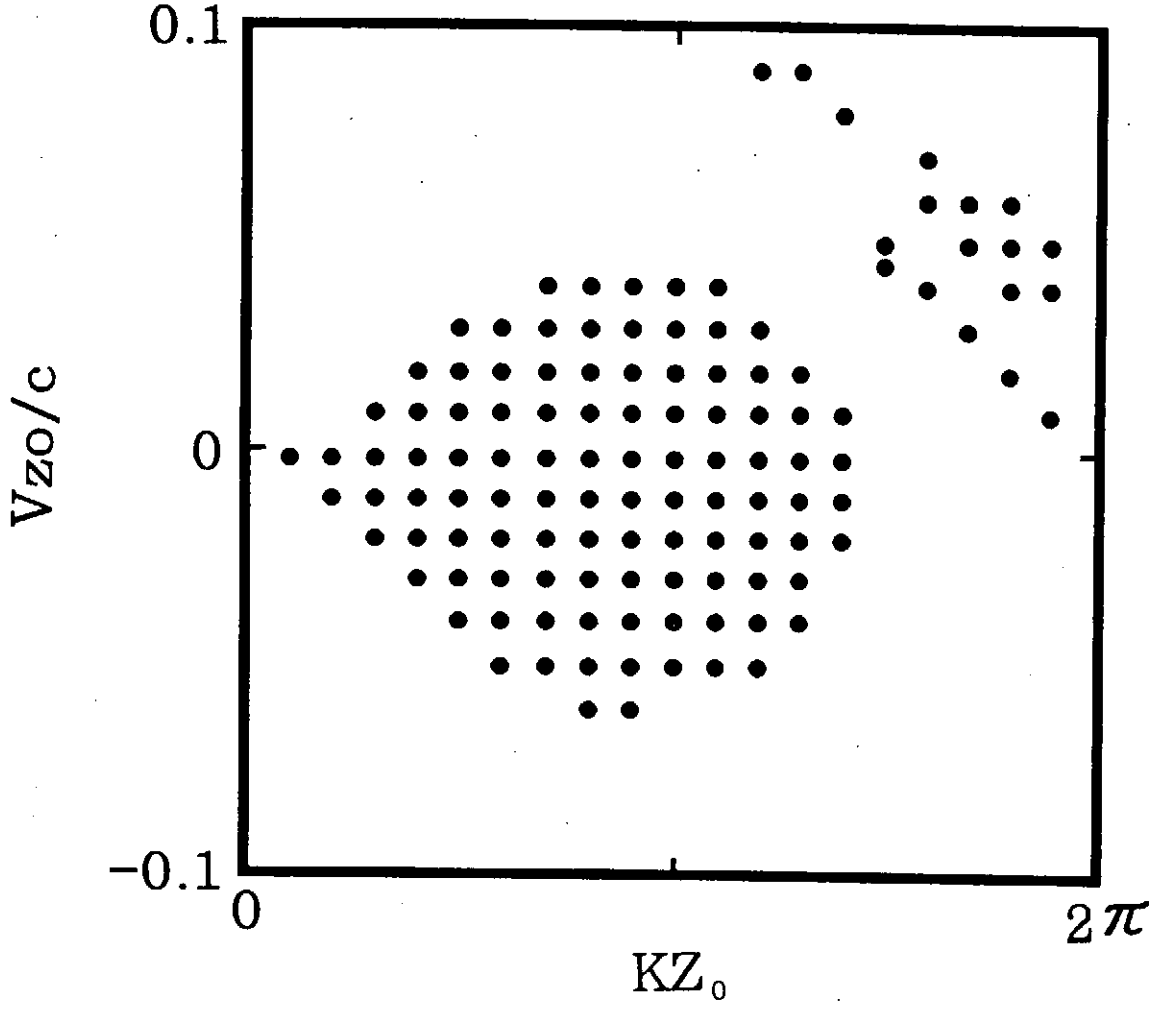

Fig. 6 (a)

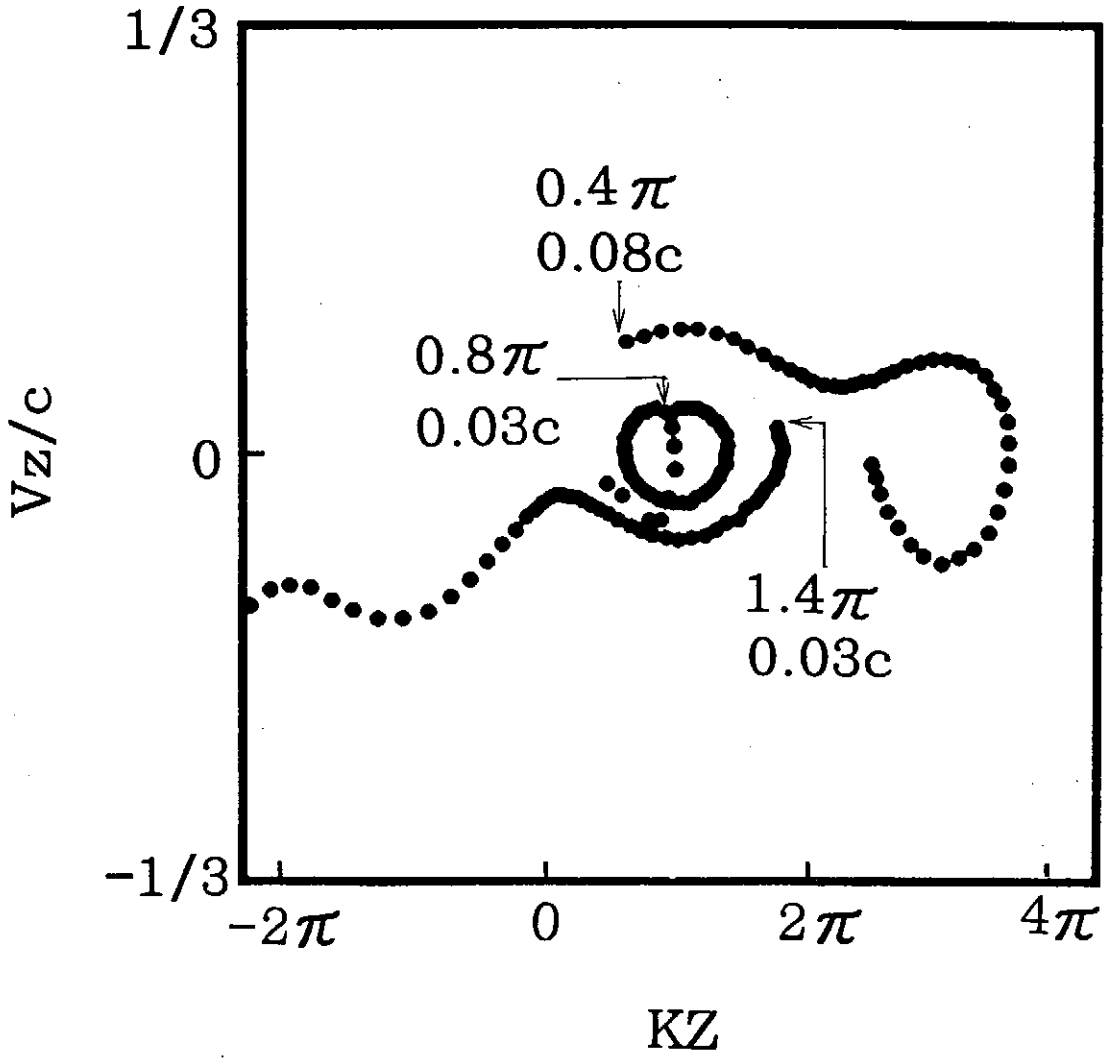

Fig. 6 (b)

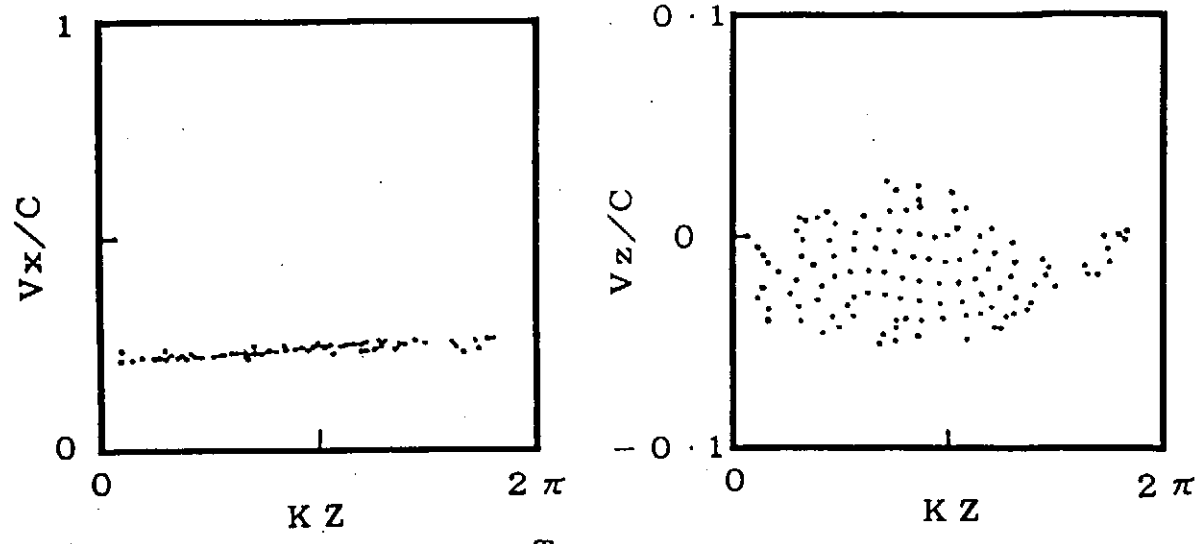

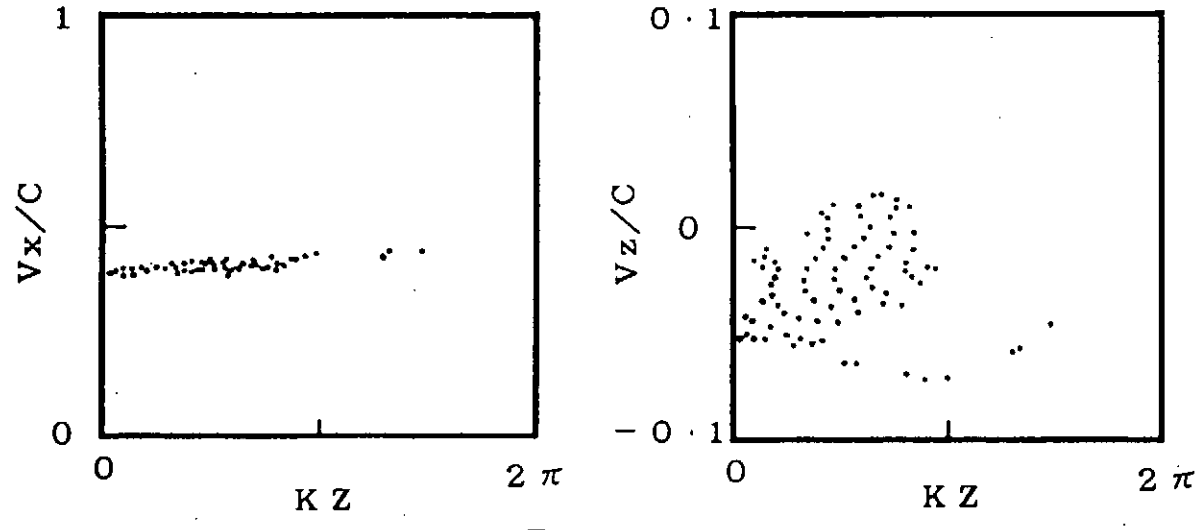

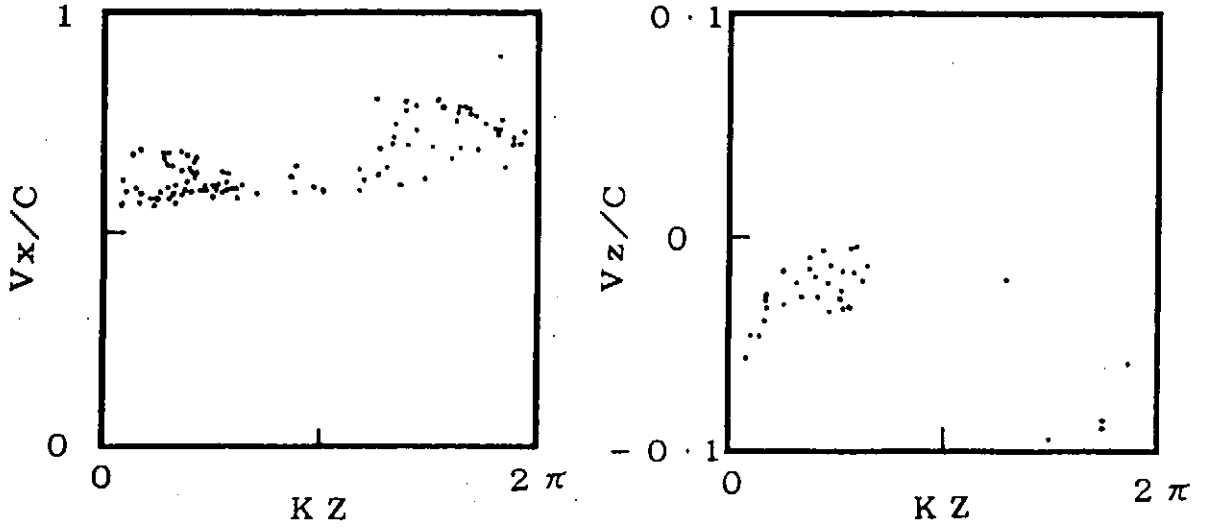

(a) (b)

Fig. 7

K. Otsuka et al.

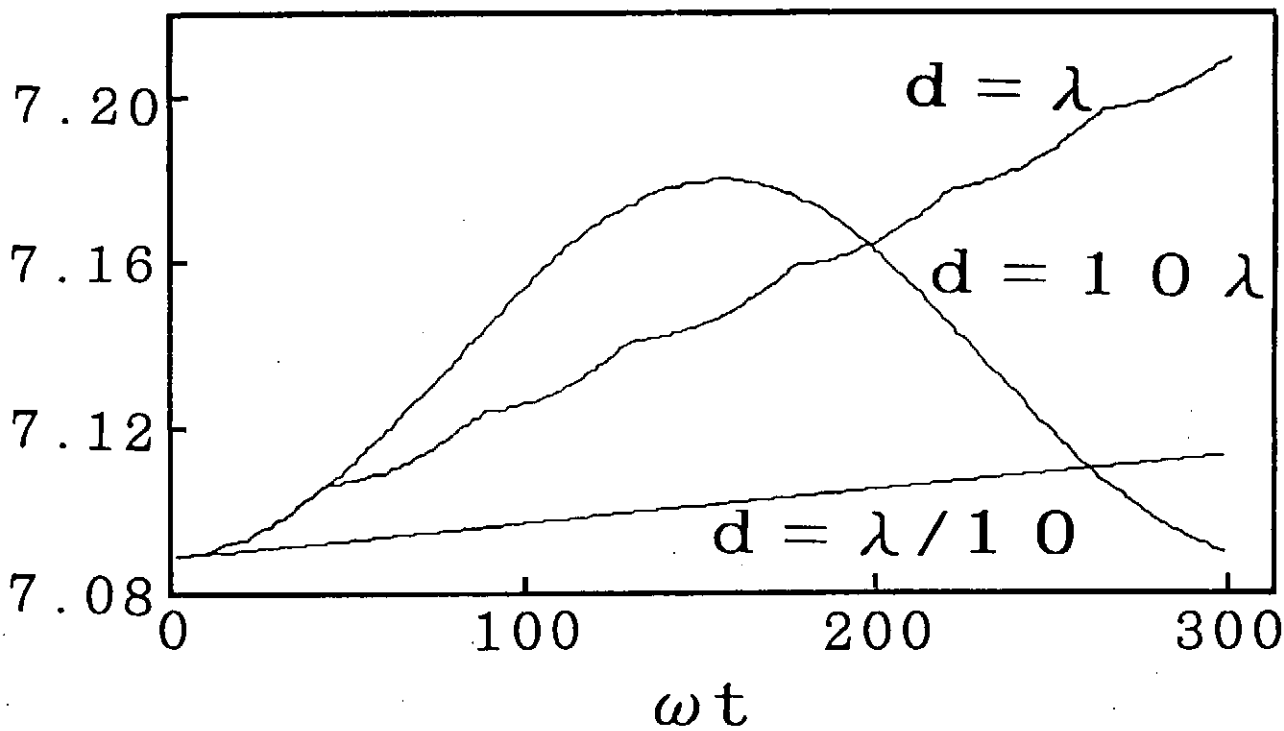

Fig. 8 (a)

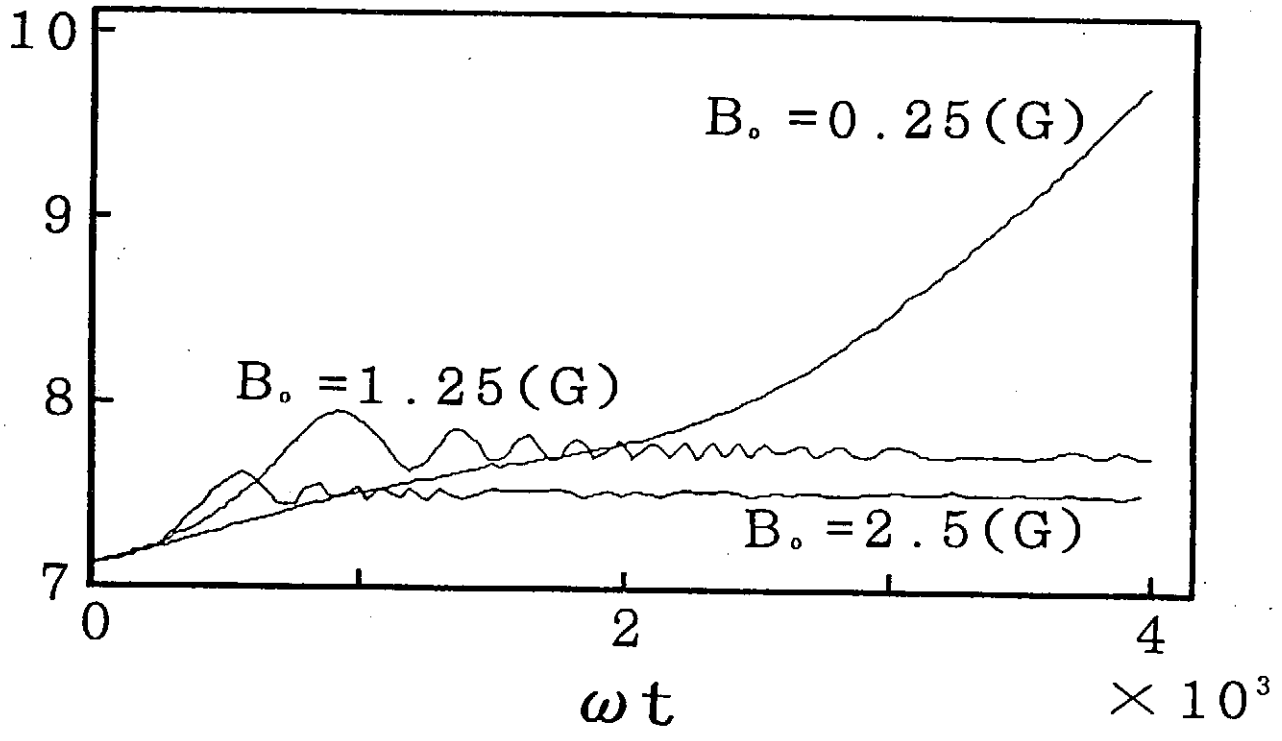

Fig. 8 (b)

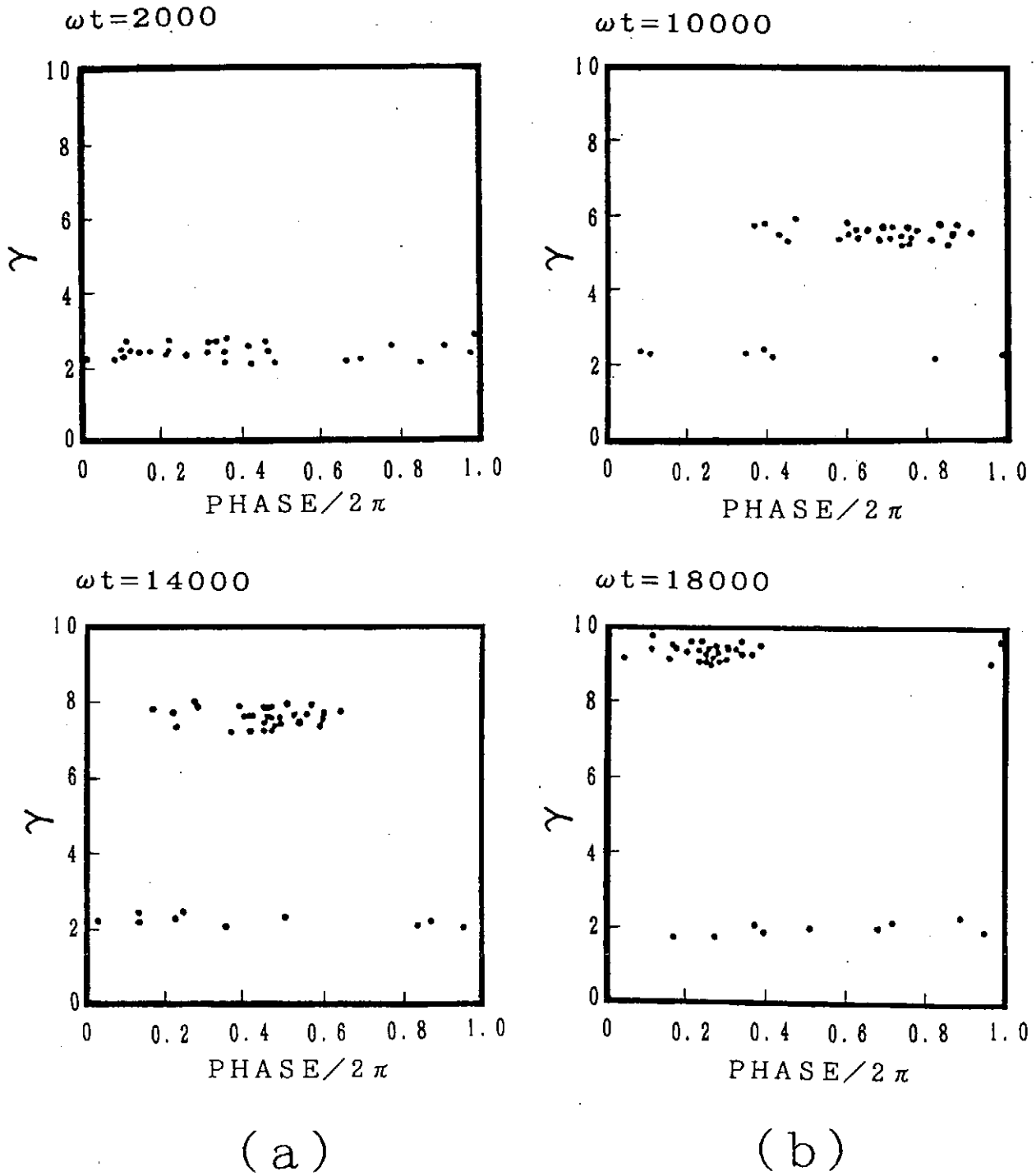
ωt=2000
ωt=10000
ωt=14000
ωt=18000
γ
PHASE／2π
0
0.2
0.4
0.6
0.8
1.0
2
4
6
8
10
(a)
(b)

Fig. 9

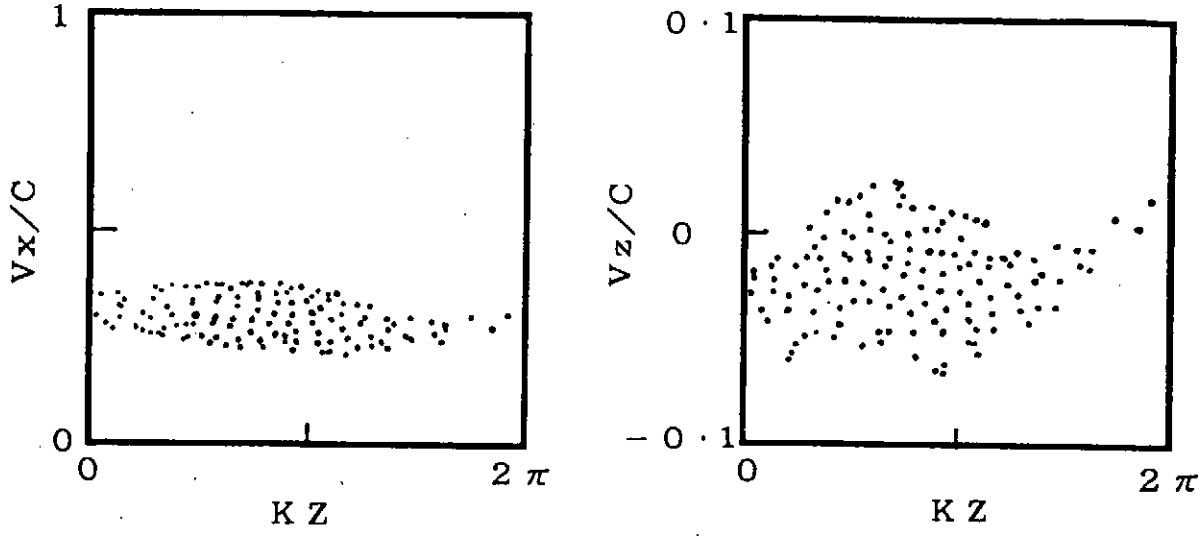
1
0
Vx/C
0
2 π
K Z
0 · 1
0
− 0 · 1
Vz/C
0
2 π
K Z
ω T γ p = 6 5 0

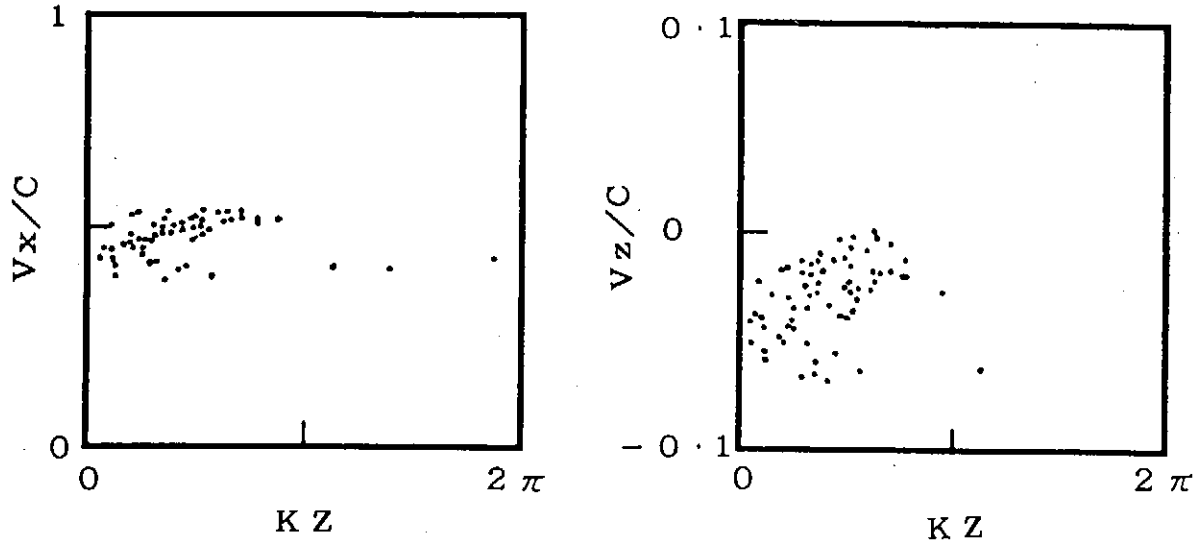
1
0
Vx/C
0
2 π
K Z
0 · 1
0
− 0 · 1
Vz/C
0
2 π
K Z
ω T γ p = 9 9 7

(a) (b)

Fig. 10

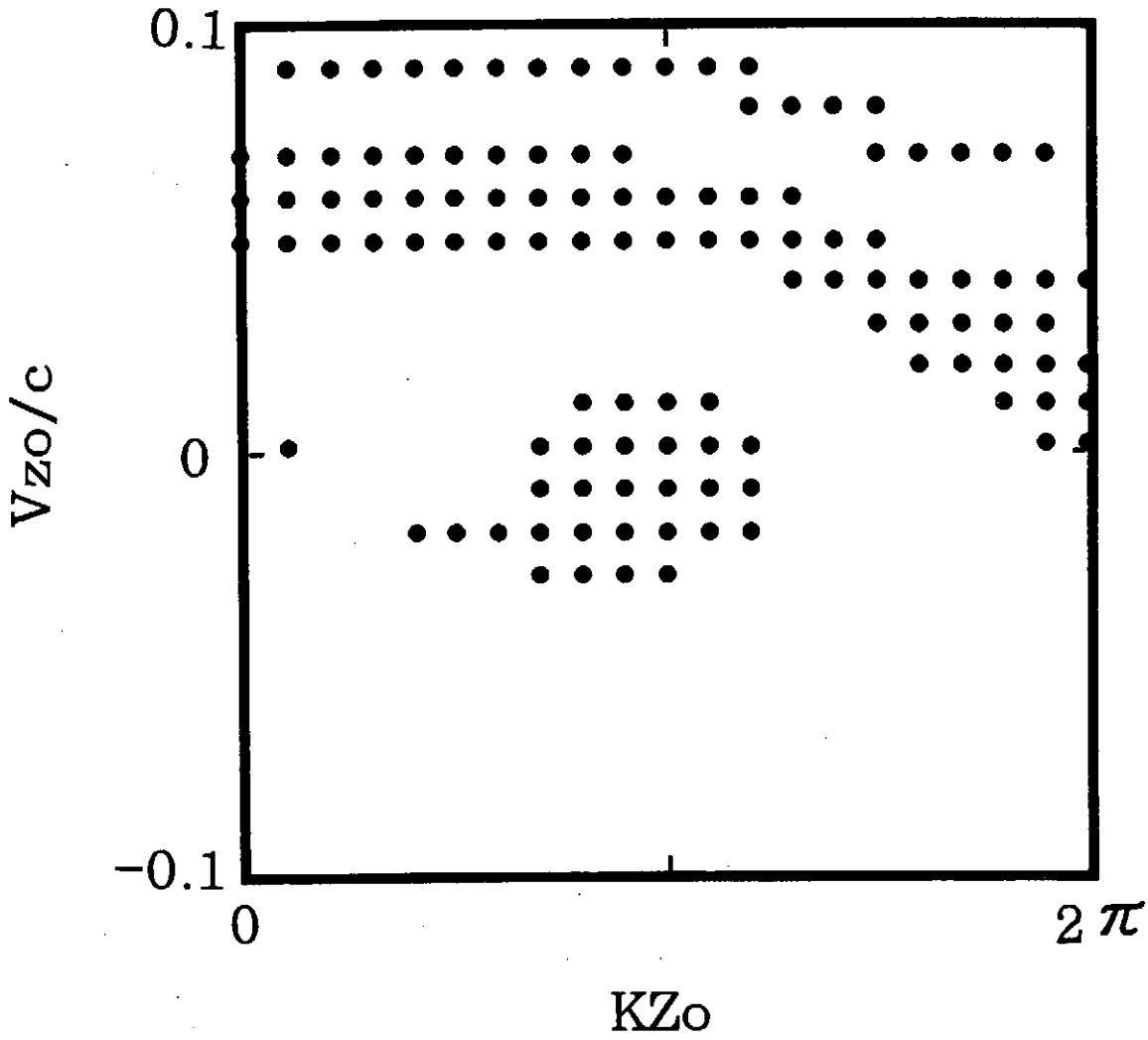

Fig. 11 (a)

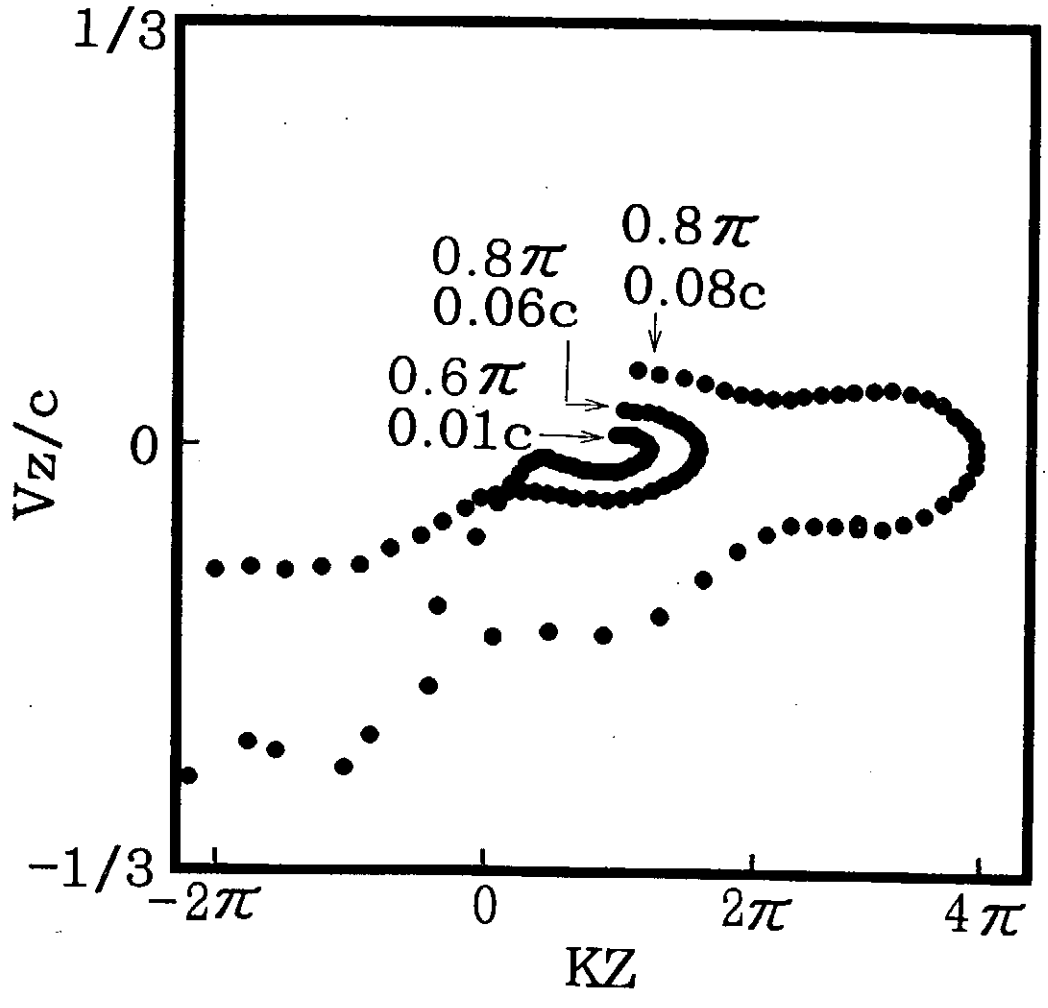

Fig. 11 (b)

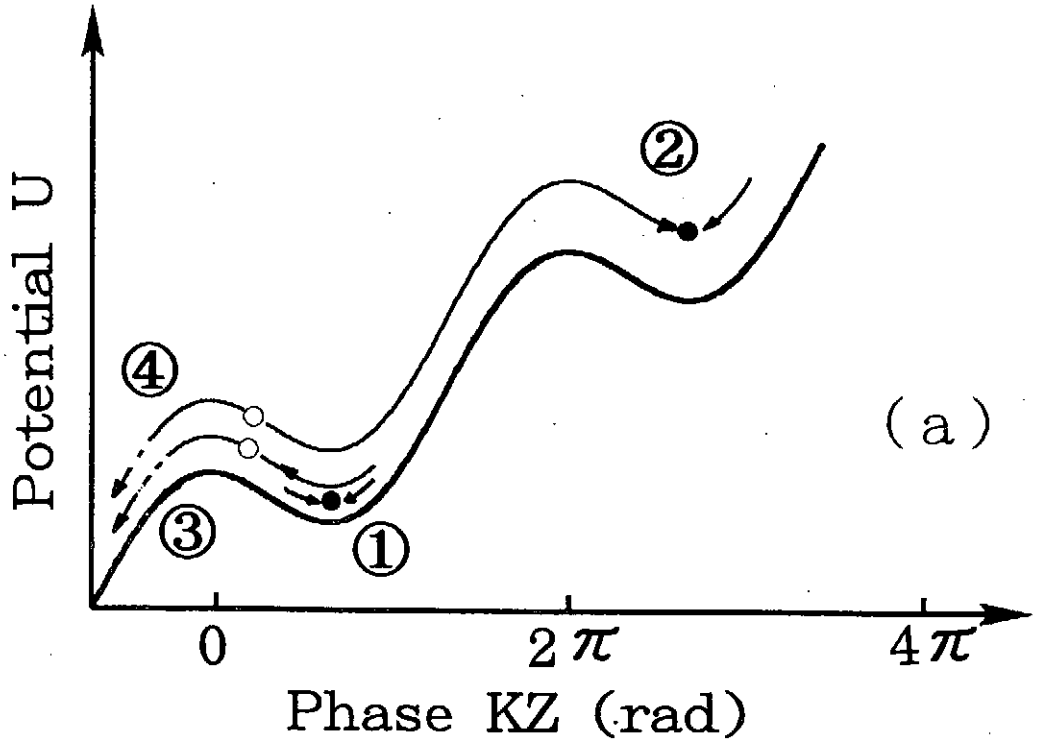
Potential U
②
④
③
①
(a)
0
2π
4π
Phase KZ (rad)

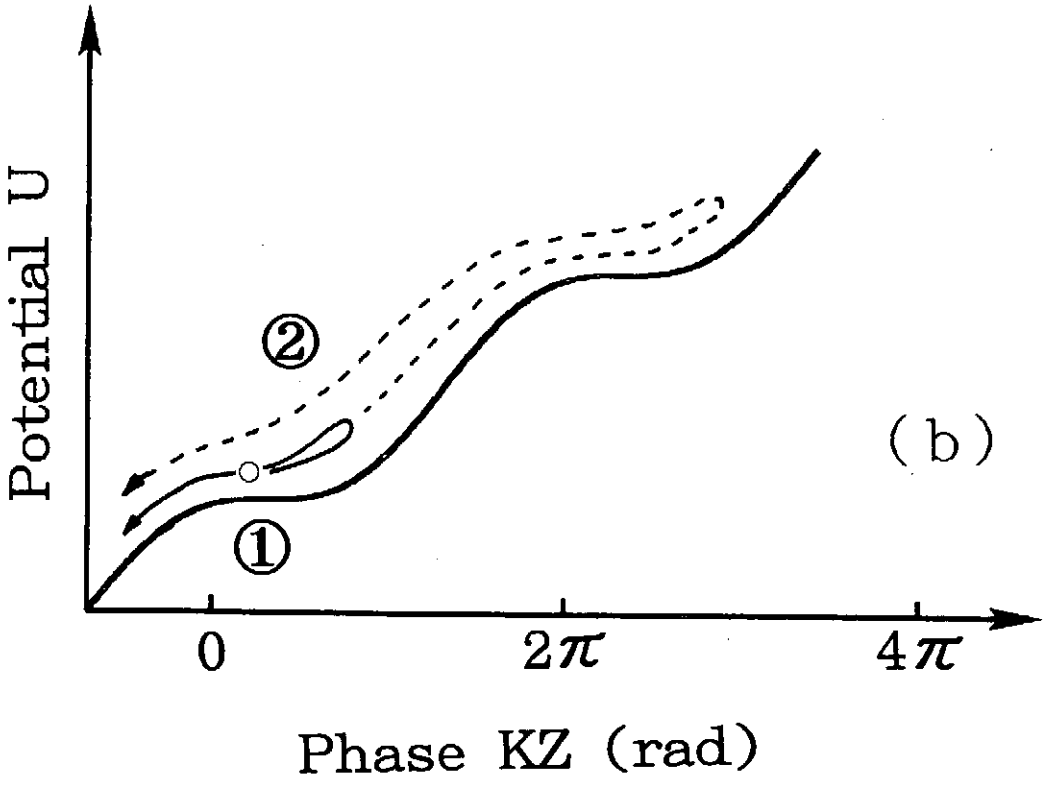
Potential U
②
①
(b)
0
2π
4π
Phase KZ (rad)

Fig. 12

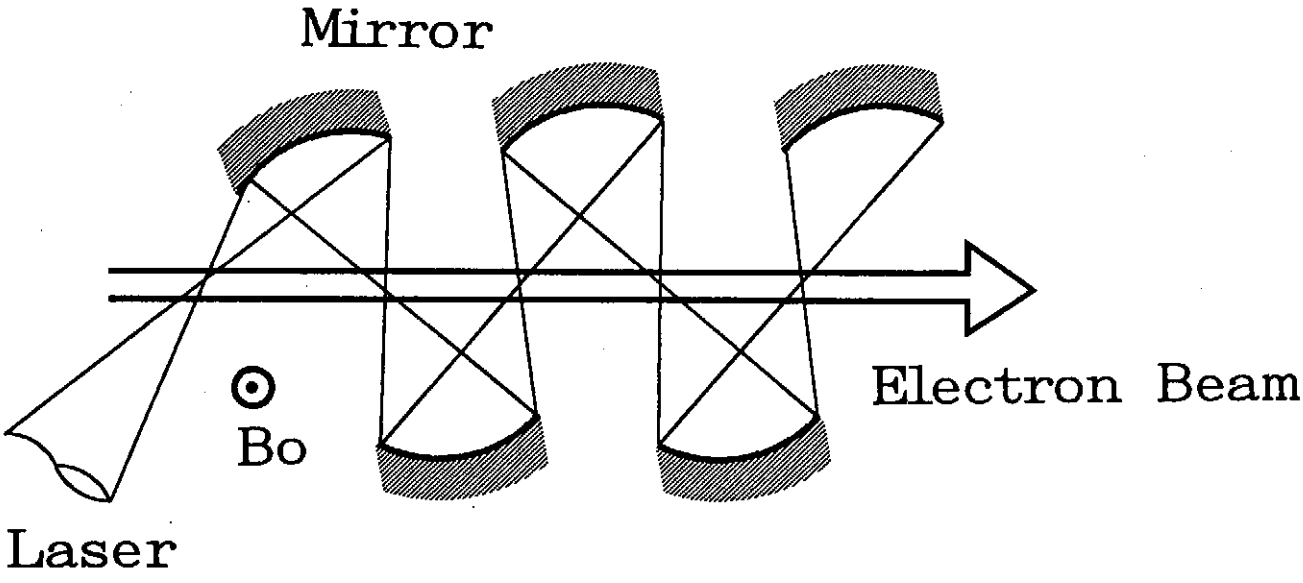

Fig. 13

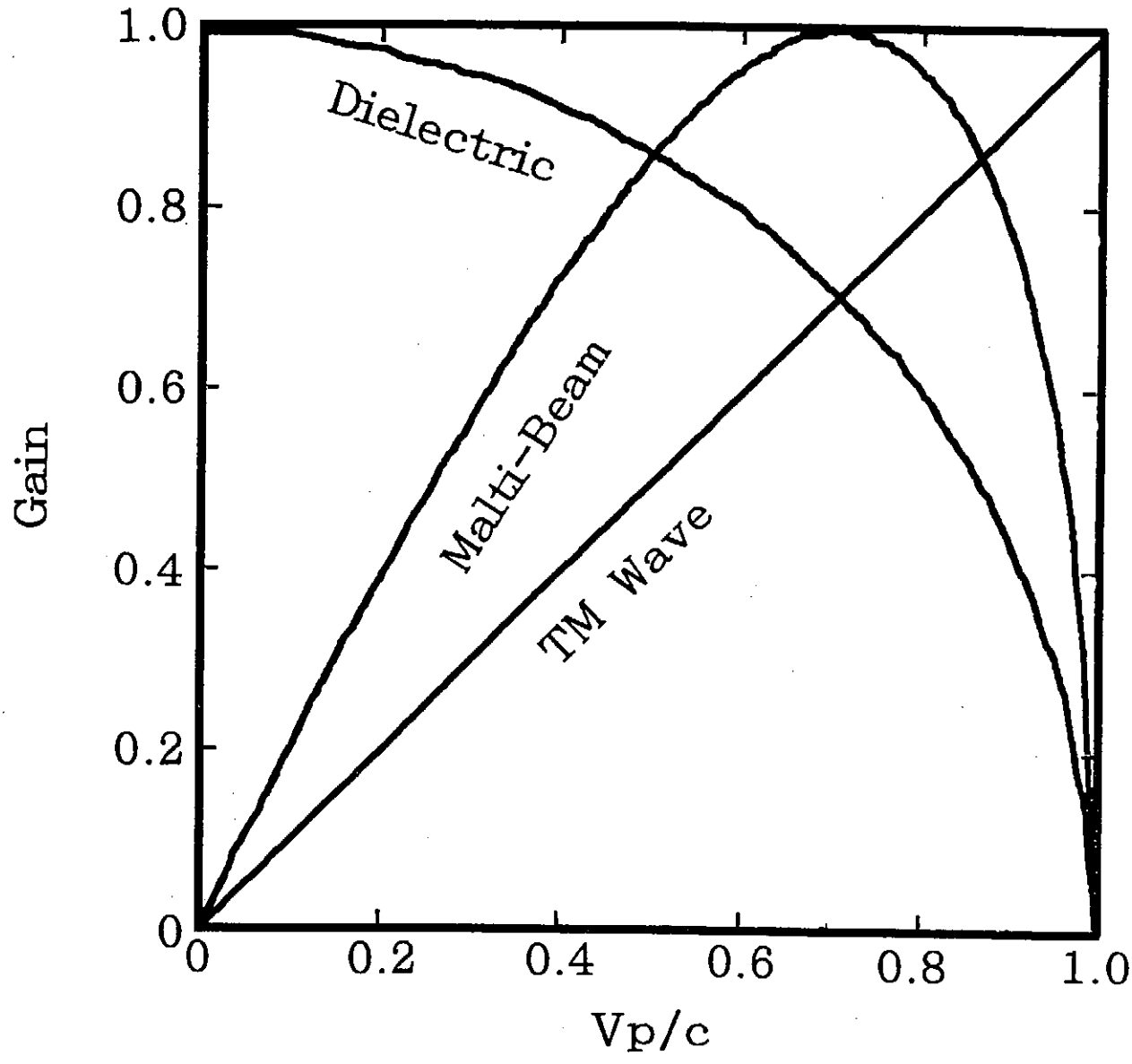
1.0
0.8
0.6
0.4
0.2
0
Gain
Dielectric
Malti-Beam
TM Wave
0
0.2
0.4
0.6
0.8
1.0
Vp/c

Fig. 14

Table 1.

	Ex(MV/m)	Ez(MV/m)	By(G)	Bo(G)	△z(m)	△x(m)
multi-EM beam	1		33.3	37.4	302	109
TE mode with dielectrics	1		35.4	4.10	2770	997
VpxB accelerator		1		99.2	114	40.8
Conventional linear accelerator		1		0	999	0

Electron Acceleration by Gaussian Laser Beam

Satosi Takeuchi, Ryo Sugihara† and Koichi Shimoda‡

Faculty of Engineering, Yamanashi University, Kofu 400, Japan
†Plasma Science Center, Nagoya University, Nagoya 464-01, Japan
‡Faculty of Science and Technology, Keio University, Yokohama 223, Japan

Abstract

It is shown that the longitudinal electric field of a transverse magnetic mode of a Gaussian laser beam accelerates an electron to an ultrarelativistic energy. The electron is captured and accelerated in a length of the order of the Rayleigh range. The ultimate energy increment of the electron with a single laser beam is given by the product of transverse field intensity and the beam waist, and can be of the order of 100MeV. This fact implies that a multi-stage acceleration enables TeV-order-acceleration in a length of a few kilometers with the art.

1 Introduction

The energy density of a laser pulse is usually much greater than that of microwave, and hence many ideas for using powerful lasers to accelerate electrons have been published.[1–3] Since, however, the laser beam is essentially a transverse electromagnetic wave, directions of acceleration in those schemes are transverse and this gives rise to complexity of configurations.

It has been noticed, on the other hand, that the Gaussian beam has a longitudinal field component $E_z(x, y, z)$.[4] Since E_z is connected with the transverse field component $\mathbf{E}_t(x, y, z)$ through $\nabla \cdot \mathbf{E} = 0$, E_z is formally given by

$$E_z = -\int \nabla_t \cdot \mathbf{E}_t dz, \tag{1}$$

where ∇_t stands for the transverse part of the divergence operator ∇.

Cicchiteilli et. al.[5] ascribed to this field the high energy electron ejection from laser irradiated materials and Scully[6] and Caspers[7] gave qualitative discussions on the possibility of using this field for accelerating electrons. On the other hand, Shimoda[8] gave an elementary

methode for calculating field components of a laser beam with finite width and explicitly acquired the longitudinal field. Accordingly we expected an electron acceleration with this longitudinal field and obtained a concrete expression of electron energy gain. We also found that the acceleration mechanism is relevant to the beat wave accelerator[9] rather than to the linear accelerator because of the presence of a phase slippage.

2 Gaussian beam

We start with reviewing the methode of Ref.8 and obtaining the required longitudinal field component. Suppose that a TM wave whose frequensy ω and wave number k is propagating in the z-direction in free space with the fields,

$$(B_x, B_y, B_z) = [f(x,y,z), g(x,y,z), 0]\exp(i\omega t - ikz). \tag{2}$$

It is shown that f and g satisfy the following Helmholtz equation,

$$\frac{\partial^2 u}{\partial x^2} + \frac{\partial^2 u}{\partial y^2} - 2ik\frac{\partial u}{\partial z} = 0, \tag{3}$$

under the paraxial approximation $|\partial^2 u/\partial z^2| \ll |2k\partial u/\partial z|$ where u stands for f or g. The Gaussian-type solution is written in the form[10],

$$u = \frac{w_0}{w} H_m\left(\sqrt{2}\frac{x}{w}\right) H_n\left(\sqrt{2}\frac{y}{w}\right) \exp(i\Phi_{m,n})\exp\left(-\frac{r^2}{w^2} - \frac{ikr^2}{2R}\right), \tag{4}$$

where $r^2 = x^2 + y^2$, $\Phi_{m,n} = (m+n+1)\tan^{-1}(z/\ell_0)$, $F^{-1} = 1/w^2(z) + ik/2R(z)$, $w(z) = w_0\sqrt{1 + z^2/\ell_0^2}$, $R(z) = z + \ell_0^2/z$, $\ell_0 = \pi w_0^2/\lambda$, and H_m and H_n are the Hermite polynomials. The ℓ_0 is the Rayleigh range, w_0 is the beam radius at the waist and other notations are standard.

We choose $f = u_{mn}$ and then have $g = -\int(\partial u_{mn}/\partial x)dy$, using the relation $\partial f/\partial x + \partial g/\partial y = 0$ from $\nabla \cdot \mathbf{B} = 0$. The best mode for electron acceleration is the one with $m = 0$ and $n = 1$ or vice versa. We understand this from the following argument. The E_z is easily obtained to be

$$E_z = -i\frac{2Aw_0}{kw^2}\left(1 - \frac{r^2}{F}\right)\exp(i\omega t - ikz + i\Phi_{0,1})\exp\left(-\frac{r^2}{F}\right) \tag{5}$$

where we introduced an amplitude A which relates to the maximum amplitude of the transverse electric field given by the relation $A = \sqrt{2}e|E|_{max} = 2.33|E|_{max}$ where $|E|_{max} = \max(\sqrt{|E_x|^2 + |E_y|^2})$.

In the vicinity of the beam axis, i.e., $r \approx 0$, the approximations $f \approx g \approx 0$ are valid, then the transverse components of the field are given by $E_x = B_y \approx 0$, $E_y = -B_x \approx 0$.

Whereas E_z takes the maximum value. These properties are appropriate for acceleration. We see the mode considered is symmetric around the beam axis and therefore we call it TM_0 mode.

3 Acceleration mechanism

We suppose that a relativistic test electron is injected from the left-hand side and directed to the right; the direction is the same as the laser beam. Since the transverse field on the axis is zero, we only focus our attention on interaction with the longitudinal field, $\bar{E}_z = Re(E_z)$, at $x = y = 0$. With $\zeta \equiv z/\ell_0$, $w^2 = w_0^2(1+\zeta^2)$ and familiar relations, $\sin(2\tan^{-1}\zeta) = 2\zeta/(1+\zeta^2)$, and $\cos(2\tan^{-1}\zeta) = (1-\zeta^2)/(1+\zeta^2)$, we have

$$\bar{E}_z(\psi) = \frac{2A}{kw_0}\left[\frac{2\zeta\cos\psi}{(1+\zeta^2)^2} + \frac{(1-\zeta^2)\sin\psi}{(1+\zeta^2)^2}\right], \tag{6}$$

where $\psi = \omega t - kz + \psi_0$, ψ_0 being the phase of a particle to start at $z = -\ell_0$, which is the case through the text. We assume the injected electron has a large γ, e.g., 10^3, and then we may approximate ψ by

$$\psi \approx \psi_0 + k\ell_0(\zeta+1)/2\gamma^2 \approx \psi_0, \tag{7}$$

where we have used $t \approx (z+\ell_0)/v_z$ and $(1-\beta_z) \approx 1/2\gamma^2$. Relation (7) implies that for the accelerating electron, ψ is nearly locked at the initial phase ψ_0. This fact is already known in the electron linear accelerator in which a longitudinal electromagnetic wave with the velocity of light c is used. We must, however, note that the actual phase is $\psi + \Phi_{01}$ as seen in expression (5) and this point will be discussed later on.

Now assuming that γ is large enough, we replace ψ in eq.(6) by ψ_0 and then we easily see the motion of electron is governed by the following energy conservation relation

$$mc^2\gamma + U(\zeta) = mc^2\gamma_0 + U(\zeta_0) \equiv K_0, \tag{8}$$

$$U(\zeta) \equiv -\int_{-1}^{\zeta} q\bar{E}_z(\zeta)\ell_0 d\zeta, \tag{9}$$

$$= -qAw_0(\zeta\sin\psi_0 - \cos\psi_0)/(1+\zeta^2). \tag{10}$$

Figure 1 shows a typical profile of $U(\zeta)$. The $U(\zeta)$ has two extremums $U^+ \equiv U(\zeta^+)$ and $U^- \equiv U(\zeta^-)$ which are given by

$$U^{\pm} = (qAw_0/2)(\mp 1 + \cos\psi_0), \tag{11}$$

$$\zeta^{\pm} = (\pm 1 + \cos\psi_0)/\sin\psi_0. \tag{12}$$

The U^+ and U^- are the minimum and the maximum, respectively, irrespective of the sign of $\sin\psi_0$. When the initial energy K_0 of the electron is greater than $U(\zeta^-)$, the particle can run over the maximum at $\zeta = \zeta^-$ even if $\zeta_0 < \zeta^-$ and the energy gain is expressed as

$$mc^2\Delta\gamma = U(\zeta_0) - U(\zeta). \tag{13}$$

The energy gain between $\zeta = 1$ and $\zeta_0 = -1$, or in the Rayleigh range, is given by

$$mc^2\Delta\gamma = U(-1) - U(1) = qAw_0 \sin\psi_0. \tag{14}$$

We understand that the maximum energy gain is achieved when $\sin\psi_0 = 1$. We see, in this case, $\zeta^+ = 1$ and $\zeta^- = -1$, which coincide with the both ends of the Rayleigh range, and there the potential takes its minimum and maximum. For $\sin\psi_0 < 0$, the electron is decelerated as is seen from Eq.(14).

4 Longitudinal phase stability

The phase locking between the electron and the longitudinal field is a sufficient condition for a continuous acceleration in the full Rayleigh range. Figure 2 gives critical γ_0, γ_p, to the phase-lock approximation for $\sin\psi_0 = 1$ and for various kw_0. Above the curve the difference between the numerical value $(\Delta\gamma)_{num}$ obtained by using the exact $\bar{E}_z(\psi)$ and the analytical value $(\Delta\gamma)_{an}$ of Eq.(14) is less than 1%. The γ_p levels off for small amplitude A as seen in the figure. This is because the test electron just passes through the Rayleigh range with little interaction with the field having such a small amplitude. We can estimate γ_p in this limit analytically and have $\gamma_p = kw_0(\pi - 2)^{1/2}/(2\sqrt{2\varepsilon})$ which agrees with the numerical one, where $\varepsilon = |1 - (\Delta\gamma)_{an}/(\Delta\gamma)_{num}|$. Dotted lines in the figure show analytical results.

We consider the matching between the particle and the wave. The phase velocity v_p is obtained from relation $\omega t - kz + \Phi_{01}$ =constant as

$$v_p = \frac{c}{1 - 2\ell_0/k(z^2 + \ell_0^2)} \approx c\left[1 + \frac{2}{k\ell_0(1+\zeta^2)}\right]. \tag{15}$$

Obviously v_p is greater than c and then the accelerating particle sooner or later falls down into the deceleration phase. To be precise, we notice that $2\tan^{-1}(1) = \pi/2$ and $2\tan^{-1}(-1) = -\pi/2$ and then from Eq.(7) the phase $\omega t - kz + \Phi_{01} \approx \Phi_{01}$ differs by π between $\zeta_0 = -1$ and $\zeta = 1$ or between the initial and the final phases. This means that the particle is accelerated in the half wave length. In this sense the acceleration scheme presented here is essentially different from the usual electron linear accelerator in which electrons can be accelerated indefinitely.

5 Tansverse stability

So far we have assumed that the test electron runs along the beam axis on the center. Consequently the particle is not affected by the transverse field because B_x and B_y are zero on the axis and so E_x and E_y. When the particle is injected off the axis, however, it may be deflected by the transverse fields. We then examine the stability of particle orbit. We deal with the motion on the $x-z$ plane, since the laser beam of TM_0 mode is symmetric around the axis. We inject the test particle at the point $(w_0/\sqrt{2}, 0, -\ell_0)$, bearing in mind that $|E_x|$ takes its maximum at $(w_0/\sqrt{2}, 0, 0)$. The x component of the force, F_x, affecting the electron is

$$F_x = qE_x - (q/c)B_y v_z \approx qE_x/(2\gamma^2). \tag{16}$$

A similar force $qE_y/(2\gamma^2)$ acts on the electron on the $y-z$ plane. We examine the orbit for $\sin\psi_0 = 1$ for which the particle is continuously accelerated. If the electron is not deflected immediately after the injection, there occurs no deflection afterwards since $\gamma > \gamma_0$ and since $|F_x|$ rapidly decreases. Suppose that we reduce γ_0 and that for some γ_0, say γ_d, the electron starts to be deflected near $\zeta_0 = -1$. We call γ_d the marginal γ_0 that divides the motion into the stable and the unstable ones. The γ_d is given in Fig.3 together with the filed E_x in the inlet. Each curve has its maximum. This is caused by a property of F_x in Eq.(16). That is, for a small A, F_x is proportional to E_x or A, while for a large A, F_x is inversely proportional to A. Now we understand that if we use a laser with a kw_0 an electron whose γ_0 is above both curves labeled with the same kw_0 in Fig.2 and in Fig.3 is stably accelerated.

6 Discussion

We show here some examples of electron acceleration. Suppose that $\gamma_0 = 10^3$ (510MeV of the electron) which safely clears the above criterions irrespective of kw_0 and that $\lambda = 10^{-3}$cm (CO_2 laser). The maximum energy gain $G_{max} \equiv mc^2(\Delta\gamma)_{max}$ of the electron is given by Eq.(14) with $\sin\psi_0 = 1$. The A relates to $|E|_{max}$ as indicated previously and then we easily obtain G_{max} in terms of $|E|_{max}$. We here express G_{max} in term of the power P of the beam as follows:

$$G_{max} = 0.64 \times 10^2 \left[P(\mathrm{W/cm^2}) w_0^2(\mathrm{cm})\right]^{1/2} \mathrm{eV}. \tag{17}$$

We now note that $P \times \pi w_0^2$ is constant provided the total power is fixed. This implies that G_{max} is constant in this constraint no matter how we control w_0, while the acceleration length $R_a \equiv |\zeta^- - \zeta^+| = 2\ell_0 = kw_0^2$ is reduced if we have a stronger focus. We now choose $P = 10^{14}$ W/cm^2, a realistic value in view of the present state of the art in laser technology, and $w_0 = 0.1$ cm. Then we have $G_{max} = 6.4 \times 10^7$eV and $R_a = 63$cm. If we use the those

values, we will have 1TeV electrons in a 10 km long device that is made of 16×10^3 units of the acceleration element with 63cm long. With the same power and with $w_0 = 0.033$cm, the R_a reduces to 6.3cm and the total length of the 1TeV accelerator will be reduced to 1km though the focused electric field will increase to 10^9V/cm, still within the present state of the art of laser technology.

A schematic diagram of an experiment to verify the acceleration mechanism presented here is shown in Fig.4.

7 Conclusion

We have proposed a new scheme of electron acceleration by using the longitudinal field accompanying a laser of finite width. We first derive analytically Hermite-Gaussian laser beams by using the paraxial approximation. The field components properly include a longitudinal electric field whose intensity is maximum at the beam axis while the transverse components become zero there. A test electron is phase-locked and stably accelerated when $\gamma_0 > \gamma_p$ which corresponds to the minimum injection energy and also when $\gamma_0 > \gamma_d$ above which the deflection by E_x and E_y is negligible. It is shown that the maximum energy increment is independent of the injection energy of a particle and is given by qAw_0. A numerical demonstration for applying this scheme to an accelerator is made and we find that it is plausible to have an 1TeV electron accelerator with a few kilometers length by the use of lasers of the present state of the art.

Acknowledgment

One of the authors (S.T.) would like to thank Professors M.Matsumoto and K.Sakai for their enlightening discussions and invaluable comments. This work was supported by Grant-in-Aid for Encouragement of Young Scientists of The Ministry of Education, Science and Culture in Japan.

References

[1] *Advanced Accelerator Concepts*, AIP Conference Proceedings No.156, edited by F.E.Mills (AIP, New York, 1987).

[2] *Advanced Accelerator Concepts*, AIP Conference Proceedings No.193, edited by C.Joshi (AIP, New York, 1989).

[3] W.Scheid and H.Hora: Laser and Particle Beams, **7** (1989) 315.

[4] M.Lax, W.H.Luisell and W.B.McKnight: Phys. Rev. A, **11** (1975) 1365.

[5] L.Cicchitelli, H.Hora and R.Postel: Phys. Rev. A, **41** (1990) 3727.

[6] M.O.Scully: Appl. Phys. **B51** (1990) 238.

[7] F.Caspers and E.Jensen: *Laser Interaction and Related Plasma Phenomena*, ed. H.Hora and G.H.Miley (Plenum Press, New York) Vol.9, p.459.

[8] K.Shimoda: J. Phys. Soc. Jpn. **60** (1991) 141; ibid. 1432.

[9] T.Tajima and J.M.Dawson: Phys. Rev. Lett. **43** (1979) 267.

[10] H.Kogelnik and T.Li: Proc. IEEE, **54** (1966) 1312.

Figure captions

Fig.1 Typical profile of the potential $U(\zeta)$.

Fig.2 Initial value γ_p of the particle vs the transverse amplitude A of the electromagnetic wave.
The value γ_p is the critical γ_0 for the phase locking. In the region above a curve the phase locking approximation is valid, then the electron is kept in phase. The difference of the energy gain between the numerical value and the analytical one (14) with $\sin\psi_0 = 1$ is less than 1%.

Fig.3 Marginal value $\gamma_d \equiv \gamma_0$ for the orbit stability and equi-intensity curve of E_x for $\sin\psi_0 = \pm 1$.
The transverse motion of the particle is stable in the region above the curves. In the inlet the direction of E_x on the solid curves is outwards while that on the dotted curves is inwards when $\sin\psi_0 = 1$. When $\sin\psi_0 = -1$, the direction of E_x is reversed.

Fig.4 Schematic diagram of experimental arrangement for verification of the principle of electron acceleration by the Gaussian laser beam.

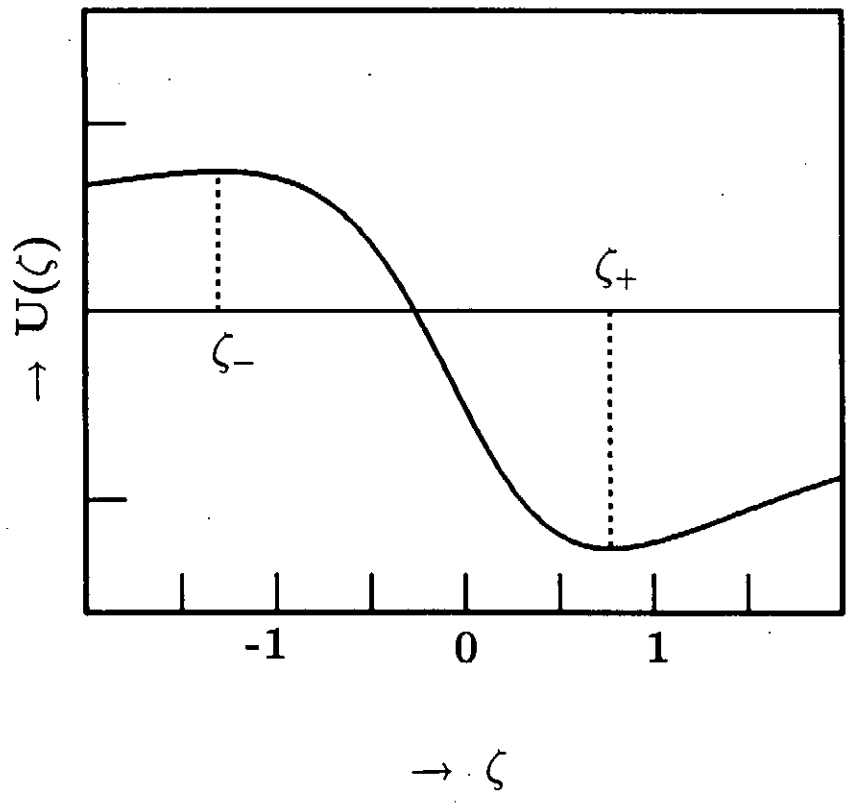

Fig.1

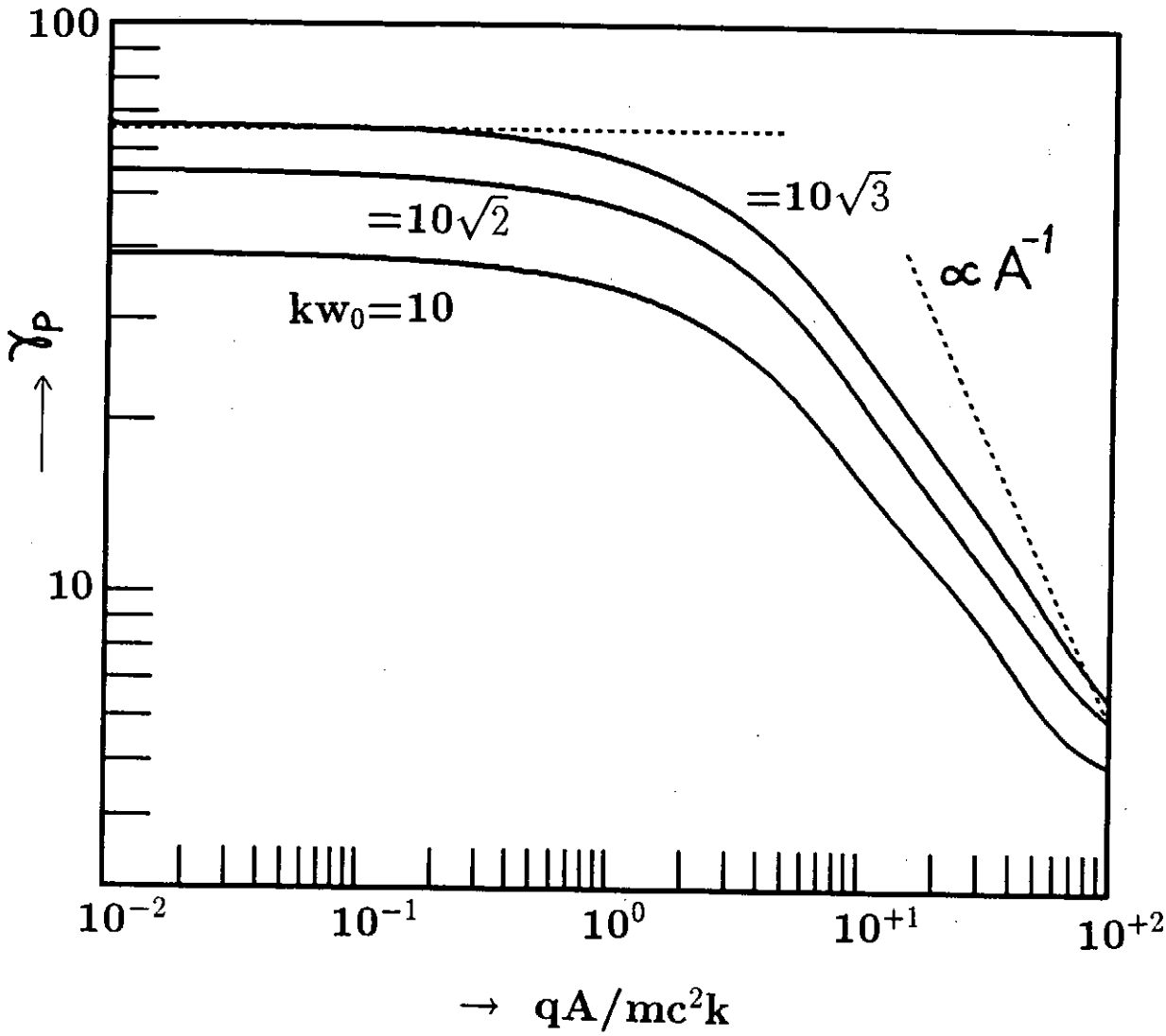
100
10
γ_p
$=10\sqrt{3}$
$=10\sqrt{2}$
$kw_0=10$
$\propto A^{-1}$
10^{-2}
10^{-1}
10^{0}
10^{+1}
10^{+2}
$\rightarrow$ qA/mc^2k

Fig.2

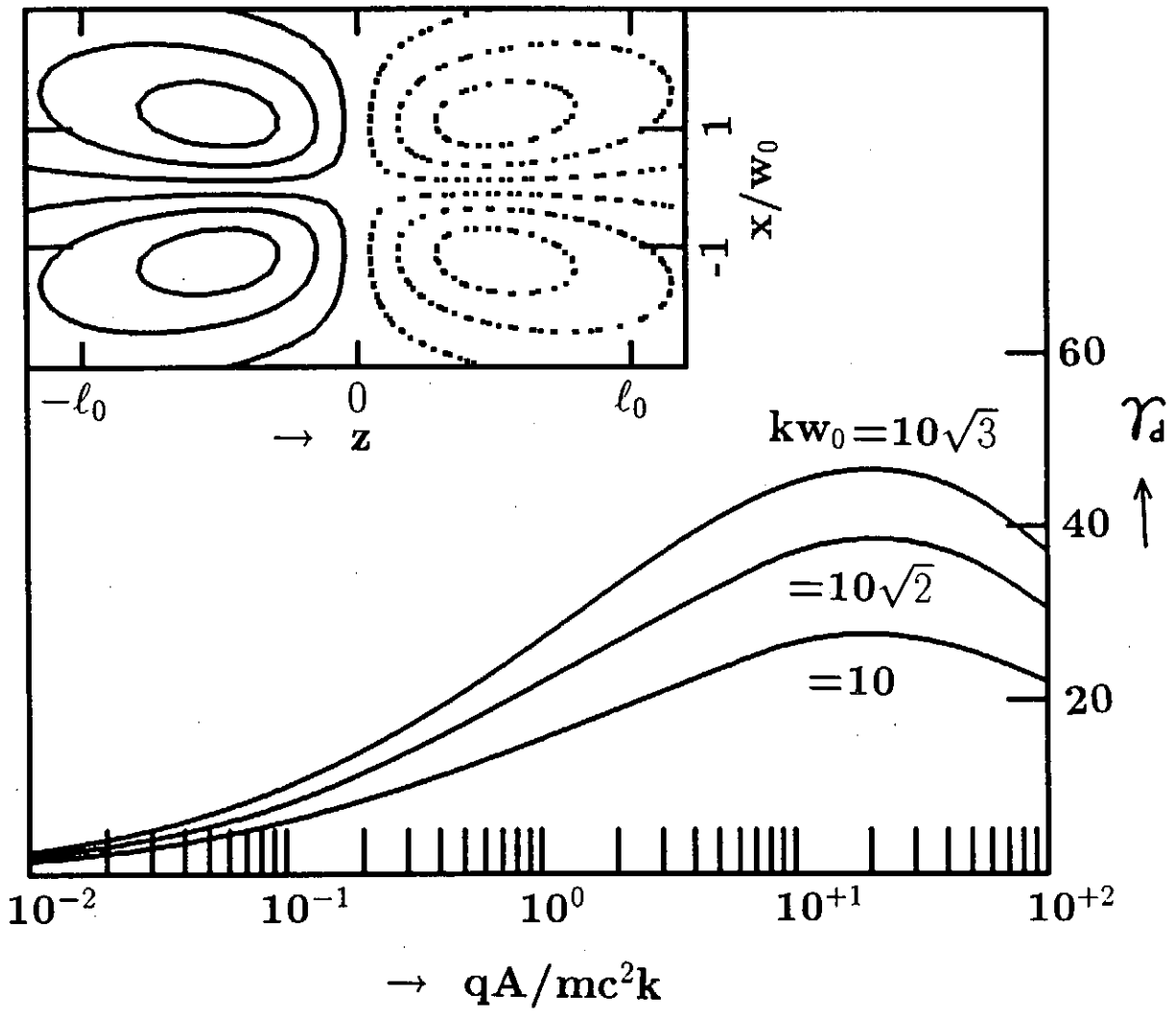
1
-1
x/w0
−ℓ0
0
ℓ0
→ z
60
40
20
γd
kw0=10√3
=10√2
=10
10−2
10−1
100
10+1
10+2
→ qA/mc2k

Fig.3

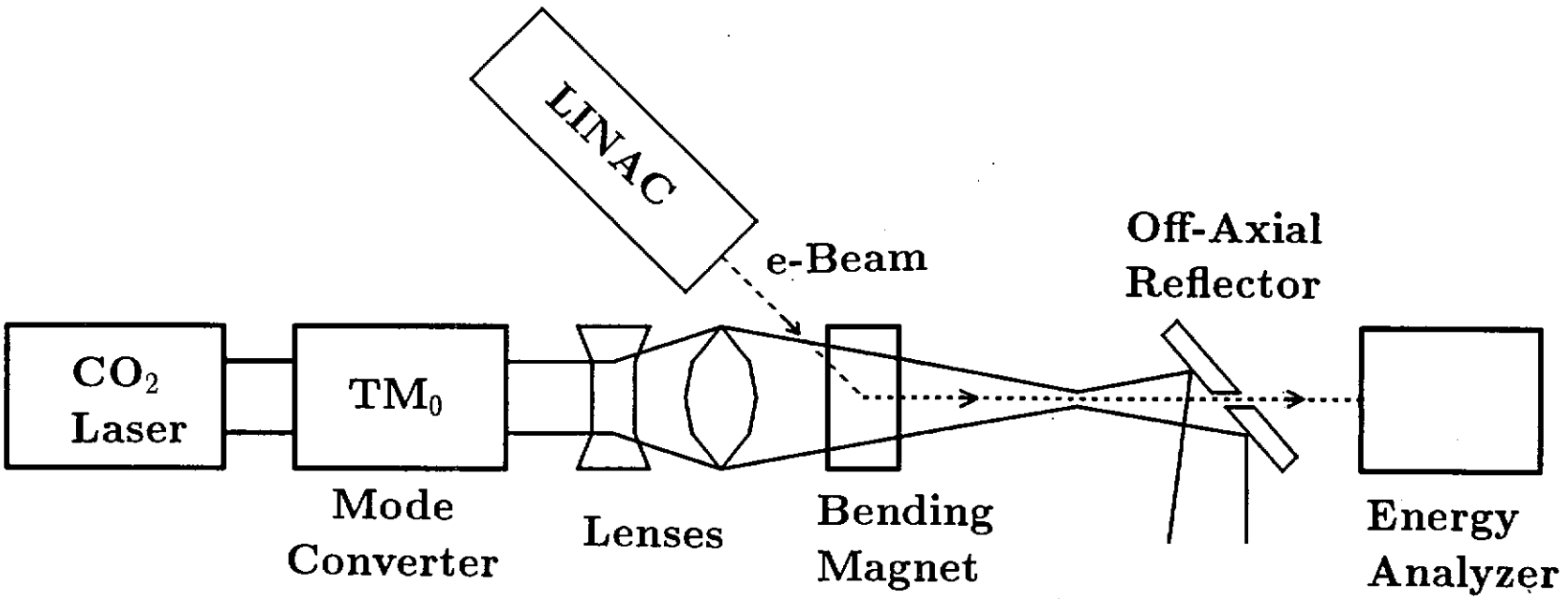
LINAC
e-Beam
Off-Axial
Reflector
CO_2
Laser
TM_0
Mode
Converter
Lenses
Bending
Magnet
Energy
Analyzer

Fig.4

EXCITATION OF PLASMA WAVE BY A SHORT MICROWAVE PULSE

S.Kusaka, A.Saitoh, N.Yugami, and Y.Nishida

Department of Electrical and Electronic Engineering

Utsunomiya University

Utsunomiya, Tochigi 321, Japan

Abstract

The excitation of the plasma wakefield can be achieved by using short, high-power microwave pulse, instead of a laser pulse for demonstrating the laser wakefield accelerator (LWFA). Although the conditions of the experiment are different from those of the LWFA, the plasma wave is observed, which is non-resonantly excited by short microwave pulse. Modifying the original theory, the excitation of the plasma wave is due to the ponderomotive force ($gradE^2$) of the short microwave pulse.

Several electron acceleration schemes using plasma have been proposed.[1-5] They have an advantage of getting high field gradient for electron acceleration. Laser wakefield accelerator (LWFA) is one of the plasma-based acceleration schemes, and employs a short, high-power, single frequency laser pulse.[5-6] The LWFA has some advantages. For example, it can get long

acceleration distance, or it is not necessary to adjust the plasma density very precisely to designed certain value.

In this paper, first experimental results by a short microwave pulse, and some explanations for the excitation mechanism of the plasma wave are presented. This is essentially the same method of the LWFA.

The ponderomotive force produced by the microwave acting on the plasma is given by

$$\vec{F}_{pond}=|e|\nabla\phi_L(r,Z,t) \qquad (1)$$

where, $\phi_L=-m_0c^2a_L^2/(2|e|)$, is ponderomotive potential and $a_L=|e|A_L/(m_0c^2)$ is the normalized vector potential amplitude of radiation field. This field moves at the wave group velocity. The radial ponderomotive force expels electrons radially outward, while the front (back) of the laser pulse exerts a forward (backward) force on the electron. The microwave pulse acts like an electron bunch which propagates through the plasma. As the plasma electrons flow around the microwave pulse, the plasma waves are generated. (Fig.1)

The wave equation for the plasma wake field is given as,

$$\frac{\partial^2\phi}{\partial t^2}+\omega_p^2\phi=-\omega_p^2\phi_L . \qquad (2)$$

By performing an algebraic transformation to the phase velocity frame of excited plasma wave, ($\zeta=Z-v_pt$, $\tau=t$), one can obtain from eq.(2),

$$\frac{\partial^2\phi}{\partial\zeta^2}+k_p^2\phi=-k_p^2\phi_L \qquad (3)$$

where $k_p=\omega_p/v_p$. By solving eq.(3), one can obtains

$$\phi(r,\zeta)=k_p\int_{\zeta}^{\infty}\sin k_p(\zeta-\zeta')\,\phi_L(r,\zeta')d\zeta' , \qquad (4)$$

and the electric field of the wakefield is given by $E_z=-\delta\phi/\delta Z$, $E_r=-\delta\phi/\delta r$.

Experiments are performed in a cylindrical stainless steel chamber with multi-dipole magnets on the outside of the wall, as shown in Fig.2. The argon plasma is produced by pulse discharge (discharge duration of 3 msec and 10 Hz repetition). Typical plasma parameters are a maximum plasma density $n_0=2\times10^{11}cm^{-3}$, an electron temperature T_e=2-3 eV, which are obtained by Langmuir probe method. The p-polarized microwave with a frequency 2.86 GHz (corresponding critical plasma-density is $n_c=1\times10^{11}cm^{-3}$), a maximum power of 10 kW and typical pulse width 500 nsec is irradiated through a high gain horn antenna installed with metal plate lens in front of it. The field strength in the plasma are measured by a crystal detector or a spectrum analyzer, through a tiny plate probe (1 mm x 1 mm) or a cylindrical probe (0.1 mm x 1 mm).

To demonstrate the excitation of the wakefield, a uniform plasma density and no reflected microwave are required. Unfortunately, in our experimental apparatus, such conditions can't be achieved. However, the physical mechanism and other characteristics of the wave excitation can be investigated under these conditions.

Figure.3 indicates two detected waveforms, top trace is the signal of the incident microwave, and bottom one is the field of the excited plasma wave detected by the crystal detector at Z=25 cm measured from the antenna edge. The scale of the horizontal axis is 100 ns/div. There are two peaks in the plasma wave .

The latter peak seems to be wakefield, because it is nonlinearly excited after the incident microwave power shut off. This phenomena can be explained by the above mentioned theory. Figure.4 shows the $|E^2$-distribution in the Z-direction, in other words, the standing wave structure is seen. Figures.5(a) and (b) show spectra of the plasma wave observed around 1 GHz with and without plasma at Z=25 cm respectively. As clearly seen, the plasma wave can be excited with the frequency of about 1 GHz. When a plasma frequency is 1 GHz, the corresponding plasma density is 1.2×10^{10} cm^{-3}. This value is in reasonable agreement with $n_0\simeq1.3\times10^{10}$ cm^{-3} which is measured by Langmuir probe method. Figure.6 shows the propagation velocity (Z-direction) of the nonlinear wave (the latter peak) shown in Fig.3, the velocity of which was measured to be $v=2-3\times10^7$ cm/s. Since the electron thermal velocity is estimated to be $v_{th}\simeq1\times10^8$ cm/s, the velocity of this nonlinear wave is slightly slower than v_{th}. The present pulse propagates toward the point of Z=25 cm. This point corresponds to the bottom of the standing wave, as seen in Fig.4. The waves are excited at both sides of the bottom, where the ponderomotive force, which is proportional to $\mathrm{grad}E^2$, is maximum.

To explain above experimental results, the theory mentioned previously should be modified. As shown in Fig.7, the following conditions are required; the electron temperature T_e is non-zero, and the group velocity of the driving wave is zero, because the short pulse, electromagnetic wave is a standing wave and does not propagate. Still there exist areas of high gradient of E^2. Therefore, even if the microwave pulse does not pass through the plasma, the ponderomotive force originated from high gradient of

E^2 can exist. So that it is possible to consider that the ponderomotive force acts on electrons, and the plasma wave can be excited. Under these assumptions, the excited plasma wave is expected to propagate with velocity less than thermal velocity v_{th}. As mentioned above, the observed propagation velocity is slightly slower than thermal velocity, and is in reasonable agreement. In conclusion, the plasma wave (wakefield) was non-resonantly excited by short microwave pulse. The method of excitation was slightly different from that of the LWFA theory. However, the key mechanism of the excitation can be explained by the theory with slight modification.

A present work is supported in part by a Grant-in-Aid from a Ministry of Education, Science and Culture, Japan.

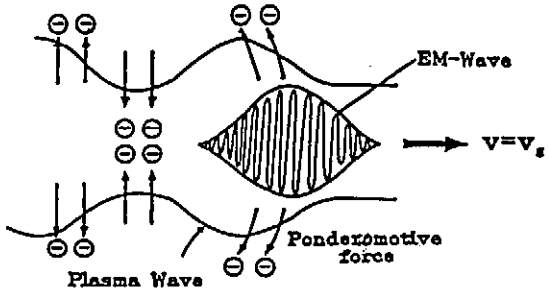

Fig.1 Schematic view of Wakefield Excitation by a Short EM Wave Pulse

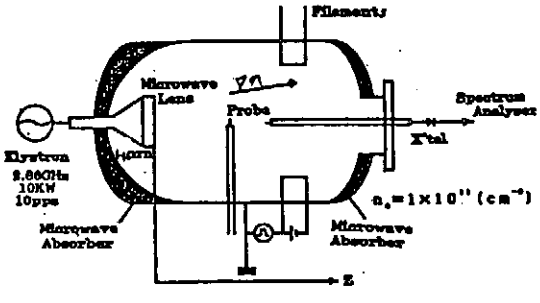

Fig.2 Experimental Set up

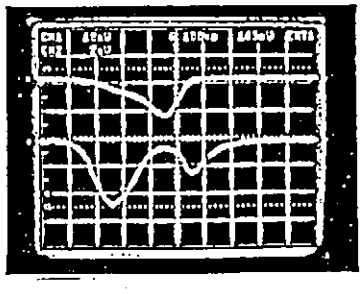

Fig.3 Detected Waves

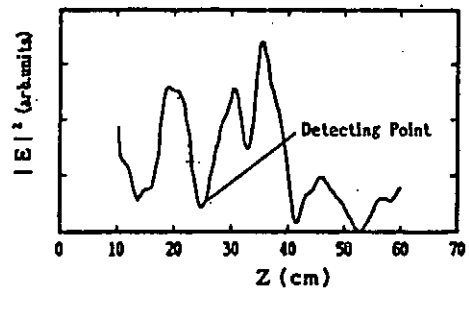

Fig.4 Distribution of Electric Field in the Z-direction

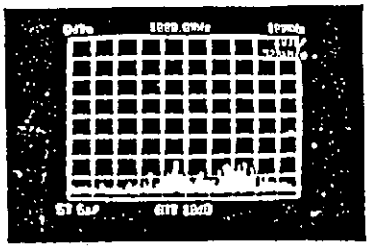

10MHz/div

(a) with plasma

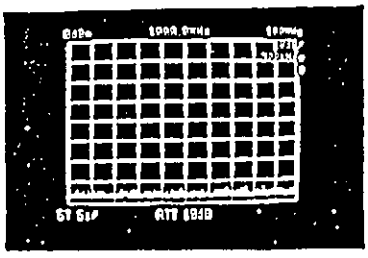

10MHz/div

(b) without plasma

Fig.5 Spectrum observed at Detection Point

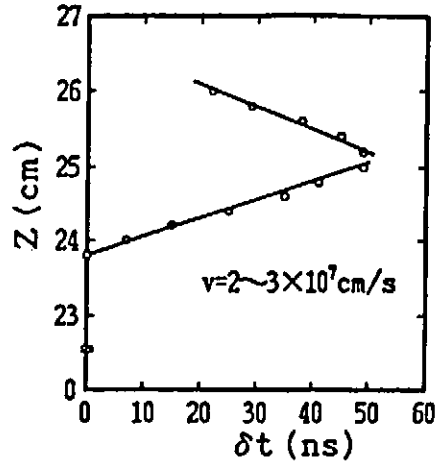

Fig.6 Propagation of Nonlinear Wave

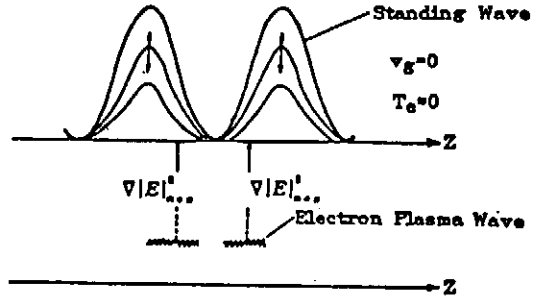

Fig.7 Modification of LWFA Theory

References

1. T.Tajima and J.M.Dawson, Phys. Rev. Lett. 43, 267 (1979).

2. P.Chen, J.M.Dawson, R.W.Huff, and T.Katsouleas, Phys. Rev. Lett. 54, 693 (1985).

3. R.Sugihara and Y.Mizuno, J. Phys. Soc. Japan47, 1290 (1979).

4. Y.Nishida, M.Yoshizumi, and R.Sugihara Proceed of 13th Annual

Anomalous Absorp. Conf., Banff, Albertga (1983); Phys. Lett. 105A.

5.Y.Nishida, M.Yoshizumi, and R.Sugihara and References therein.

6. P.Sprangle, E.Esarey, A.Ting, and G.Joyce, in Proceedings of the Nonneutral Plasma Physics Symposium, Washington, DC, March 28-29,1988 (in press); NRL Memorandum Report 6267 (1988).

7. P.Sprangle, E.Esarey, A.Ting, and G.Joyce, Appl. Phys. Lett.53, 2146-2148 (1988).

Observation of the Plasma Lens Effect

H. Nakanishi, K. Nakajima, H. Kobayashi, A. Ogata
National Laboratory for High Energy Physics, Tsukuba, 305
Y. Yoshida,T. Kobayashi, T. Ueda, K. Miya
Nuclear Engineering Research Laboratory,
The University of Tokyo, Tokai-mura, Naka-gun, Ibaraki-ken, 319-11
N. Yugami, Y. Nishida
Department of Electric and Electrical Engineering,
Utsunomiya University, Ishii-machi, Utsunomiya, 321
H. Shibata and S. Tagawa
Research Center for Nuclear Science and Technology,
The University of Tokyo, Tokai-mura, Naka-gun, Ibaraki-ken, 319-11

abstract

A direct observation of the wakefield self-focusing of an electron beam in a plasma is reported. The transverse beam sizes were measured at three different points downstream of the plasma. The Twiss parameters and the emittance were then derived as a function of the plasma density in the overdense region. Profiles in the holizontal-longitudinal plane were also measured using a streak camera. The experimental results in the vertical direction agree well to a prediction based on linear theory.

1. Introduction

A plasma lens based on self-focusing due to the shielding of space charge of a particle beam by a quiescent plasma has been proposed as a final focus device for the next generation of linear colliders.[1] Its focusing force can exceed those of a superconducting magnet by several orders of magnitude, since a plasma can support very large electromagnetic fields. This concept is experimentally examined in this paper. The results agree well with the theoretical predictions, although certain aspects of the results remain unexplained.

There are two regions in a self-focusing plasma lens: overdense and underdense. The physical mechanism of an overdense plasma lens, in which the plasma density is much larger than the beam density, is as follows. In a relativistic electron beam traveling through a vacuum, a repulsive force due to the space charge of all electrons in the bunch is canceled by an attractive force due to a self-magnetic field of the bunch; thus, the beam almost maintains a constant radius. However, if the same beam now enters a plasma, the plasma electrons respond to the excess charge by shifting away from the beam particles.

The remaining plasma ions neutralize the space-charge force within the beam; although the plasma is very effective at shielding the space charge of the beam, it is less effective at shielding its current. The beam thus experiences almost the full effect of its self-generated azimuthal magnetic field. In an underdense plasma lens, in which the beam is denser than the plasma, the space charge of the electron beam essentially blows out all of the plasma electrons, leaving a uniform column of positive ion charge.

The plasma lens effect was first demonstrated by the ANL group.[2] Because their plasma was dense and long, the focal point fell inside the plasma. They have explained their results by the Bennett equilibrium. Following them, we have reported the effect of a thin overdense plasma lens.[3] The present experiments were conducted in order to verify the previous results, in which the ratio of the plasma density to the beam density ranged up to $n_e/n_b \sim 10$. A higher plasma density region, up to $n_e/n_b \sim 60$, was also explored in the present experiments. The results have shown that (1) the observed plasma lens effect in the vertical direction agrees well with a calculation based on linear theory;[1] (2) indication of an instability was found in the region $n_e/n_b > 50$; (3) the present results seem to reproduce the emittance reduction discovered in the previous experiments.

The next section describes the experimental setup. The results are then compared with a theoretical prediction given in section 3. The last section contains a discussion and conclusions.

2. Experimental Setup

The experiments were conducted at the University of Tokyo on a 18MeV linac.[4] Figure 1 shows the experimental setup. Single-bunch beams were introduced into a plasma chamber. The differential pumping was used to separate the plasma chamber from the linac duct. Transverse beam profiles were observed on three phosphor screens (Desmarquest AF995R) which were located 880, 1380 and 1880mm from the center of the plasma chamber. We call them the first, second and third screens in this paper, counting from the nearest one to the plasma. CCD TV cameras observed images on the three screens, which were triggered in synchronism with the linac beams. A carbon block was set at the end of ths beamline in order to measure the beam current. The fluctuation of the current was within $\pm 5\%$ throughout the data taking. It gave the charge of a bunch as 512pC with a repetition rate of 6.25Hz.

The main differences from the previous experimental setup were[3] as follows: (1) Two quadrupole magenets, a focusing-defocusing pair, were newly installed before the plasma chamber. (2) Remote control of the insertion and extraction of the three phosphor screens has been made possible, and each screen now

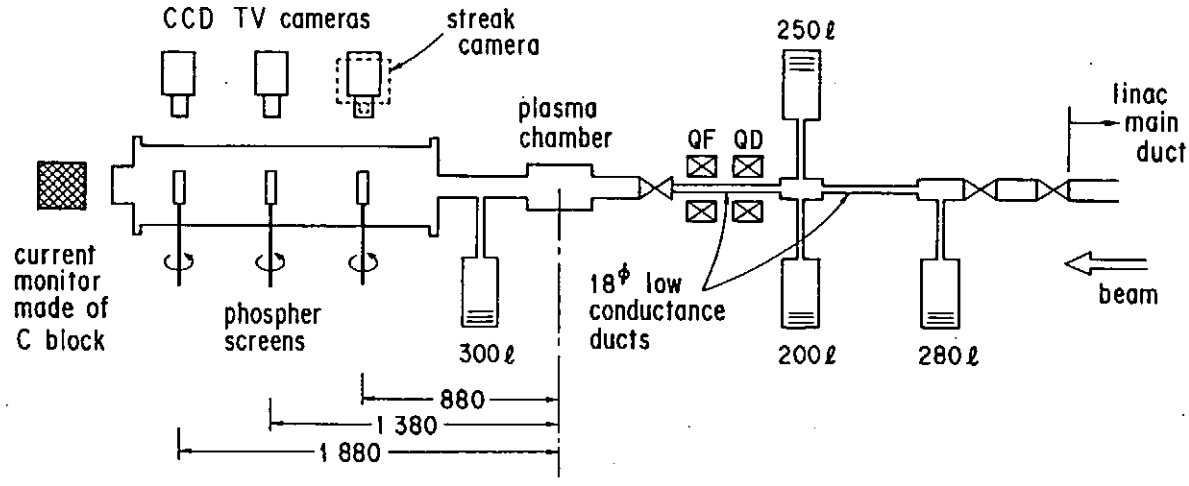

Fig. 1. Experimental setup. The capacities of turbomolecular pumps are given.

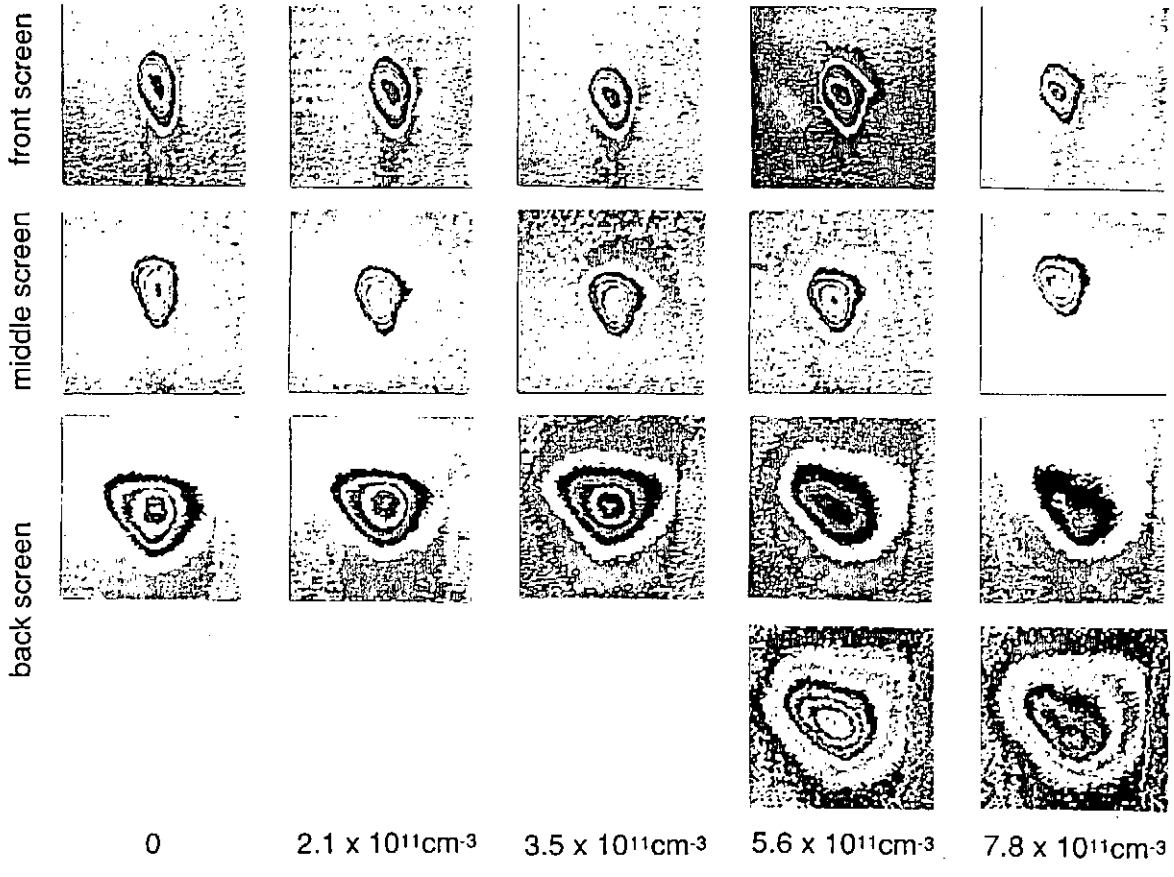

Fig. 2. Typical transverse profiles obtained at three screens. The magnifications are different among the three screens. The contours were processed by the same rule, except for the two out of the matrix, where the sensitivity is increased.

has its own CCD camera. This has enabled us to perform the three measurements at the three screens within one minite, before the plasma parameters changed seriously. (3) A streak camera was used to measure the beam density distribution in the horizontal-longitudinal plane.

The plasma was produced in a chamber (147mm in inner diameter and 360mm in length) by a discharge between the LaB_6 cathodes and the chamber in synchronism with the linac bunch. The plasma pulse width was about 2msec. It was confined by the multidipole field of permanent magnets placed around the chamber periphery.[5] The magnetic field had its maximum value (700G) at the chamber wall. One of the features of this confinement is that there was no magnetic field along the beam transport. The argon plasma density ranged from $.5 - 10 \times 10^{11}\text{cm}^{-3}$ and the temperature ranged from $2.5 - 4\text{eV}$, as measured by a Langmuir probe. The plasma length along the beam transport was about 15cm.

The streak camera was placed so as to observe the same first Desmarquest screen that was used for the transverse profie measurement. Tha horizontal slit in front of the lens introduced light only from the vertical beam center into the camera. The camera caught the ultra-short decay component of the phosphorescence from the Desmarquest screen. The phosphorescent mechanism will be reported elsewhere.[6] In order to obtain good statistics in spite of the poor light intensity, we added 512 streak pictures before computer image processing.

The beam parameters at the plasma center in the absense of a plasma were as follows: $\sigma_{y0} = 2.26\text{mm}$, $\sigma'_{y0} = 0.837\text{mrad}$, $\rho_{y0} = -0.713$, $\sigma_{x0} = 2.77\text{mm}$, $\sigma'_{x0} = 2.25\text{mrad}$, and $\rho_{x0} = -0.956$. Their derivations are described in the next section. The streak-camera measurement gave the rms bunch length as $\sigma_{l0} = 4.18\text{mm}$; this, however, is a value calculated from a superposition of 512 streak pictures. We thus used the value obtained from a single-bunch measurement several years ago, $\sigma_{l0} = 3\text{mm}$.[4] The average electron density inside the bunch becomes $n_b = 1.23 \times 10^{10}\text{cm}^{-3}$.

These two measurements using a streak camera give the resolution of the camera in the longitudinal length measurements as $((4.18\text{mm})^2 - (3\text{mm})^2)^{1/2} = 2.91\text{mm}$. This must be mainly due to the time jitter of the camera triggering.

3. Experimental Results

Figure 2 shows typical transverse profiles on the three screens, caught by the CCD cameras and contoured by a computer. As the plasma density increases, the image changes mainly in the vertical direction. In the density region above $5 \times 10^{11}\mathrm{cm}^{-3}$ or $n_e/n_b > 40$, profiles contoured with increased sensitivity are also given, since the image on the third screen becomes weak and broad. Above $7 \times 10^{11}\mathrm{cm}^{-3}$ or $n_e/n_b > 50$, two peaks are distinguishable on the third screen.

The intensity distribution on each screen was integrated both vertically and horizontally. The horizontal and vertical beam sizes were calculated from the resultant one-dimensional distribution. The so-called rms beam sizes were derived from the width of the distribution, to give $\exp(-1/2)$ of the peak. Figure 3 shows the horizontal and vertical beam sizes as a function of the plasma density. The three bold lines show an approximation using third-order (Fig. 3(a)) and the second-order (b) polynominals. Since no remarkable change is found in the horizontal size except for in the high-density region, the following analysis is made only on the vertical size.

Because we had free space between the plasma and the phosphor screens, we could derive three parameters (two Twiss parameters and the emittance) at the plasma as a function of the plasma density from a set of three data at the three screens. Let us approximate the transverse profile of the beam at the plasma position by a Gaussian characterized by three parameters, σ, σ' and ρ. Specifically, the beam in the transverse phase space at the plasma is expressed by the matrix

$$\Sigma = \begin{pmatrix} \sigma^2 & \rho\sigma\sigma' \\ \rho\sigma\sigma' & \sigma'^2 \end{pmatrix}, \tag{3.1}$$

or the contour equation of the beam is written as

$$\frac{1}{1-\rho^2}\left(\frac{y^2}{\sigma^2} - \frac{2\rho y y'}{\sigma\sigma'} + \frac{y'^2}{\sigma'^2}\right) = 1. \tag{3.2}$$

The beam at the screen i (where $i = 1, 2, 3$) is then expressed by the matrix

$$\Sigma_i = F_i \Sigma F_i', \tag{3.3}$$

where F_i is the transfer matrix of free space with a distance s_i between the plasma and the i-th screen:

$$F_i = \begin{pmatrix} 1 & s_i \\ 0 & 1 \end{pmatrix}; \tag{3.4}$$

F_i' denotes the transpose of F_i. Beam sizes σ_1, σ_2 and σ_3 at the three screens

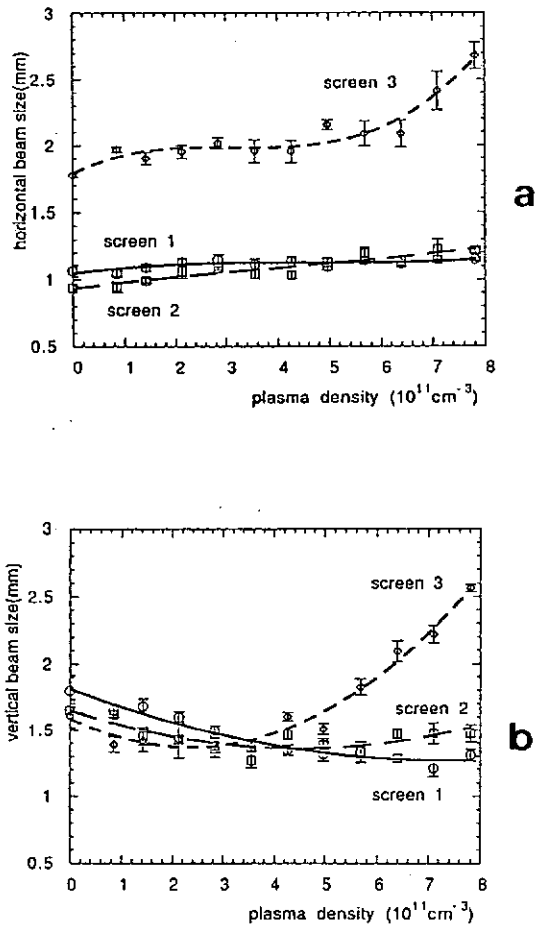

Fig. 3. Horizontal (a) and vertical (b) beam size observed on three screens. Error bars are obtained from values. The lines show approximations using third-order (a) and second-order (b) polynominals.

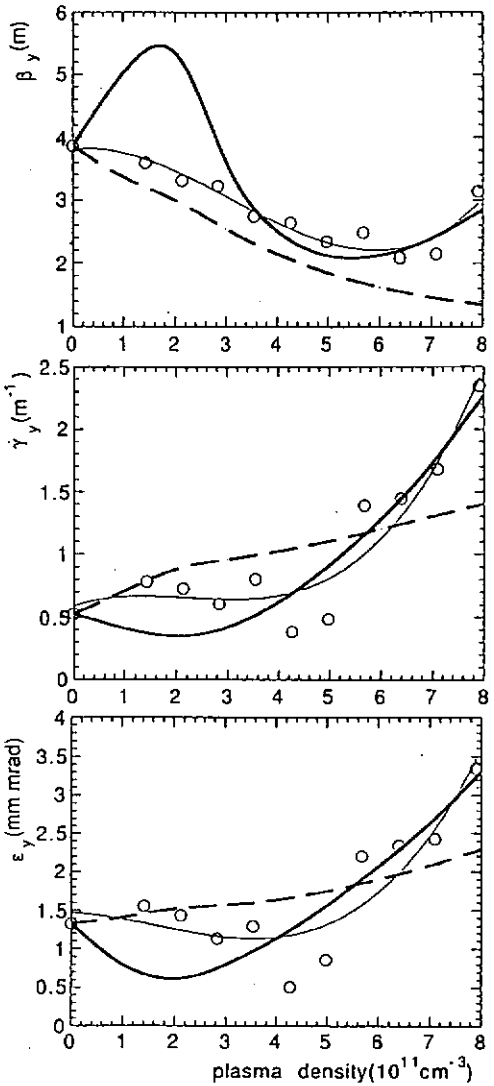

Fig. 4. Dependence of vertical Twiss parameters and emittance on the plasma density. The data points and the thin solid lines were calculated directly from the measeured beam sizes, while the thick solid lines were calculated from the quadratic approximation given in Fig. 3. The dashed lines were calculated based on a round-beam model.

then become

$$\sigma_i^2 = \sigma^2 + 2s_i\rho\sigma\sigma' + s_i^2\sigma'^2. \tag{3.5}$$

Solving the three simultaneous equations with $i = 1, 2, 3$, we obtain σ, σ' and ρ. The Twiss parameters (β and γ) and the emittance (ϵ) are derived by the relations

$$\beta = \sigma^2/\epsilon, \quad \gamma = \sigma'^2/\epsilon \quad \text{and } \epsilon = \sigma\sigma'(1-\rho)^{1/2}. \tag{3.6}$$

The vertical Twiss parameters and the emittance were calculated in two ways from the experimental data. We first calculate directly from a trio of data: σ_1, σ_2 and σ_3. The results are plotted in Fig. 4, whose dependence on the plasma density was approximated by the third-order polynominals (shown by thin solid lines). The second calculation used a method described in the previous report,[3] in which the density dependences of the beam sizes were first approximated by quadratic curves, as shown in Fig. 3(b). The Twiss parameters and the emittance were then calculated as continuous functions of the plasma density from the approximated, but continuous, beam sizes. The thick solid lines in Fig. 4 show the results.

We now try to explain the density dependence theoretically. In the range $n_e > .5 \times 10^{11}\text{cm}^{-3}$, Chen's conditions for the round-beam-limit, $1/(4\pi r_e a^2) \gg n_e \gg 4Nk_p^2 b/(\pi a^2)$, are satisfied[1], where the parabolic profiles in both the transverse and longitudinal directions are assumed to be approximations to a Gaussian, with a and b denoting the bunch radius and half of the bunch length, respectively; *i.e.*, the transverse distribution is approximated by $f(r) = 1 - r^2/a^2$, and the longitudinal distribution is approximated by

$$g(\zeta) = 1 - (\zeta + b)^2/b^2, \tag{3.7}$$

where ζ ($-2b < \zeta < 0$) denotes the longitudinal position inside a bunch. What we observe is the rms size. We consider that the parameters characterizing the parabola distribution (a and b) should be determined so as to give the same area as does a Gaussian distribution with the same peak intensity. We then have

$$a = (9\pi/8)^{1/2}\sigma, \quad b = (9\pi/8)^{1/2}\sigma_l. \tag{3.8}$$

Under these conditions, the focusing strength is proportional to ζ^3:

$$K(\zeta) = \frac{e^2 k_p^2 N \zeta^3}{\gamma mc^2 a^2 b^2}. \tag{3.9}$$

Let us express the beam at the plasma position in the absence of a plasma by a matrix, Σ_0. Using the familiar transfer matrix of a thick lens with length

l,

$$P(\zeta) = \begin{pmatrix} \cos\sqrt{K(\zeta)}l & (\sin\sqrt{K(\zeta)}l)/\sqrt{K(\zeta)} \\ -\sqrt{K(\zeta)}\sin\sqrt{K(\zeta)}l & \cos\sqrt{K(\zeta)}l \end{pmatrix}, \tag{3.10}$$

we can express the beam in the presence of a plasma by

$$\Sigma(\zeta) = P(\zeta)\Sigma_0 P'(\zeta). \tag{3.11}$$

By inserting $\Sigma(\zeta)$ into eq.(3.3), we obtain the beam parameters at a screen. Here, we write the result as $\Sigma_i(\zeta)$, because it is a function of ζ. The beam size at a screen, $\sigma_i(\zeta)$, is the square root of the (1, 1) element of the $\Sigma_i(\zeta)$. The beam size that we have observed is the average of $\sigma_i(\zeta)$ weighted by the longitudinal distribution of eq.(3.7); *i.e.*

$$(\sigma_o)_i = \int_{-2b}^{0} g(\zeta)\sigma_i(\zeta)d\zeta \Big/ \int_{-2b}^{0} g(\zeta)d\zeta. \tag{3.12}$$

The thick lines in Fig. 5 gives the theoretical density dependences of the vertical sizes at three screens, where we set the lens length at 15cm. As it shows, the experimental and theoretical sizes agree fairly well.

Because of the nonlinear operation of eq.(3.12), the resultant longitudinal distribution is no longer Gaussian. This operation does not conserve the emittance, but deteriorates it, if it is perfunctorily calculated from the lefthand side of eq.(3.12), using eq.(3.6). The dashed lines in Fig. 4 show the apparent dependence of the emittance on the plasma density, together with those of the Twiss parameters, β and γ. The figure shows that the experimental emittance reduction overcomes the apparent emittance increase in the low- density region, though the density dependences of the experimentally-obtained emittance are somewhat different due to the two ways of data processing.

From the streak pictures, longitudinal profiles along the beam center were derived. The longitudinal bunch sizes, the barycenter shifts and the peak intensities were then calculated. Here, the bunch size was again defined by using the full-width-exp(-1/2)-maximum. Figure 6 shows them together with thin lines approximating their density dependence by third-order polynominals. The longitudinal line distribution should be proportional to

$$h_1(\zeta) = \frac{g(\zeta)}{\sigma_{x1}(\zeta)\sigma_{y1}(\zeta)} = \frac{1-(\zeta+b)^2/b^2}{\sigma_{x1}(\zeta)\sigma_{y1}(\zeta)}. \tag{3.13}$$

The thick lines in Fig. 6 show the width, the peak position, and the peak intensity calculated from this equation. The peak intensities were normalized by the value in the absence of a plasma. Only the plasma density dependence

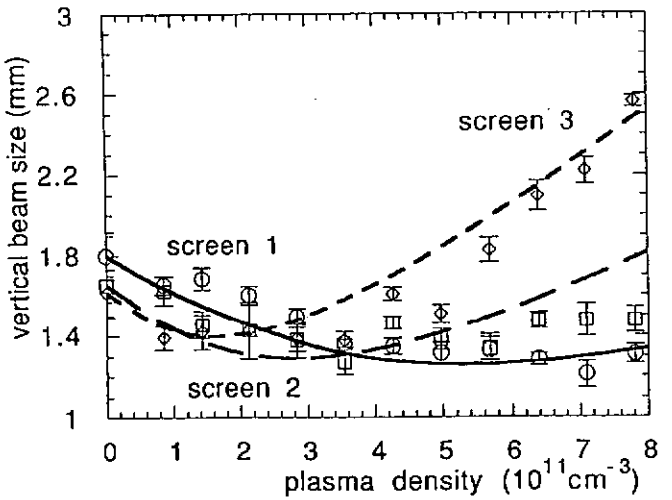

Fig. 5. Theoretical dependences of the vertical beam sizes at three screens on the plasma density. Experimental data are also given.

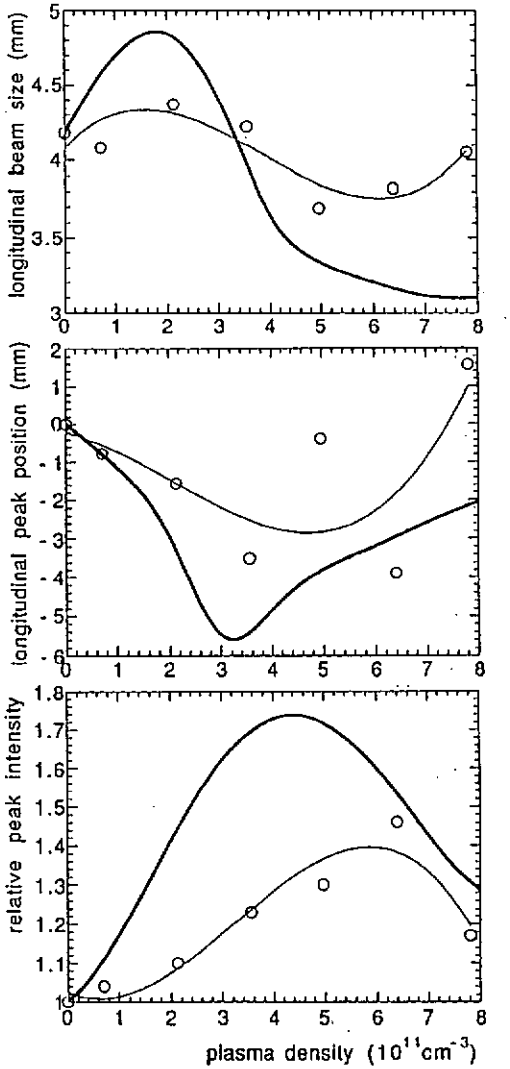

Fig. 6. Dependence of the longitudinal bunch size, longitudinal peak position and peak intensity on the plasma density measured by a streak camera. The peak intensity was normalized by the value in the absence of a plasma. The thick solid lines show theoretical values based on a round beam model, while the thin lines show approximations of experimental data using third-order polynominals.

of the vertical size ($\sigma_{y1}(\zeta)$) was taken into account in the calculation, while the horizontal size ($\sigma_{x1}(\zeta)$) was regarded as being constant. The finite resolution of the streak camera was taken into account in deriving both the width and the peak intensity. Though the tendency agrees between the experiments and theory, the experiments show weaker density dependences for all three curves. It should be noted that the theoretical calculation is not strict, since it adopted a parabolic distribution as an approximation of a normal Gaussian distribution.

4. Discussion and Conclusions

One comment should be made concerning the peak split appearing on the third screen at the high plasma density region of Fig. 2. We found that this structure was quite robust and reproducible. It might contribute to the emittance increase at the high-density region shown in Fig. 4. One of the possible mechanisms causing this peak split would be the Webel instability.[7] However, this instability is possible only for wide beams where $k_p a > \pi$. Our plasma was not sufficiently dense to fulfil this condition.

We cannot explain the phenomenon given in Fig. 3(a), that the plasma lens had little effect in the horizontal direction. Figure 2 shows that the vertical distribution was always broader than the horizontal distribution. This is most remarkable at the first screen. One possibility is the existence of an obstacle upstream of the plasma. If it scraped both the right and left sides of the beam, the beam could not have a Gaussian distribution in (x, x') phase space when entering the plasma. In this case, the lens could not be effective horizontally.

Figure 4 suggests the possibility that the emittance calculation adopted previously[3] might exaggerate its dependence on the plasma density. However, the same figure still shows the existence of a modest emittance decrease in the density region $n_e/n_b < 40$. The previous report[3] suggested a possibility that the transverse-emittance decrease is compensated for by a longitudinal-emittance increase. The hypothesis is as follows. The beam particles experience not only a transverse wakefield to cause the lense effect, but also a longitudinal wakefield to cause deceleration. It is null at the head of the beam and maximum at the tail. A substantial energy spread is thus introduced which increases the longitudinal-emittance. This increase in turn decreases the transeverse-emittance. Though this hypothesis is plausible, no specific mechanism has yet been designated which mixes the particles in six-dimensional phase space to enable transverse-longitudinal coupling. In addition, a fact counter to this hypothesis is suggested in the present experiments: that is, the bunch length shortening shown in Fig. 4. The energy spread could be compensated for by the bunch shortening so that the longitudinal emittance would be conserved independently of the transverse emittance.

We have also tried to study the underdense region. We have found only a large statistical variance in the experimental data because of a weak lens effect. A longer plasma is necessary to study this region using this linac.

In conclusion, these experiments have verified the previous results in one aspect. The two-dimensional linear theory of plasma wakefield still explains the results, in spite of the fact that the measurement was also made in the high plasma density region of $n_e/n_b \gg 10$. However, a new phenomenon was found which caused two peaks on the transverse profile and an emittance increase in the density region above $n_e/n_b > 50$. An emittance reduction was observed below $n_e/n_b < 40$. Its mechanism still remains to be analyzed.

REFERENCES

1. P. Chen, *Part. Accel.* **20** (1987), 171.
2. J. B. Rosenzweig, R. Schessow, B. Cole, C. Ho, W. Gai, R. Konecny, S. Mtingwa, J. Norem, M. Rosing and J. Simpson, *Phys. Fluids* **B2**(1990), 1376.
3. H. Nakanishi, Y. Yoshida, T. Ueda, T. Kozawa, H. Shibata, K. Nakajima, T. Kurihara, N. Yugami, Y. Nishida, T. Kobayashi, A. Enomoto, T. Oogoe, H. Kobayashi, B. S. Newberger, S. Tagawa, K. Miya and A. Ogata, *Phys. Rev. Lett.* **66**(1991), 1870
4. H. Kobayashi, T. Ueda, T. Kobayashi, S. Tagawa, and Y. Tabata, *Nucl. Instr. and Meth.* **B10/11**(1985), 1004.
5. K. Nakajima, A. Enomoto, H. Kobayashi H. Nakanishi, Y. Nishida, A. Ogata, S. Ohsawa, T. Oogoe, T. Shoji and T. Urano, *Nucl. Instr. and Meth.* **A292** (1990), 12.
6. S. Tagawa, to be published in *Proc. 7th. Symp. Accel. Sci. Tech.*, Wako, Japan, 1991.
7. J. J. Su, T. Katsouleas, J. M. Dawson, P. Chen, M. Jones and R. Keinigs, *IEEE Trans. Plasma Sci.* **PS-15**(1987), 192.

X-Band Microwave FEL for TBA Feasibility Study

S. Hiramatsu, K. Ebihara, Y. Kimura, J. Kishiro, T. Monaka*, T.Ozaki,
K. Takayama and D. H. Whittum

National Laboratory for High EnergyPhysics, KEK
1-1 Oho, Tsukuba, Ibaraki, 305, Japan
** The Graduate University for Advanced Studies, KEK*

Abstract

To assess the feasibility of a FEL two beam accelerator, an induction-driven X-band FEL test-stand with ion channel guiding inside the wiggler has been constructed at KEK and an amplifier experiment is in progress. Power in excess of 20MW at 9.4GHz, has been observed with a beam energy of 800keV and a current of 500-700A. Maximum gain is 22dB/m, with no saturation after 15 wiggler periods. Data for the detuning curve, field evolution and current transmission are presented and discussed. The expected performance at 1.6MeV is also discussed.

Introduction

To realize a TeV-class electron-positron linear collider with high accelerating-gradient linacs, the FEL two beam accelerator (TBA/FEL) has been proposed as a power source[1]. In Fig.1 is shown a conceptual illustration of the TBA/FEL. Theoretical investigations in this several years on the essential problems in the TBA concept such as long distance transport of a high current driving beam, bunch stability of the driving beam in the ponderomotive potential of the multi-stage FEL and rf phase stability have shown the intrinsic potentiality of the TBA/FEL for a future linear collider. To assess the feasibility of such a TBA, we proposed an X-band FEL test-stand[2,3], and subsequently modified the design to include ion channel guiding throughout the beamline[4]. The study of such an ion-focussed FEL is motivated by the need for stable transport of a multi-kiloampere beam over large distances in a TBA. In particular ion channel guiding has been proposed to suppress beam breakup caused by the deflecting mode in the TBA induction gaps[5].

At the test stand, the first ion channel transport studies commenced in July, 1989[6,7]. Preliminary FEL experiments commenced in August, with only modest success[8]. Since then, we have extended the wiggler from 12 to 15 periods and shortened the beam line from the injector to the wiggler. Recent measurements reveal a vast improvement in FEL performance.

In this test stand the microwave FEL at 9.4GHz is driven by a 80nsec induction beam with current in excess of 700A, and a voltage of 800kV---too low a voltage at present for the multi-stage FEL configuration which is an essential part of the TBA concept. The purpose of the test stand is to provide experience with high-current beam generation and ion-focused (IFR) transport in the FEL. For TBA studies, we are planning to increase beam energy by extending the induction linac; extension to 1.6MeV is the next step.

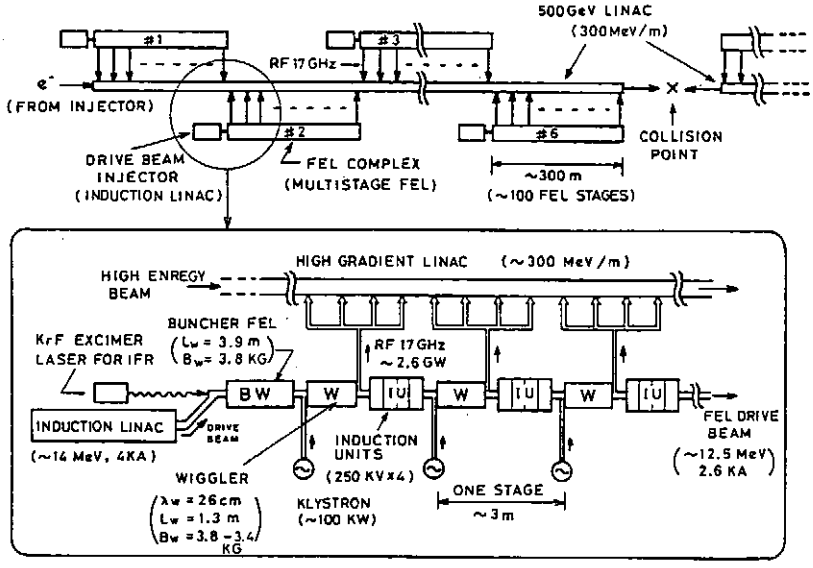

Fig.1 Conceptual illustration of the 500GeV×2 linear collider in the TBA/FEL scheme.

X-band FEL Test-stand

The FEL test stand consists of an injector, a wiggler, the microwave system and the laser guiding system (Fig.2). Further detail is illustrated in Fig.3.

Injector

The beam is drawn from a 50mm diameter velvet cathode of the "laser-based foil-less" type[9], with an anode-cathode gap of 40 mm. The injector consists of 4 induction cells, and each cell produces about 200kV with 80nsec pulse duration, for a beam voltage of 800kV. The induction cells are driven by two magnetic pulse compressors[10]. Output pulse power of each compressor is 3.2GW. One compressor is driven by a gate turn-off thyristor (GTO) switch, with timing jitter less than 2 ns. The other compressor is driven by an air gap switch, with timing jitter of almost 20nsec. (This air gap switch is slated to be replaced with a GTO, since such a large timing jitter is unacceptable for reliable FEL performance.)

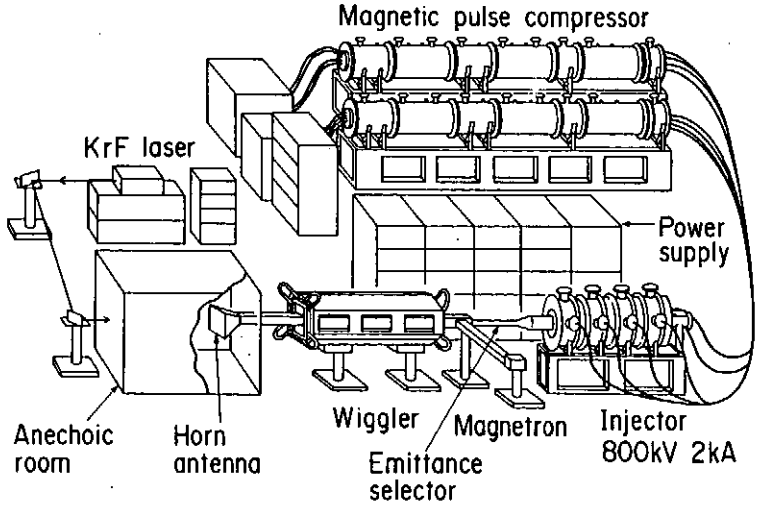

Fig.2 The layout of the KEK FEL test stand.

The beam current after the injector is typically 2.7kA. The normalized beam emittance of 0.41cm rad was obtained by means of a multi-hole plate. At a distance of 40cm from the anode, the beam enters an emittance selector, consisting of a 60cm length tubing with 20mm diameter and tapered entrance. From the emittance selector the beam enters the FEL interaction region, consisting of 5.5cm x11 cm stainless steel waveguide. Beam current is monitored by three Rogowski coils as indicated in Fig. 2. Typical current passed by the emittance selector is 0.5-0.7kA, depending on the laser fluence and Diethylaniline (DEA) gas pressure at the injector. Just after the wiggler, the beam is dumped on the waveguide wall with a steering coil.

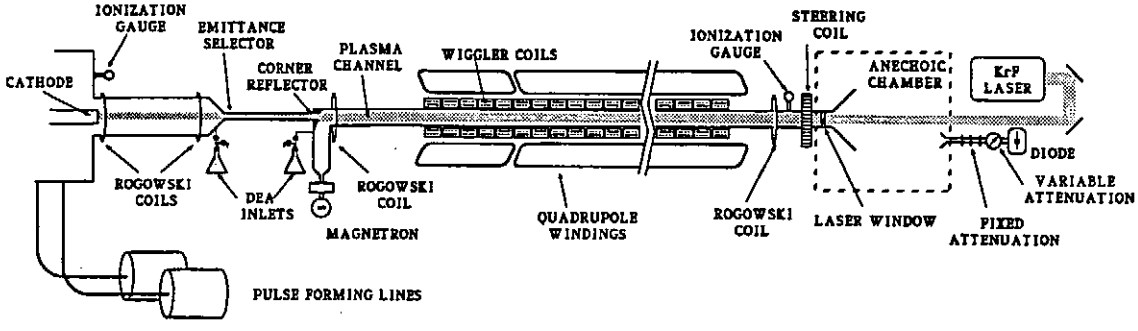

Fig.3 Details of the beamline set-up.

Wiggler

The wiggler is the planar, reversed coil type with 15 periods and a 16cm wiggler period length. The magnetic field is produced by exciting solenoid coils and by eddy current in copper plate placed on the vertical walls of the stainless steel waveguide[11]. The fifteen power supplies are wired so that the first two half periods may be adjusted for orbit matching. The repetition rate of the power supplies is 0.1Hz. Two air core quadrupole magnets provide additional orbit matching at the entrance, and focussing in the wiggle plane.

Microwave system

The microwave source is a pulsed magnetron operating at 9.4GHz. The microwave signal is converted from the TE_{10} mode to TE_{01} via a tapered waveguide, and fed into the beamline (5.5cm x 11cm waveguide) with a corner reflector. The corner has a beam passing aperture covered with thin wire mesh. The microwave power in the oversized rectangular waveguide is amplified and passed through a laser window and a horn into an anechoic chamber. The laser window is transparent to both the KrF laser and the microwave. The receiving horn is placed 1.8m from the transmitting horn at an angle of 3° from the forward direction, so as not to interfere with laser guiding. The signal is attenuated and detected by a crystal diode, calibrated via thermistor and powermeter. A second horn, mounted on a turntable is used to study the horizontal and vertical components of the mode profile in the horizontal plane.

IFR beam transport

DEA gas is fed into the beamline from two flasks as indicated in Fig.3. The gas pressure is monitored by two ionization gauges of the Bayard-Alpert type, placed at the injector and the wiggler exit. A Lambda-Physik KrF laser operating at 248nm with 18nsec pulse length is used to ionize the DEA by a two-photon resonant process[12]. Laser pulse energy is measured by joulemeter and typically is 50-100mJ, with a shot-

to-shot jitter of 1mJ. The laser diameter is 2.5cm. In practice, gas pressure and laser fluence are critical in tuning beam transport. The experiments are performed under the nitrogen-equivalent pressure of 0.3mTorr at the wiggler exit. The resulting current transmission through the wiggler is depicted as a function of wiggler field strength in Fig.4. By tuning gas pressure and magnetic field, we can achieve up to 90% current transmission over a useful range of wiggler field.

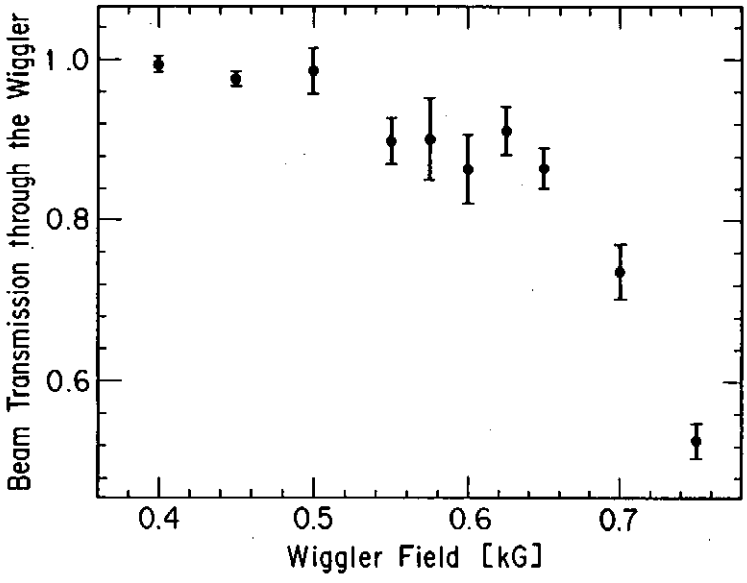

Fig.4 Beam transmission ratio versus peak wiggler field.

FEL Amplification

To date the maximum power achieved is 25MW, with an input RF power of 18kW. For this shot the beam energy was about 760keV and the current passed through the wiggler was 520A. The rf pulse is depicted in Fig. 5, together with the beam current. The full width of the amplified microwave signal was 40-50nsec.

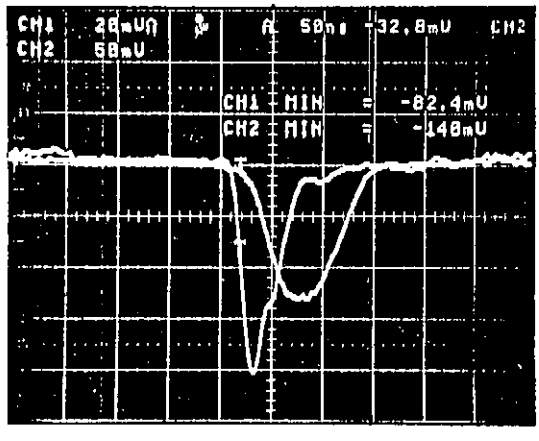

Fig.5 Oscilloscope trace of the amplified microwave signal, and the beam current (broad trace). (The beam is delayed by 50 nsec due to the difference in the cable lengths.)

In Fig. 6, the measured detuning curve is depicted. The scatter in the figure is due to beam voltage variation produced by the timing jitter of the air-gap switch. These data correspond to a timing difference of less than 10nsec. Maximum gain occurs at 620 gauss, or 87% of the resonant field. The height and location of the peak can be understood from Raman FEL theory. The gain observed at low wiggler field can be attributed to the "head" and "tail" of the beam voltage profile. The evolution curve is shown in Fig.7 and corresponds to an exponential gain of 20.8dB/m, with no saturation. The maximum gain obtained so far is 22dB/m and saturation has not been observed.

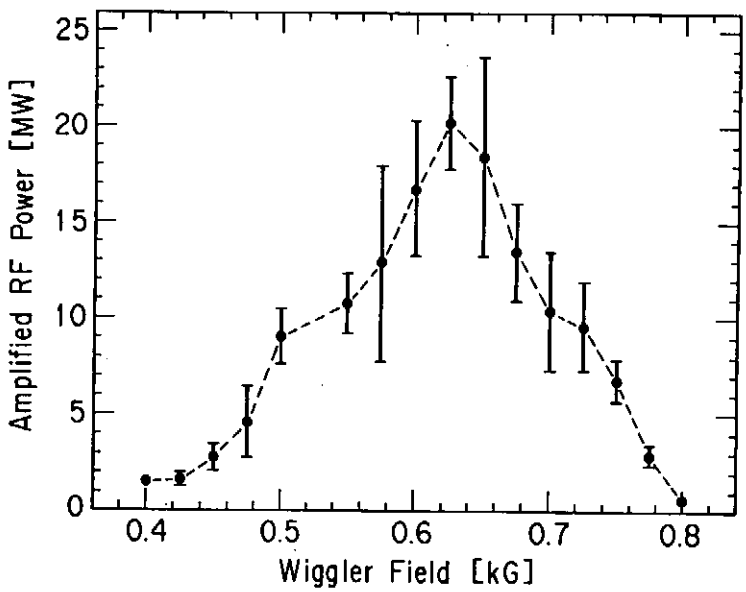

Fig.6 Microwave power versus peak wiggler field.

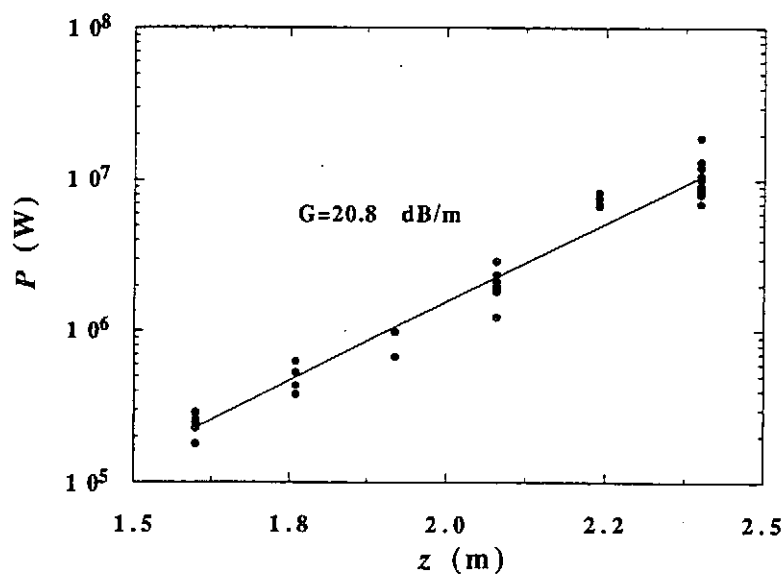

Fig.7 The evolution of the microwave power through the wigggler corresponds to an exponential gain of 20.8dB/m.

Although the dominant mode for the FEL amplification is TE_{01} mode, theoretically one expects a non-negligible coupling to the TE_{11} mode or TE_{21} mode. We have begun preliminary studies of the mode profile in the horizontal plane of the anechoic chamber. Indeed, interference is evident in the measured field profile. However, at present the mode content appears to vary from shot to shot and we are continuing to study possible explanations, including mode conversion in the laser plasma.

The frequency was measured by using bandpass filters. At 600 gauss, 63 % of the amplified power lies within a bandwidth of 9.320-9.460 GHz, while 72% of the magnetron lies within this bandwidth. The component in the Ku-band is less than one percent.

Discussion

We have demonstrated beam transport and microwave amplification in an ion-focussed free-electron laser. Detailed theoretical studies of the detuning curve are in progress and have thus far shown that low energy and space-charge corrections, as well as multi-mode effects are important. To analyze the experimental data, we developed a one-dimensional FEL dispersion relation without high-γ approximation following essentially the treatment of Orzechowski *et al.*[13], while including space-charge using a harmonic model. The best fit to the data is shown in Fig.8 corresponding to a ±2.1% detuning spread and a 2.0cm beam radius. The peak gain and corresponding wiggler field B_W in the measured detuning curve agree well, underscoring the importance of space-charge. In order to confirm this simple fit, current experimental efforts are focused on reaching saturation which is expected in the 50MW range.

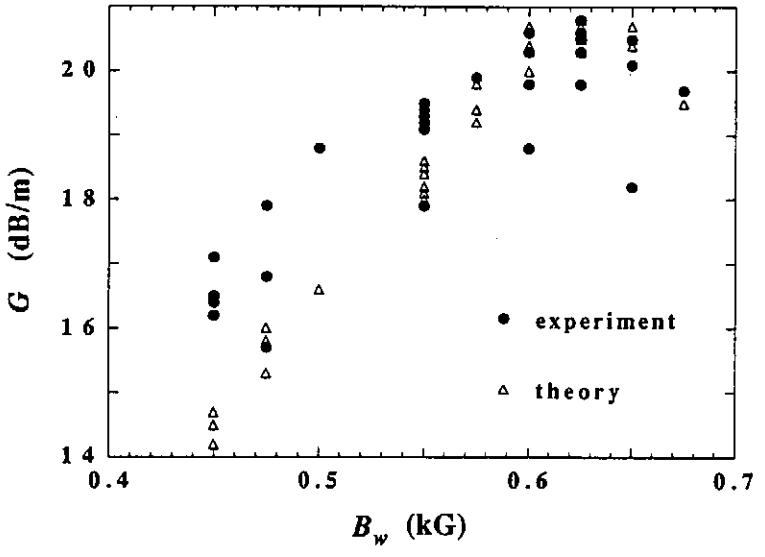

Fig.8 Experimental detuning data and theoretical best-fit with the low-γ 1-D warm Raman dispersion relation. Scatter is due to variation in beam current.

Due to the complexity of the nonlinear ion-focussing problem, an understanding of the current loss at high wiggler field is best approached numerically. To this end we have developed a 3-dimensional FEL simulation incorporating realistic beam transport effects and detailed "benchmarking" of the code is in progress to confirm the equilibrium spot-size and current loss characteristics.

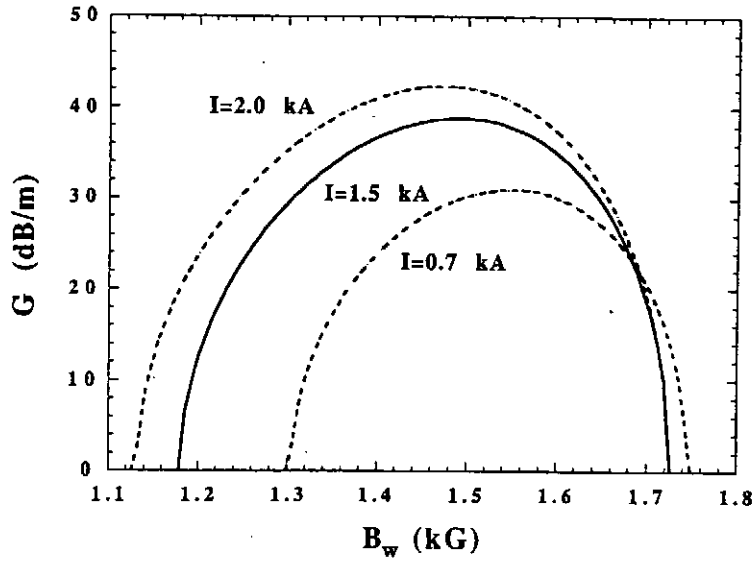

Fig.9 Expected gain at 1.6MeV.

Since more than several MeV will be desirable to the TBA, the beam energy will be increased year by year by extending the induction linac. The extension program to 1.6MeV will be completed in next spring and much higher gain and power are expected since gain degradation by space charge will be less severe. As shown in Fig.9, the theoretical calculation at this energy with ±1% energy spread, and a spot-size of 1.85cm predict gain of 31dB/m (an improvement of 10dB/m), and saturation before the 12th wiggler period at 130MW (for 30kW input). With tapering more than 250MW could be achieved. At the same time, one expects that at higher energy a large current could be transported due to the reduction in transverse space-charge effects. For 1.5kA, gain of 39dB/m could be expected with saturation at 370MW. With tapering more than 700MW could be achieved.

One of us (DHW) was supported by the Japan Society for the Promotion of Science.

References

1) A.M.Sessler, AIP Conf. Proc. 91 (1982) 163.
2) S.Hiramatsu *et al.*, Nucl. Instr. and Meth. A285 (1989) 83.
3) S.Hiramatsu *et al.*, Proc. of the Tokyo Int. Symp. '90 on FEL, Tokyo, Japan, 1990; JAERI-M 91-141, 1991, p96.
4) K.Takayama and S.Hiramatsu, Phys. Rev. A37 (1988) 173.
5) G.J.Caporaso *et al.*, Phys. Rev. Lett. 57 (1986) 1591.
6) T.Kurino *et al.*, Part. Accel. 31 (1990) 89.
7) T.Monaka *et al.*, Proc. of the 7th Symp. on Accelerator Science and Technology, Osaka, Japan,1989, p181.
8) T.Ozaki *et al.*, ibid., p183.
9) S.L.Shope, C.A.Frost, G.T.Leifeste, and J.W.Poukey, Phys. Rev. Lett. 58 (1987) 551.
10) J.Kishiro *et al.*, Part. Accel. 31 (1990) 83 .
11) K.Takayama *et al.*, KEK Preprint 89-152.
12) C.A.Frost, J.R.Woodworth, J.N.Olsen, and T.A.Green, Appl. Phys. Lett. 41 (1982) 813.
13) T.J.Orzechowski *et al.*, IEEE J. Quant. Electron. 21 (1985) 831.

MeV/u Cluster Generation

Yasushi IWATA, Naoaki SAITO, Mitsumori TANIMOTO, Kiwamu SUGISAKI, Shigeyuki SEKINE, Hajime SHIMIZU and Yoichi KIMURA

Electrotechnical Laboratory, 1-1-4 Umezono, Tsukuba-shi, Ibaraki 305, Japan.

We propose a new principle for the generation of cluster beam with a high energy up to more than 1 MeV/u. Multiply-charged clusters have a critical size below which they are intrinsically unstable with respect to the Coulomb repulsion between atomic ions. Accordingly, it is difficult to accelerate cluster directly up to high energy, and then, another way should be necessary to produce a high energy cluster. The principle we propose, is consist of three steps; acceleration of atomic ions up to more than 1 MeV/u, condensation and cooling of the ion beam in a storage ring, and neutralization of ions and aggregation due to associative collision of neutral atoms.

1. Introduction

Solid materials generally contain tens of thousands of atoms in their space of ten nm in diameter. Small particles consisting of less than just the same number of atoms are commonly called clusters. If energetic clusters of MeV/u are generated, the constituent atoms collide with a target in maintaining a high density of solid level. The high energy cluster beam is a ultra-short-pulsed beam with a ultra-high current density. We consider, for an example, 1 MeV/u $^{23}Na_{100}$ clusters which consist of 100 sodium atoms and have the total energy of 2.3 GeV. The Na_{100} clusters, which are particle of 1.4 nm in diameter moving with a velocity of $1.4\times10^{9} cm/sec$, pass through a surface layer of $3\times10^{-8} cm$ in thickness in a period of $2\times10^{-17} sec$. The injected electrical power density per cluster is $4\times10^{21} W/cm^2$. Such a high power density cannot possibly achieved by the usual ion beam, and is much greater than that obtained by the power laser which have been constructed up to the present.[1,2]

Cluster-ion beams with high energies but not up to 1 MeV/u, have been obtained in the several facilities. Small molecular-ions, (H_2^+, HeH^+, CH^+, NH^+, OH^+, H_3^+, CH_2^+, NH_2^+, OH_2^+, CO_2^+, CH_3^+, CH_4^+, $\cdots$),have been accelerated at Argonne's $4MV$ Dynamitron,[3] and at New York University,[4] the University of Lyon[5] and the Weizmann Institute[6]. the molecular-ions passing through a thin foil are charge-stripped and then are disintegrated in to atomic fragments by the Coulomb explosion. The fragment patterns so called ring patterns, reflect the structures of the molecules before disintegrated. Au_n^+ or Au_n^{2+} ($2 \leq n \leq 20$) ions have been accelerated at University of Paris for the study of the cluster stopping in dense plasmas at an energy range from 38 keV/u to 380 keV/u.[7] A cluster ion accelerator with an acceleration voltage up to 1 MV was built in Karlsruhe to produce intense cluster-ion beams of hydrogen of several eV per atom.[8] The beams are of interesting in nuclear fuel injection into fusion devices as well as in the production of negative hydrogen ions for plasma heating. Cluster-ion impact of DD fusion has been demonstrated using $D^+(D_2O)_n$ clusters impinging on targets of $TiD(C_2D_4)_m$

and $ZrD_{1.65}$, at the 300 kV (recently 750 kV also available) Cockcroft-Walton accelerator of Brookhaven National Laboratory.[9]

In this article, we propose a new principle for the generation of cluster beam with a high energy up to more than 1 MeV/u.

2. Restriction on the cluster acceleration

Using the classical-electrostatic (or jellium calculation) the ionization potential W which is necessary to remove an electron from a uniformly conducting sphere of radius R having Z elementary charges e, is

$$W = W_\infty + \left(Z + \frac{3}{8}\right)\frac{e^2}{r+\delta}. \tag{1}$$

where W_∞ represents the bulk polycrystalline work function, δ is the spill-out factor.[10] The equivalent sphere radius r of the metal cluster having n atoms is $r_s n^{1/3}$. To obtain a high energy clusters with use of the usual electrostatic or linear accelerator, we must multiply ionize the clusters of large mass number. The multiply-charged clusters M_n^{z+}, however, have the critical size n_c below which they are intrinsically unstable with respect to the Coulomb repulsion between atomic ions. Considering a dissociation process,

$$\begin{aligned} M_n^{z+} \;&\rightarrow\; M_{n-1}^{z+} + M \rightarrow M_{n-1}^{z+} + M^+ + e^-, \\ &\searrow\; M_{n-1}^{(z-1)+} + M^+ \nearrow \end{aligned} \tag{2}$$

we get the energy conservation relation

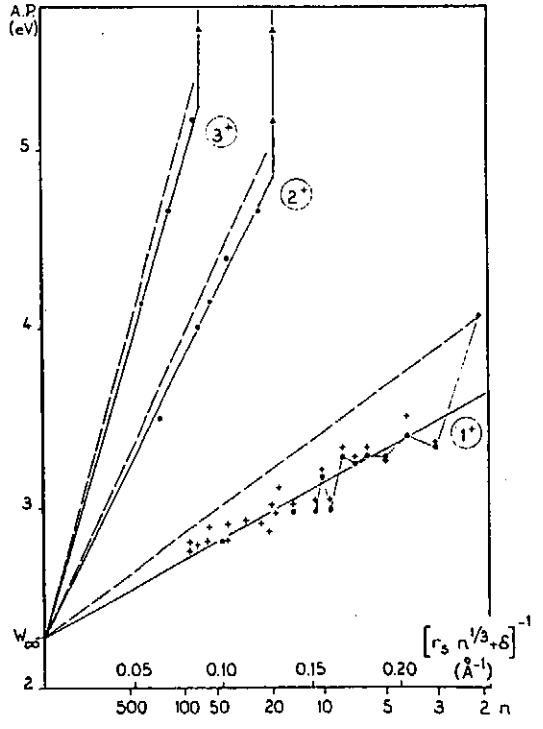

Figure 1. Appearance potential for single, doubly, and triply charged potassium clusters plotted vs the quantity $[r_s n^{1/3} + \delta]^{-1}$. The respective experimental straight lines $1^+, 2^+, and 3^+$ coincide with those predicted by Eq. (5).. $W_\infty = 2.28eV$. The triangles represent the measured critical sizes. (Ref.10).

$$B_n + I(M) = B_n^+ + I(M_{n-1}^{(z-1)+}). \tag{3}$$

B_n and B_n^+ are the dissociation energies associated with the ejection of monomer and ion, respectively. $I(M)$ and $I(M_{n-1}^{(z-1)+})$ are the ionization potentials of M and $M_{n-1}^{(z-1)+}$, respectively, the potentials which are given by eq.(1). M_n^{z+} spontaneously ejects M^+ if $B_n^+ \leq 0$. Then eq.(1) and (3) give us the critical size,

$$n_c = 1 + \left[\frac{(Z - \frac{5}{8})e^2}{r_s\{I(M) + B_n - W_\infty\}} - \frac{\delta}{r_s}\right]^3. \tag{4}$$

C.Bréchignac's group[10] examined the photoionization threshold of potassium cluster and demonstrated that the ionization potentials of the clusters for $Z = 0, 1, 2$ are given by eq.(1), as shown in fig.1. Taking $I(K)$=4.34 eV, B=0.7 to 0.85 eV in the range $n = 20$ to $n = 100$, W_∞=2.28 eV, r_s=2.57 $\AA$ and δ=0.83 $\AA$, They determined the critical sizes of potassium cluster to be $n_c = 16$ for K_n^{2+} and $n_c = 75$ for K_n^{3+}.

Accordingly, the critical size of multiply ionized cluster ions restricts us to ionize the clusters highly enough to accelerate them up to high energy. For example, the ratio of mass to charge M/Q for ${}^{40}K_{75}^{3+}$, ${}^{40}K_{235}^{4+}$, ${}^{40}K_{530}^{5+}$ are 1000, 2350 and 4240, and the critical sizes given by eq.(4) are 75, 235 and 530, respectively. The available maxima in energy for potassium cluster ions of Z =3, 4, 5 are 20 keV/u 8.5 keV/u and 4.7 keV/u, respectively, even if the cluster ions are electrostatically accelerated at 20 MV. Then another way should be necessary to produce a high energy cluster.

3. New generation principle

The principle of the high-energy cluster generation we propose, is consist of three steps; acceleration of atomic ions, storage in a ring and cooling, and neutralization of ions and aggregation due to associative collision of neutral atoms.

3-1. Laser cooling [11,12]

We consider a two-level system in free ions with mass M which possess a resonant electric dipole transition of frequency ν_0 with natural linewidth γ. Suppose that we irradiate these ions with monochromatic directed radiation tuned slightly lower than the resonance frequency. We assume that the intensity is low enough not to cause saturation, and that the monochromaticity is high comparably with the line width. Those ions traveling against the radiation and Doppler-shifted to the resonance frequency ν_0, scatter the incoming light at a higher rate than those ions Doppler-shifted away from resonance. The ion receives a momentum impulse $\hbar\vec{k}$ in the absorption process where $\vec{k}$ is the photon wave vector. In the reemission process, however, the ion receives the randomly oriented momentum and undergoes a random walk in momentum space. The average net momentum per scattering event transferred to the ion is $\hbar\vec{k}$ and the ionic velocity is changed by an amount $\vec{v}_r = \hbar\vec{k}/M$. When the ionic velocity $\vec{v}$ and $\vec{k}$ are antiparallel, cooling occurs. The Doppler shift is $\vec{k}\cdot\vec{v}$ and becomes $\vec{k}\cdot\vec{v} - \frac{1}{2}\nu_0\beta^2$ in the relativistic case, and the recoil energy $R = (\hbar k)^2/2M$. The change in the kinetic energy of the ion per scattering event is

$$\Delta E_{ion} = \hbar\vec{k}\cdot\vec{v} + 2R. \tag{5}$$

Following eq.(5) cooling occurs as long as $\hbar\vec{k}\cdot\vec{v} \ll -2R$.

We consider, for an example of cooling, the D_2 line of sodium ions ($M = 23$) with a line width $\hbar\gamma$=$2.6\times10^{-7}eV$. Supposing the initial temperature as $2000K$, the average velocity v_{rms} is $1.2\times10^{5}cm/s$, $2R$=$2.1\times10^{-10}eV$, $\Delta E_{ion} = 8.3\times10^{-6}eV$. Then it needs more than 3.1×10^{4} scattering events to cool down the sodium ions to the recoile energy.

Cooling may be treated by the phase-space distribution function $f(z,v,t)$ of ions under light pressure. The behavior of the distribution function is described by the Fokker-Plank equation;

$$\left(\frac{\partial}{\partial t} + v\frac{\partial}{\partial z}\right) f = \frac{\partial}{\partial v}(-\phi f) + \frac{\partial^2}{\partial v^2}(df); \tag{6}$$

$$\phi = -\frac{\gamma\kappa^2 v_r}{(\Delta - \vec{k}\cdot\vec{v})^2 + \gamma^2 + 2\kappa^2}, \tag{7}$$

$$d = \frac{1}{2}\frac{\gamma\kappa^2 v_r^2}{(\Delta - \vec{k}\cdot\vec{v})^2 + \gamma^2 + 2\kappa^2}(1+\alpha), \tag{8}$$

where κ is the Rabi frequency and Δ is the detuning from resonance. Equation (7) gives the spontaneous cooling force, and eq.(8) is the diffusion. α is a factor for the random walk of ions. Solving the equation of motion for an ion under the velocity-dependent force $\phi(v)$,

$$\frac{dv}{dt} = \phi(v), \tag{9}$$

we can get the velocity at an arbitrary time t for an ion with an arbitrary initial velocity v_0.

Schöder's group accomplished the first successful laser cooling of $^7Li^+$ ions stored at the energy of $13.3MeV$ ($\beta = 0.064$) in the Heidelberg Test Storage Ring.[13] The ion beam was merged with a copropagating beam from a single-mode Ar^+-ion laser and a counter-propagating single-mode dye-laser beam. The transition of $^3S_1(F=\frac{5}{2}) \rightarrow ^3P_2(F=\frac{7}{2})$ in $^7Li_+$ ions was used. The laser saturation intensity for the transition is 8.8 mW/cm^2. The velocity distribution of the ions was measured by fluorescence detection at 90° as a function of the laser frequency detuning. The initial fluorescence signal width was 1.9 GHz which is corresponds to a temperature of the longitudinal motion of $T = 260K$. Using electron cooling to reduce the transversal temperatures which affects the longitudinal temperature. They finally suppressed the energy spread of the ion beam below 200 mK (35 MHz).

3-2. Neutralization

Suppose a swift positive ion collide with free electrons. The necessary condition for electron capture of the ion is that the relative kinetic energy of electrons to the ion is less than the electron-binding energy of the ion ; $\frac{1}{2}m_e v_{rel} < e^2Z/r$. Then the probability of electron capture has the maximum when electrons travel with the same velocity as of the ion. The neutralization rate of a swift positive ion generally depends on the electron density $\rho(r, v_{rel})$ in the phase space.

3-3. Interaction between neutral atoms

Considering two neutral atoms separated by r, the electrical dipole-dipole interaction is dominant. The interaction may be roughly estimated by the following simple picture of two dipole oscillators with the frequency of ω_0 separated by r. As they interact with each other but still in long-range, the eigenstates of the system become nondegenerate and have different eigenvalues $\frac{1}{2}\hbar\omega_\pm = \frac{1}{2}\hbar\omega_0\sqrt{1\pm\kappa}$, where $\kappa = \alpha/r^3$ is a coupling constant and α is the polarizability. The interaction energy,

$$\begin{aligned}\Delta E &= \frac{1}{2}\hbar(\omega_+ + \omega_-) - \frac{1}{2}\hbar(\omega_0 + \omega_0) \\ &\simeq -\frac{\hbar\omega_0\alpha^2}{8r^6}\end{aligned} \tag{10}$$

is proportional to r^{-6}. This is so called the London-van der Waals' force. If the states of the oscillators are different from each other the first-order κ-term remains in ΔE. Supose one (e.g. +) is in the excited state of the quantum number n, while another (-) in the state of m ($m \neq n$). We may represent the interaction potential as follow:

$$\begin{aligned}\Delta E &= \left(n+\frac{1}{2}\right)\hbar(\omega_+ - \omega_0) + \left(m+\frac{1}{2}\right)\hbar(\omega_- - \omega_0) \\ &= (n-m)\frac{\hbar\omega_0\alpha}{2r^3} - o\left(\frac{1}{r^6}\right) + \cdots.\end{aligned} \tag{11}$$

This means that the potential is proportional to r^{-3} and affects in a longer range compared to the London-van der Waals' potential.

The polarizability α of an atom is defined in terms of the energy shift of the atomic state exposed to a weak electric field in the direction z as follows:[14]

$$\begin{aligned}\Delta &= -\frac{1}{2}\alpha\epsilon_0 E^2 \\ &= -\frac{1}{2}\left(\alpha_0 + \alpha_2\frac{3J_z^3 - J(J+1)}{J(2J-1)}\right)\epsilon_0 E^2\end{aligned} \tag{12}$$

where α_0 and α_2 are respectively the scalar and tensor polarizabilities, $\vec{J}$ is the total electronic angular momentum, and ϵ_0 is the vacuum permittivity. Both polarizabilities are expected to scale with n^7.

$$\alpha \propto n^7 \tag{13}$$

The n^7 dependence was verified for the scalar polarizability[15] and for the tensor polarizability[16] of the $40D$ and $60D$ states of caesium.

We consider highly excited neutral atoms immediately after electron capture. The atomic state of the neutral atoms may widely distribute. The suggestive equations (11) and (13) indicate that the interaction between the highly-excited neutral atoms is a long-range interaction and the magnitude of it is larger than that between the neutral atoms in the ground state. Accordingly, we may expect that the interactions between the highly excited neutral atoms make them to aggregate. If the relative kinetic energies between the neutral atoms are smaller than the dissociative energy of cluster but are sufficiently high enough to take place a associative collision between

them, then clusterization of the neutral atoms will occ10ur under the sufficient density of atoms.

3-4. Generator system

Applying the three processes mentioned above to atomic ion beam, we may principally produce a high energy cluster beam. We show in fig.2 the apparatus system. First, atomic ions are accelerated up to the energy higher than 1 MeV/u by the linear accelerator.

After the acceleration, the beam are injected to the storage ring, and are stacked in transverse and longitudinal phase space to increase the beam density. Cooling is performed by copropagating and counter-propagating laser beams in response to the need; in the case that the temperature of the beam is too hot to occur the associative collision in the atomic beam after neutralization. $B\rho$ required for the storage ring is 4.14 Tm for e.g. 1 MeV/u $^{23}Na_+$ ions. The vacuum limits the life of ions not to stray by charge-exchange collisions with residual gas. The life of 1 MeV/u ions is 1 sec at $2 \times 10^{-8} Pa$, and ions travel a distance of $1.3 \times 10^7 m$ for the period.

The third step is electron beam merging into the ion beam for neutralization. The ions capturing the merged electron become highly-excited neutral atoms. If the density of the swift atoms is sufficiently high, aggregation and then clustering may occur. If we magnetically carry out the mass-analysis of the swift clusters consist of e.g. $(^{23}Na_{100})^+$ of 1 MeV/u , the magnitude of $B\rho = 3.3 \times 10^2$ Tm is necessary.

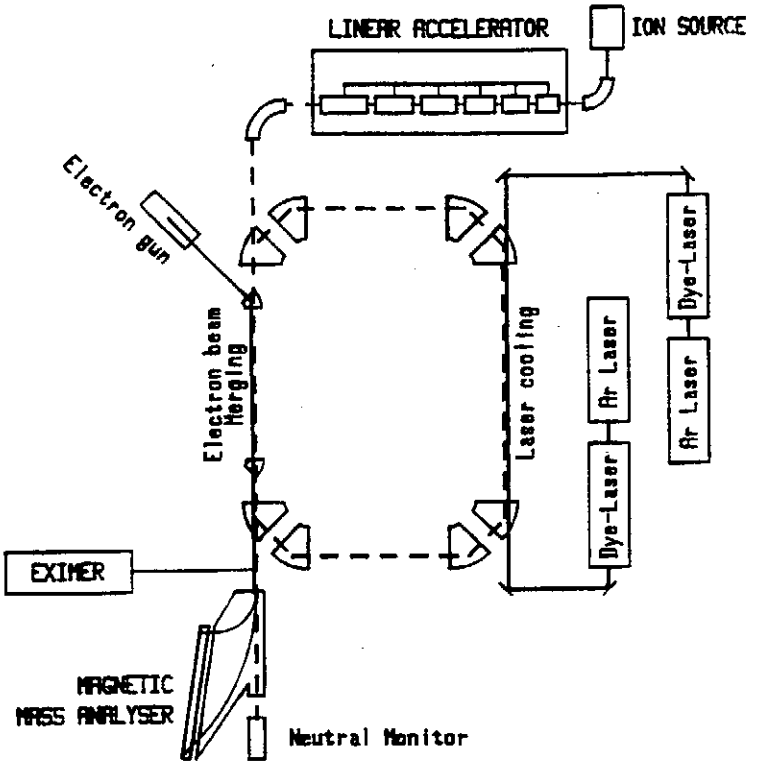

Figure 2. Generator system for a high energy cluster beam.

4. Discussion

Consider the collision between a Rydberg atom $A^*(n)$, $n \gg 1$, and a ground-state atom A,

$$A^*(n) + A \rightarrow A_2^+ + e \quad (14)$$

$$\searrow A^+ + A + e \quad (15)$$

Channel (14) is associative ionization and is the simplest collision leading to the formation of a chemical bond. This process is predominant when the total collisional energy is less than the dissociation energy of A_2^+. Channel (15) is termed Penning ionization and can take place when the total energy is above the limit. The reaction rate per ground-state atom is

$$\frac{dA_2^+}{dt} = \sum_{n=1}^{\infty} k(n)\rho^*(n), \quad (16)$$

where $k(n)$ and $\rho^*(n)$ are respectively the rate constant and the density of Rydberg-state atom in the n state. J.Weiner and J.Boulmer[17] examined the associative ionization and measured the rate constant as a function of n at temperature of 1000 K. Figure 3 showing the results indicates the maximum of the rate constant $k_{max} \simeq 1 \times 10^{-9} cm^3/s$. Regarding the probability of the associative collision is unity in the Rydberg atom $r \leq r_n$, the temperature dependence of k_{max} is given by[17]

$$k_{max}(T) = \pi r_n^2 f(T) \quad (17)$$

where $f(T)$ is the Maxwellian velocity distribution. Equation (17) show that the rate constant is large as T becomes high. But the dissociative collisions occur at too high temperature.

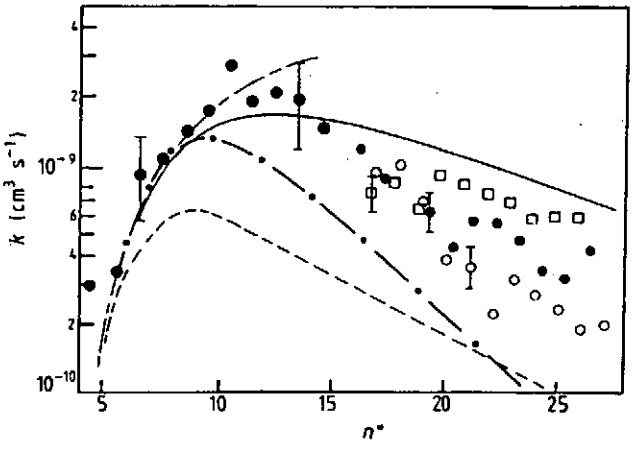

(Ref. 17).

Figure 3. Experimental and theoretical rate constant at $T = 1000$ K plotted against effective principal quantum number. Present results ($17 \leq n^* \leq 27$) are scaled to absolute results obtained by Boulmer *et al* (1983). Experimental data: □, s levels; ●, p levels; ○, $l \geq 2$ levels. Theoretical curves: —·—·—, k_{tot}; ——, p levels; —·—·—, $l \geq 2$ (hydrogenic) levels; - - - - -, s levels.

Suppose the net rate constant including other associative collisions leading to a chemical bond formation is $10^{-8}cm^3/s$. If the density of Rydberg atoms is $10^{11}cm^{-3}$, one chemical bond per neutral atom is formed in 0.1 ms. Unfortunately, however, a $1MeV/u$ swift atom with the velocity of $1\times10^7m/s$, travels a distance of 1 km in the period of 0.1 ms. Therefore a long drift tube is necessary to generate a MeV/u cluster beam under the low density of atomic beam.

5. Conclusion

Multiply-charged Clusters have a critical size below which they are intrinsically unstable with respect to the Coulomb repulsion between atomic ions. Accordingly, direct acceleration of cluster up to high energy is difficult. Another method to generate a high energy cluster beam is based on the principle that the interaction between highly-excited neutral atoms is in long-range and its magnitude is large in scale with n^7. Swift highly-excited neutral atoms may collide associatively with each other and make a cluster in such condition that the relative kinetic energies between the neutral atoms are smaller than the dissociative energy of cluster, but are sufficiently high for associative collision.

References

[1]M.Watanabe, K.Hata, T.Adachi, R.Nodomi and S.Watanabe, Opt. Lett. **15,** 845 (1990).

[2]A.J.Taylor, C.R.Tallmann, J.P.Roberts, C.S.Lester, T.R.Gosnell, P.H.Y.Lee and B.J.Kimura, Opt. Lett. **15,** 39 (1990).

[3]D.S.Gemmell, Necl. Instrum. Methods **170,** 41 (1980).

[4]R.Laubert and F.K.Chen, Phys. Rev. Lett. **40,** 174 (1978).

[5]M.J.Gaillard, J.C.Poizat and J.Remillieux, Phys. Rev. Lett. **41,** 159 (1978).

[6]A.Faibis, G.Goldring and Z.Vager, Phys. Rev. Lett. **39** 695 (1977).

[7]C.Deutsch, Laser and Part. Beams, **8,** 541 (1990).

[8]E.W.becker et al., Nucl. Eng. Design **73,** 187 (1982).

[9]R.J.Beuhler, G.Friedlander and L.Friedman, Phys. Rev. Lett. **63,** 1292 (1989).

[10]C.Bréchignac, Ph.Cahuzac, F.Carlier and J.Leygnier, Phys. Rev. Lett. **63,** 1368 (1989). See also C.Brécignac, Ph.Cahuzac, F.Carlier and M.deFrutos, Phys. Rev. Lett. **64,** 2893 (1990).

[11]D.J.wineland and W.M.Itano, Phys. Rev. **A20,** 1521 (1979).

[12]J.Javanainen, M.Kaivola, U.Nielsen, O.Poulsen and E.Riis, J. Opt. Soc. Am. **B2,** 1768 (1985).

[13]S.Schröder et al. Phys. Rev. Lett. **24,** 2901 (1990).

[14]A.Khadjavi, A.Lurio and W.Happer, Phys. Rev. **167,** 128 (1968).

[15]A.F.vanRaan, G.Baum and W.Raith, J. Phys., **B9,** L349 (1976).

[16]P.P.Herrmann, J.Hoffnagle, N.Schlumpf, V.L.Telegdi and A.Weis, J. Phys., **B19,** 535 (1986).

[17]J.Weiner and J.Boulmer, J. Phys., **B19,** 599 (1986).

PROGRAM OF WORKSHOP ON PLASMA-BASED AND NOVEL ACCELERATORS

National Institute for Fusion Science, Nagoya
December 19-20, 1991

THURSDAY MORNING

Opening Talks
R.Sugihara

Review of Plasma-Based Accelerators
Y.Nishida

Topics in Division of Plasma Physics in 1991 APS Autumn Meeting
Y.Nishida

Beat-Wave Acceleration Experiment Using CO_2 Laser at ILE, Osaka University and Laser Ionization of High Speed Gasjet for Beat-Wave Acceleration
Y.Kitagawa

Stabilization of Double Line Oscillation for Beat-Wave Acceleration
K.Matsuo

THURSDAY AFTERNOON

Introduction to Study of Plasma Resonance to Laser Beat Wave Carried out by G.Mattieussent et al. at LULI, France
Y.Suzuki

20MeV ESM Calibration for Laser Beat-Wave Acceleration
K.Sawai

Development of Electron Beam Source for Beat-Wave Acceleration
K.Morioka

MeV/u Cluster Genaration
Y.Iwata, N.Saito, M.Tanimoto, K.Sugisaki, S.Sekine, H.Shimizu and Y.Kimura

X-Band Microwave FEL for TBA Feasibility Study
S.Hiramatsu, K.Takayama, J.Kishiro, T.Ozaki, K.Ebihara, D.H.Whittum, Y.Kimura and T.Monaka

Particle Acceleration by Microwave with Corrugated Wave Guide
T.Watanabe, K.Ogura and K.Minami

FRIDAY MORNING

Plasma Wakefield Acceleration Experiment in KEK
K.Nakajima, H.Nakanishi, A.Enomoto, A.Ogata, T.Shoji, Y.Nishida and N.Yugami

Observation of the Plasma Lens Effect and Plasma Wakefield Acceleration Experiment in Electron Linac of Unversity of Tokyo
H.Kobayashi, A.Ogata, K.Nakajima, H.Nakanishi, A.Enomoto, H.Shibata, S.Tagawa, Y.Yoshida, T.Ueda, T.Kobayashi, K.Miya, Y.Nishida and N.Yugami

Plasma Focusing and Plasma Wakefield Acceleration Experiment by Using Twin Linac System
Y.Yoshida, T.Ueda, T.Kobayashi, K.Miya, H.Shibata, S.Tagawa, A.Ogata, K.Nakajima, H.Nakanishi, A.Enomoto, Y.Nishida and N.Yugami

Plasma Wave Excitation by Short-Wavelength Microwave
S.Kusaka, N.Yugami and Y.Nishida

FRIDAY AFTERNOON

$V_p \times$ B-Type Electron Accelerator Fabricated From Cylindrical Acceleration Tube
N.Yugami, K.Kikuta, D.Ariyama and Y.Nishida

Multi-Laser-Beam Accelerator
R.Sugihara

Electron Acceleration by Gaussian Laser Beam
S.Takeuchi, R.Sugihara and K.Shimoda

LIST OF PARTICIPANTS

Shigenori Hiramatsu	National Institute for High Energy Physics, KEK
Yasutsugu Iwata	Electrotechnical Laboratory
Yoneyoshi Kitagawa	Institute of Laser Engineering, Osaka University
Takahito Komatsu	Ishikawajima-Harima Heavy Industries Co., Ltd.
Shiro Kusaka	Faculty of Engineering, Utsunomiya University
Kazuya Matsuo	Institute of Laser Engineering, Osaka University
Kenji Morioka	Institute of Laser Engineering, Osaka University
Yasushi Nishida	Faculty of Engineering, Utsunomiya University
Yoshinobu Nunogaki	The Institute of Science and Industrial Research, Osaka University
Atsushi Ogata	National Institute for High Energy Physics, KEK
Yuichi Ogawa	Faculty of Engineering, The University of Tokyo
Kiyonobu Sawai	Institute of Laser Engineering, Osaka University
Tatsuo Shoji	Plasma Science Center, Nagoya University
Ryo Sugihara	Plasma Science Center, Nagoya University
Yasuo Suzuki	Japan Atomic Energy Research Institute
Masayoshi Taguchi	College of Industrial Technology, Nihon University
Kenichi Takagi	ULVAC Japan, Ltd.
Satoshi Takeuchi	Faculty of Engineering, Yamanashi University
Tsuguhiro Watanabe	National Institute for Fusion Science
Yoichi Yoshida	Nuclear Engineering Research Laboratory, The University of Tokyo
Noboru Yugami	Faculty of Engineering, Utsunomiya University

Recent Issues of NIFS Series

NIFS-PROC-1 *U.S.-Japan Workshop on Comparison of Theoretical and Experimental Transport in Toroidal Systems Oct. 23-27, 1989* Mar. 1990

NIFS-PROC-2 *Structures in Confined Plasmas –Proceedings of Workshop of US-Japan Joint Institute for Fusion Theory Program–* ; Mar. 1990

NIFS-PROC-3 *Proceedings of the First International Toki Conference on Plasma Physics and Controlled Nuclear Fusion –Next Generation Experiments in Helical Systems– Dec. 4-7, 1989* Mar. 1990

NIFS-PROC-4 *Plasma Spectroscopy and Atomic Processes –Proceedings of the Workshop at Data & Planning Center in NIFS–*; Sep. 1990

NIFS-PROC-5 *Symposium on Development of Intensed Pulsed Particle Beams and Its Applications February 20 1990*; Oct. 1990

NIFS-PROC-6 *Proceedings of the Second International TOKI Conference on Plasma Physics and Controlled Nuclear Fusion , Nonlinear Phenomena in Fusion Plasmas -Theory and Computer Simulation-;* Apr. 1991

NIFS-PROC-7 *Proceedings of Workshop on Emissions from Heavy Current Carrying High Density Plasma and Diagnostics;* May 1991

NIFS-PROC-8 *Symposium on Development and Applications of Intense Pulsed Particle Beams, December 6 - 7, 1990*; Jun. 1991

NIFS-PROC-9 *X-ray Radiation from Hot Dense Plasmas and Atomic Processes*; Oct. 1991

NIFS-PROC-10 *U.S.-Japan Workshop on "RF Heating and Current Drive in Confinement Systems Tokamaks" Nov. 18-21, 1991*, Jan. 1992